Titre: Title:	Application of a Numerical Code Based on Smoothed Particle Hydrodynamics to Estimate Stresses in Granular Backfilled Openings
Auteur: Author:	Armel Stanislas Nabolle
Date:	2022
Type:	Mémoire ou thèse / Dissertation or Thesis
Référence: Citation:	Nabolle, A. S. (2022). Application of a Numerical Code Based on Smoothed Particle Hydrodynamics to Estimate Stresses in Granular Backfilled Openings [Master's thesis, Polytechnique Montréal]. PolyPublie. https://publications.polymtl.ca/10443/

POLYTECHNIQUE MONTRÉAL

affiliée à l'Université de Montréal

Application of a numerical code based on smoothed particle hydrodynamics to estimate stresses in granular backfilled openings.

ARMEL STANISLAS NABOLLE

Département de génie civil, géologique et des mines

Mémoire présenté en vue de l'obtention du diplôme de *Maîtrise ès sciences appliquées*

Génie Civil

Juin 2022

POLYTECHNIQUE MONTRÉAL

affiliée à l'Université de Montréal

Ce mémoire intitulé:

Application of a numerical code based on smoothed particle hydrodynamics to estimate stresses in granular backfilled openings.

présenté par **Armel Stanislas NABOLLE**

en vue de l'obtention du diplôme de *Maîtrise ès sciences appliquées*

a été dûment accepté par le jury d'examen constitué de :

Li LI, président
Vincenzo SILVESTRI, membre et directeur de recherche
Ghassan ABOU-SAMRA, membre et codirecteur de recherche
Benoît COURCELLES, membre.

ACKNOWLEDGEMENTS

I thank all the people who contributed to the success of this master's degree and to the realization of this work which bears witness to the many efforts made.

First, I would like to thank my research advisor, Dr. Vincenzo SILVESTRI, for giving me the opportunity to conduct my numerical research and for giving me the chance to work under his supervision and for sharing his knowledge and expertise daily through two years of continuous hard work.

I would like also to thank Dr. Ghassan ABOU-SAMRA who acted as co-advisor in this research. I am indebted to him for sharing his knowledge, precious advice and for his encouragements.

Special thanks for Dr. Li LI, acting as president of my jury for reviewing my thesis and for his finding the time to be a part of the evaluation committee of this dissertation.

For his time and expertise as part of the evaluation committee of this dissertation, I thank Dr. Benoît COURCELLES.

Finally, I would like to thank my family and friends, especially my parents, who have always been able to listen and who have continued to support and encourage me throughout my journey.

RÉSUMÉ

La méthode des particules lissées SPH (Smoothed particle hydrodynamics) a été utilisée dans cette étude afin d'étudier le processus de remblayage dans une tranchée rocheuse. Elle a pour avantage de discrétiser le remblai en particules qui interagissent entre elles, simulant ainsi les particules granulaires du remblai et permettant de reproduire le processus de remblayage effectué sur les chantiers de construction.

Trois modèles ont été reproduits avec le logiciel Abaqus 2020 de la suite Simulia afin d'étudier l'effet du mode de déposition d'un matériau granulaire dans une tranchée rocheuse. Le premier modèle est un modèle SPH avec remblai déjà placé à l'endroit désiré simulant ainsi la configuration finale du remblai en place dans la tranchée rocheuse. Le second modèle est un modèle utilisant la méthode des éléments finis FEM avec remblai à l'endroit désiré simulant également la configuration finale du remblai : ce modèle représente un modèle de base pour comparaison car il correspond aux simulations effectuées généralement pour ce genre de problèmes. Le troisième modèle est une analyse avec la méthode des particules lissées SPH qui représente un processus de remblayage uniforme, continu et progressif. Ce modèle est composé de deux modes de remblayage : le premier s'effectue dans le sens de la direction longitudinale de la tranchée et le second dans la direction transversale. Plusieurs vitesses de remblayage ont également été considérées dans les analyses. Les résultats de ces modèles ont été comparées entre eux ainsi qu'avec les résultats analytiques développées par Li and Aubertin (2008).

Les résultats de ces simulations permettent de conclure que la distribution de la pression de contact (CPRESS) à la fin du processus de remblayage dépend de plusieurs facteurs et un réarrangement des particules peut être à l'origine d'une nouvelle distribution des pressions de contact et d'un regroupement dense de particules. En général, la pression de contact augmente avec l'augmentation de la densité des particules générées. Il ressort que les valeurs de la pression de contact augmentent également avec l'augmentation de la vitesse de remblayage et que la pression de contact est plus élevée pour le remblayage suivant la direction transversale. Les simulations du processus de remblayage suivant la direction transversale montrent l'effet d'arche qui s'observe au niveau des interfaces verticales de la tranchée où la friction entre le matériau granulaire et le roc plus rigide

donne lieu à un transfert de contrainte qui a pour effet la diminution des pressions de contact au niveau de ces interfaces.

Les tailles des particules générées pour cette études sont assez grandes (0.25m de diamètre minimum). Cela est dû principalement au temps de calcul numérique requis qui est extrêmement long. La prochaine étape pour de futurs travaux serait l'étude du processus pour des particules plus petites ainsi que l'impact du processus de remblayage pour les murs de soutènement.

ABSTRACT

Smoothed particle hydrodynamics (SPH) method has been used in this thesis to study the backfilling process of a backfilled rock stope. The SPH method has the advantage of discretizing the backfill material into particles interacting with each other, thus simulating the granular particles of the backfill and making it possible to reproduce the backfilling process.

Three models were constructed using Abaqus software (2020) to study the effect of the backfilling process and deposition mode. The first model is an SPH model with a wished-in-place backfill representing the backfill material already in place in the rock stope. The second model is a FEM model with also a wished-in-place backfill: this model will serve as a comparison model because it represents the simulations generally carried out for this type of problems. The third model is an SPH analysis representing a uniform, continuous and progressive backfilling process. This model is composed of two backfilling modes: the first one taking place along the longitudinal direction of the stope and the second one along the transversal direction. Several backfilling velocities were also considered in the analyses. The results of these models were compared with each other and with the analytical results developed by Li and Aubertin (2008).

The results of these simulations reveal that the contact pressure (CPRESS) distribution at the end of the backfilling process depends on several factors and a new state of interfacial contact stresses, and a dense gathering of particles can occur due to a rearrangement of the particles. In general, and for a specific initial mesh density, it is expected that values of CPRESSs increase when the initial mesh density decrease. It is also expected that values of CPRESSs increase when the backfilling velocity increase and values of CPRESSs are higher for a backfilling process in the transversal direction. For the backfilling process in the transversal direction, an arching effect is observed and is conditioned by the location of the vertical stopes where a stress transfer between the stiff backfill material and the stiffer surrounding rock mass due to friction at the interface of the two materials reduces the pressure and the stress near the stope-walls.

Also, the size of the generated particles in this study is significantly high. This is mainly due to the long computation time required in the simulations. The next step for future work would be the study for smaller particle sizes as well as the effect of the backfilling process for retaining walls.

TABLE OF CONTENTS

LIST OF TABLES

LIST OF FIGURES

LIST OF SYMBOLS AND ABBREVIATIONS

α	Coordinate direction
α_ϕ	Drucker-Prager's constants
β	Coordinate direction
c	Cohesion
CFD	Computational Fluid Dynamics
CPRESS	Contact pressure
δ	Dirac delta function
$\nabla \cdot f(x)$	Spatial derivative of $f(x)$
$\dot{\varepsilon}^{\alpha\beta}$	Total strain rate tensor
$\dot{\varepsilon}_e^{\alpha\beta}$	Elastic strain rate tensor
$\dot{\varepsilon}_p^{\alpha\beta}$	Plastic strain rate tensor
$\dot{e}^{\alpha\beta}$	Deviatoric shear strain rate tensor
E	Young's modulus
ϕ	Friction angle
$f(x)$	Function of the position vector x
f^α	Component of acceleration caused by external forces such as gravity force among others.
FEM	Finite Element Methods
g	Plastic potential flow function
G	Shear modulus
h	The smoothing length
I_1	First invariant of the Drucker-Prager stress tensor
J_2	Second invariant of the Drucker-Prager stress tensor

k_c	Drucker-Prager's constants
K	Elastic bulk modulus
$\dot{\lambda}$	Variation of the plastic multiplier λ
υ	Poisson's ratio
$\vec{n}$	Unit normal vector
N	Number of particles in the effective area of particle x.
Ω	Computing domain containing x
$\mathbf{\Pi_{ij}}$	Additional artificial viscosity
P	Hydrostatic pressure of granular material
ρ	Soil density
$\sigma^{\alpha\beta}$	Total stress tensor
σ^{xx}	Principal stress component in x direction
σ^{yy}	Principal stress component in y direction
σ^{zz}	Principal stress component in z direction
$\sigma^{\gamma\gamma}$	Sum of the normal stress components in x, y and z directions
$\dot{s}^{\alpha\beta}$	Deviatoric shear stress rate tensor
SPH	Smoothed particle hydrodynamics
v	Velocity
ψ	Dilatancy angle
$\dot{\omega}^{\alpha\beta}$	Spin rate tensor
W	Smoothing kernel function
WIP	Wished-in-place

CHAPTER 1 INTRODUCTION

1.1 Background and problematics

Backfilling is a process used in every aspect of civil engineering, such as: 1) construction of foundations in highway engineering and 2) mining waste disposal. Engineers have several methods to evaluate the stress and strain generated in the surrounding soil material.

1.1.1 Conventional analyses of backfilled stopes and piles installation: the wished-in-place solution

Analytical computations of stresses distributions in a soil and their interactions with surrounding structures use generally the assumption of overburden stress combined with alpha and/or beta methods for piles. In the case of backfilled stopes, the computations are performed within the final frame of configuration which assumes that the backfill is at rest and in equilibrium in the stope. Lately, numerical methods such as finite element methods (FEM) and discrete element methods (DEM) have been used to simulate several backfilled stopes (Aubertin et al., 2003; Fahey et al., 2009; Jahanbakhshzadeh et al., 2018; Li & Aubertin, 2009a; Li & Aubertin, 2009b; Li et al., 2003). These computations were performed to evaluate the stress and strain state of backfilled stopes (i.e., computing of the contact pressures (CPRESS) and the tangential contact stresses at the rock-backfill interface). In order to achieve this task, many authors performed finite element analyses of different backfill-rock assemblies while admitting that the backfill is placed at rest within the rock and in contact with its inner surface. This desired (or wished) backfill-rock assembly corresponds to the initial state configuration of the performed finite element analysis. Results of such analyses are deduced normally from the final deformed configuration after applying all external loads.

The same strategy was always used for the FEM analyses of installed piles and for evaluation of their bearing capacities. It is well known that by assuming a “wished-in-place” initial configuration for analysing rate-independent interaction problems between two different geo-material parts will induce several errors in the computation process (which uses a specific computational procedure), and therefore leading to unrealistic predicted solution-variables. These errors may occur because the nature of the dynamic continuous backfilling process was ignored and was not simulated

considering an explicit dynamic procedure to reflect the time dependency of stresses and strains during a continuous backfilling process.

In the case of a floating pile for example, this assumption of "wished-in-place" frame analysis is also used in this context and the assumption of the desired installation positions or physical locations of the assembled parts (which are in this case the floating pile and the surrounding soil) ignores the complete history of stresses and deformations along the continuous process of pile driving. This process starts by penetrating the upper surface of the soil and ends at the final wished installation location. During this process, the surrounding soil may be severely remolded (and may reach a yield state) to make room for the installed pile at the end of the installation process. In this case, stresses and strains generated within the soil (especially in the vicinity of the interacting surfaces of soil and pile where gradients are high) during the installation process cannot be ignored as they can sometimes be significant.

1.1.2 The use of the SPH method for accounting for excessive deformations due to backfilling processes

As previously explained, it is important to account for the stress and strain history generated during a backfilling process or during a pile installation process. By using an initial "wished-in-place" configuration assumption in a performed finite element analysis (FEA), the computational domain is discretized in small sub-domains or elements through the meshing step. Elements are connected via the nodes. During a backfilling process for example, the procedure used for the FEA will meet numerical difficulties caused by severe distortions of elements and results in termination of the analysis prior to completion.

Because the analyses of continuous backfilling process were not able to run to completion and this occurs by using an explicit finite element procedure, as well as an implicit dynamic procedure, and a static general procedure, it was concluded that the main FEMs are not suited for analysing such a process marked by severe deformations (Liu & Liu, 2016).

The recently developed particles' methods are well suited for these aforementioned kinds of backfilling problems. In this study, the smoothed particle hydrodynamics (SPH) method developed by Gingold and Monaghan (1977) and Lucy (1977) and integrated in Abaqus (2020) was used to

assess the continuous backfilling process and for predicting the stresses and strains distributions within the backfill and along the granular-rock interaction surfaces. By using the SPH method, assessment can be achieved despite large deformations occurring within the granular backfill as the backfill is now discretized as independent particles interacting with each other.

1.2 Objectives of the present study

The principal objective of this study is the assessment of the stresses during the simulation of different backfilling process in a backfilled stope with granular material.

In the present study, several SPH simulations were performed using an explicit dynamic procedure implemented in Abaqus/Explicit (2020) in order to:

- plot the distribution of contact pressures (CPRESSs) along interaction surfaces of the in-situ rock and backfill materials.
- determine the effect of the backfilling mode on computed stresses and strains within the backfill material and on the backfill-rock contact interfaces. This task may be achieved by performing a parametric study in which different deposition modes caused by different backfilling speeds are simulated. The solution-variables deduced from these simulations are compared with each other.
- compare the results predicted from a basic finite element model (BFEM) simulating the "wished-in-place" assembly to those deduced from different performed analyses of SPH models simulating different modes of backfilling processes.
- compare SPH and FEM predicted results between each other, and also to the analytical solution developed by Li and Aubertin (2008).

1.3 Organization of this thesis

The present study is composed of five chapters:

The first chapter presents a brief description of the conventional used analytical and numerical methods for analysing backfilling problems. The problem of large and excessive deformations of

geo-materials in these aforementioned problems is presented in this chapter and a solution based on a smoothed particle hydrodynamics method (SPH) is suggested to solve the problem.

The second chapter presents a literature review of previous numerical studies, modelling activities, and analytical closed-form solutions in order to assess the stress state in backfilled stopes.

The third chapter will include a literature review on the evolution over the years of the SPH theory, its formulation, and its application in the field of solid mechanics. The use of the SPH method in the field of geotechnical engineering is presented in this chapter mainly for slope stability and retaining walls. Results deduced from several SPH' simulations are presented and discussed in this section.

The fourth chapter constitutes the author's contribution as it contains details of numerical results deduced from all Abaqus/Explicit simulations performed in the course of this work. Description of all performed simulations including their used SPH models are presented in detail in this chapter. The characteristics of all simulations such as: i) the SPH Abaqus/Explicit models, ii) the mechanical material model of the backfill and rock, ii) the explicit dynamic procedure used in all models, iii) the loading process, and iv) the mesh construction are all presented in detail herein. More importantly, all numerical results deduced from performed SPH' simulations have been depicted in several graphs which are inserted in this chapter.

The fifth chapter presents comparisons between results obtained from different SPH and FEM models. These SPH-FEM comparisons show and highlight the effect of particles rearrangement and soil density as well as the effect of: 1)- SPH particles' size, 2)- backfilling velocity, and 3)- backfilling mode during the continuous progressive backfilling process. Comparisons are also made between the SPH and FEM results, and the analytical solution developed by Li and Aubertin (2008).

The last chapter summarizes all findings and conclusions on the achieved work in the present thesis and it will draw several recommendations for future research studies.

CHAPTER 2 LITERATURE REVIEW ON STRESS STATES IN BACKFILLED STOPES

In the mining field, waste disposal by backfilling is now a common practice that ensures stability of mine stopes after extraction of the ore and minimises the environmental impact of mining operations (Benzaazoua et al., 2008).

In this chapter, the types of mine backfills used in the mining field are first presented. A literature review on stress state estimation and evaluation in backfilled stopes is also presented. Many authors succeeded to develop analytical solutions in order to assess stresses and deformations within a backfilled stope. Also, numerical studies have been conducted by using finite element methods and finite difference methods in order to determine stresses and deformations in the backfilled medium. All these aforementioned achievements were based on quasi-static procedures. For the best of the knowledges of the author, none of these studies used an explicit dynamic procedure. In this study, the author aimed to assess the dynamic backfilling process in the mining field by using an explicit dynamic procedure implemented in a commercial numerical code i.e., Abaqus/Explicit (Dassault Systèmes Simulia Corp., 2020). Computed values deduced from performed simulations and depicted in many curves and graphs will be shown later in this thesis.

2.1 Types of mine backfills

Generally, three types of mine backfills are used in the mining industry: 1) the rockfill, 2) the hydraulic fill and 3) the paste fill. These tree types will be briefly described hereafter.

2.1.1 The rockfill type

Rockfill may be composed of stones or gravels or sand or industrial mine waste to which a binder slurry is sometimes added in order to cement the fill and provide a better mechanical resistance (Yao et al., 2012). The rockfill's material is the result of the three successive operations: crushing of the rockfill, sieving of the crushed material, and finally mixing and transportation of this final product by conveyors or trucks. Cemented rockfills have in general a cement content of 1 to 6%. This is necessary to have a good binder coating on the aggregates and to reduce the cost price of the entire production operation (Emad et al., 2015).

2.1.2 The hydraulic fill type

The hydraulic fill type is also named slurry backfill. Generally, hydraulic fills are composed by mixing sand and water (with 60 to 70% solid pulp density) and permeable low density blend of mill tailing (Emad et al., 2015).The hydraulic fill is convoyed using pipelines and its displacement is achieved continuously and at high velocity. This operation is successfully achieved by using a large amount of water to ensure an easier flow of the mixed materials during the transport operation. During transportation constant mixing is also necessary to maintain good suspension of solid part. After the installation of the mix in the backfill stope, the settlement process starts, and redistributions of stresses and deformations will cause the water within the mixed materials to be evacuated upward. After reaching this state, and once the water covers the settled materials, it is pumped back directly to the surface of the fill (Potvin et al., 2005). Some hydraulic fills contain binders when liquefaction or future exposure of the fill is a possibility. Hydraulic fills are more economic than the paste fills but they are usually weaker than the other types of fills (Potvin et al., 2005).

2.1.3 The paste fill type

This last backfill has become an increasingly popular common practice in underground mines. Paste fill is a thick mix of mill tailings, binders, and water with a mud-like or paste consistency. In the paste fill, the solid content is around 75 to 80% by weight. The paste fill should have the necessary amount of fines particles for a better paste behavior (Potvin et al., 2005). Transporting the mix is usually done using piston pumps, gravity, or a combination of both. The cleaning of the pipeline network may be performed by using water and compressed air pressurization to avoid any possible clogging of the pipes by the backfill (Belem & Benzaazoua, 2008).

2.2 Analytical solutions of stress state in backfilled stopes

The simplest way to evaluated the vertical overburden stress in a layered soil may be taken from Bowles (1996) and is presented in Eq. (2.1) :

$$\sigma_v = \gamma z \tag{2.1}$$

where:

σ_v is the major principal vertical stress,

γ is the soil's unit weight, and

z is the depth of interest measured from the horizontal ground surface.

Janssen (1895) analyzed the arching effect on granular material contained in silo. Due to gravity, the granular material settles down under its own weight and it is hold at the same time by the surrounding wall by shear forces located at the granular material-silo's wall interface. The occurrence of these shear forces tends to reduce the vertical stress P_0 (as mentioned in Eq. (2.2) or previous Eq. (2.1)). The analytical solution proposed by Janssen (1895) for estimation of the vertical stress as it was taken from Bowles (1996) is presented in the following equation:

$$P_0 = \frac{\gamma R}{K_a \tan\delta}\left[1 - e^{-K_a \cdot \frac{Z}{R} \cdot \tan\delta}\right] \tag{2.2}$$

where:

P_0 is the vertical stress,

δ is friction angle at the wall-granular material interface,

K_a is the active earth pressure coefficient,

$R = area/perimeter$ of the silo and is named the hydraulic radius, and

Z is the depth within the granular medium.

In his developed equation, Janssen (1895) assumed that the vertical stress is constant over the horizontal cross section.

Marston (1930) developed an analytical solution based on the arching effect occurring in the granular medium to compute the applied stress on buried pipes in ditches. This analytical solution was used by Li and Aubertin (2008) and it is given bellow:

$$\sigma_v = \frac{\gamma B}{2K_a \tan\delta}\left[1 - \exp\left(-\frac{2K_a h \tan\delta}{B}\right)\right] \tag{2.3}$$

where:

B is the width of the trench,

h is the depth of a point element within the granular medium, and

K_a, δ and γ were defined above in Eq. (2.2).

Aubertin et al. (2003) used the theory of Marston (1930) witch was designed for estimating applied stresses on buried pipes in ditches in order to develop a new analytical solution which accounts for arching effects in narrow backfilled stopes. The authors used the force equilibrium equations for a layer element depicted in Figure 2-1 in the aim of developing Eq. (2.4). They found that the applied vertical and horizontal stresses on the stope's floor may be written as:

$$\sigma_{vH} = \gamma B \left(\frac{1 - \exp\left(-\frac{2KH \tan \emptyset'}{B}\right)}{2K \tan \emptyset'} \right) \tag{2.4}$$

$$\sigma_{hH} = \gamma B \left(\frac{1 - \exp\left(-\frac{2KH \tan \emptyset'}{B}\right)}{2 \tan \emptyset'} \right) \tag{2.5}$$

where:

H is the depth of the granular medium,

K is the lateral earth pressure coefficient, and

$\emptyset'$ is the internal friction angle of the fill material which was assumed equivalent to the interface's friction angle separating the backfill and the wall.

Aubertin et al. (2003) compared their analytical results (Eq. (2.4) and (2.5)) with results deduced from finite element analyses (FEA) performed with PHASES2 software (RocScience, 2002). The aforementioned equations assume a uniform vertical stress distribution along a horizontal section plane of the trench.

Li and Aubertin (2008) proposed an improved analytical solution based on Marston solution and considering a non-uniform vertical stress distribution across the width of a vertical backfilled stope

(Figure 2-1). They introduced new parameters that have been calibrated with numerical modelling results in FLAC-2D (Itasca, 2002; Itasca). The horizontal stress (σ_h) and vertical stress (σ_{vx}) at depth h ($0 \leq h \leq H$) in a vertical backfilled stope are expressed as:

$$\sigma_h = \frac{\gamma B}{2\tan\delta}\left[1 - \exp\left(-\frac{2K'\tan\delta}{B(1-DF)}h\right)\right] \tag{2.6}$$

$$\sigma_{vx} = \frac{\gamma B}{2\,\mathrm{K}'\tan\delta}\left\{1 - \exp\left[-\frac{2K'\tan\delta}{B(1-DF)}h\right]\right\} \times \left[1 - a\left(\frac{|x|}{B}\right)^b\right] \tag{2.7}$$

where:

x is the distance from the centerline,

$DF = \frac{a}{2^b(b+1)}$,

$a = 2^{\left(1-\lambda_1\frac{H}{B}\right)}\tan^{-\lambda_2}(\phi_0 + \phi')$,

$b = 3$,

$\mathrm{K}' = 1 - \sin\phi'$,

$\phi_0 = 50°$,

$\lambda_1 = 0.02$, and

$\lambda_2 = 0.1$.

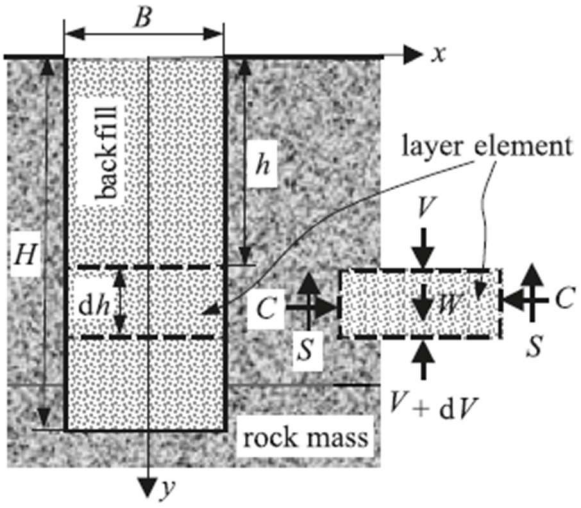

Figure 2-1 : A vertical backfilled stope with the acting forces on the isolated layer element (Li & Aubertin, 2008)

Li and Aubertin (2008) compared σ_h and σ_{vx} in Eq.(2.6) and (2.7) respectively, with the values found by Drescher (1991), i.e.:

$$\sigma_{vx} = \sigma_{vB/2} - a'\left[1 - \left(\frac{2x}{B}\right)^2\right] \tag{2.8}$$

$$\tau_x = \sigma_{vB/2}\frac{sin\,\delta\,sin\,2\psi}{1 - sin\,\delta\,cos\,2\psi}\left(\frac{2x}{B}\right) \tag{2.9}$$

$$(\sigma_{hx} - \sigma_{vx})^2 + 4\tau_x^2 - (\sigma_{hx} - \sigma_{vx})^2 sin^2\delta = 0 \tag{2.10}$$

where:

a' is a constant expressing the backfill properties and stress state at the wall, and

ψ is the major principal rotation angle at the wall.

Li and Aubertin (2008) also used FLAC (Itasca, 2002), a commercial finite difference software to perform 2D analyses in order to estimate the stress state in subvertical backfilled stopes. These analyses are based on a plane strain model of a trench having a depth of 45 m and a width of 6 m. In their study, they assumed that the modelled backfill was behaving complying to the Mohr-

Coulomb plastic criterion. The friction angle ϕ' of the backfill material was given a value of 30°. In the elastic phase the backfill was assumed to follow a linear stress-strain behavior with a Young's modulus of 300MPa and a Poisson's coefficient of 0.2. In their numerical work, these authors assumed that the angle of friction (δ) at the rock-backfill contact interface is equivalent to the internal friction angle of the backfill $\phi'(\delta = \phi' = 30^o)$. This conditions mean physically that most shear yielding is taking place at the backfill-wall interface. Li and Aubertin (2008) compared the outputted finite difference results to closed-form solutions developed in the same study. These authors concluded that the improved analytical solution, i.e., Eq. (2.6) and (2.7) provides a good representation of the stress distribution in a narrow-backfilled stope.

Jahanbakhshzadeh et al. (2017) proposed a new analytical solution for stresses evaluation in backfilled stopes with inclined walls (Figure 2-2). This proposed solution accounts for the change of stresses with the height and width of the stope, and it is expressed in the following matter:

$$\sigma_{vh} = \frac{\gamma B \sin\beta}{2\, K_\beta \tan\emptyset'}\left[1 - \exp\left(-\frac{2K_\beta \tan\emptyset'}{B(\sin\beta)}h\right)\right] \tag{2.11}$$

$$\sigma_{hh} = K_\beta \sigma_{vh} \tag{2.12}$$

where:

γ is the backfill material unit weight,

σ_{vh} and σ_{hh} are the vertical and horizontal stress at the depth h respectively,

β is the inclination angle depicted in Figure 2-2,

$\emptyset'$ is the friction angle,

l is the horizontal distance measured from the inclined wall as showed in Figure 2-2,

B is the horizontal width of the inclined backfilled stope,

K_a is the Rankine's active earth pressure,

$f_h = (1 + \cos\beta) - \left[\frac{h}{H}\tan\emptyset' \cos^2\beta\right]$,

$$f_w = \left\{1 + 3\left(1 - \frac{l}{B}\right)^4 \tan\emptyset' \cos(\beta - 10°)\right\},$$

f_h and f_w represent the effect of geometrical factors, and

$K_\beta = K_a \times f_h \times f_w$,

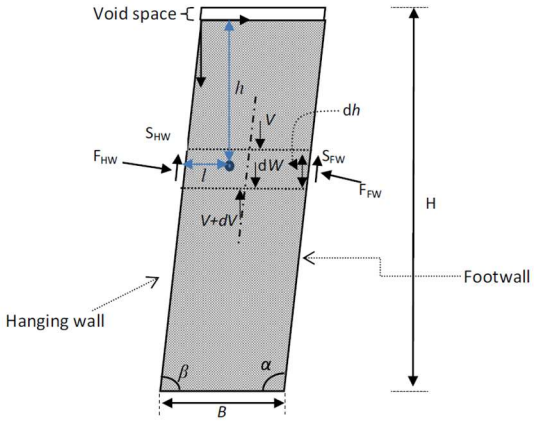

Figure 2-2 : Reference model for an inclined backfilled stope (Jahanbakhshzadeh et al., 2017).

The solution mentioned previously and found in Jahanbakhshzadeh et al. (2017), was extended to a 3D solution by Jahanbakhshzadeh et al. (2018). It can be written as:

$$\sigma_{zz} = \frac{\gamma \sin\beta}{2\,(B^{-1} + L^{-1})K_\beta \tan\emptyset'}\left[1 - \exp\left(-\frac{2(B^{-1} + L^{-1})K_\beta \tan\emptyset'}{(\sin\beta)}h\right)\right] \quad (2.13)$$

$$\sigma_{xx} = \sigma_{yy} = K_\beta \sigma_{zz} \quad (2.14)$$

where:

γ is the backfill material unit weight,

σ_{zz} is the vertical stress at the depth h,

σ_{xx} and σ_{yy} are the horizontal stress in the direction of B and L respectively at the depth h,

β is the inclination angle depicted in Figure 2-3,

$\emptyset'$ is the friction angle,

L is the horizontal dimension shown in Figure 2-3,

B is the horizontal width of the backfilled stope shown in Figure 2-3,

K_a is the Rankine's active earth pressure,

$$f_h = (1 + \cos\beta) - \left[\frac{h}{H}\tan\emptyset' \cos^2\beta\right],$$

$$f_w = \left\{1 + 3\left(1 - \frac{l}{B}\right)^4 \tan\emptyset' \cos(\beta - 10°)\right\},$$

f_h and f_w represent the effect of geometrical factors, and

$$K_\beta = K_a \times f_h \times f_w,$$

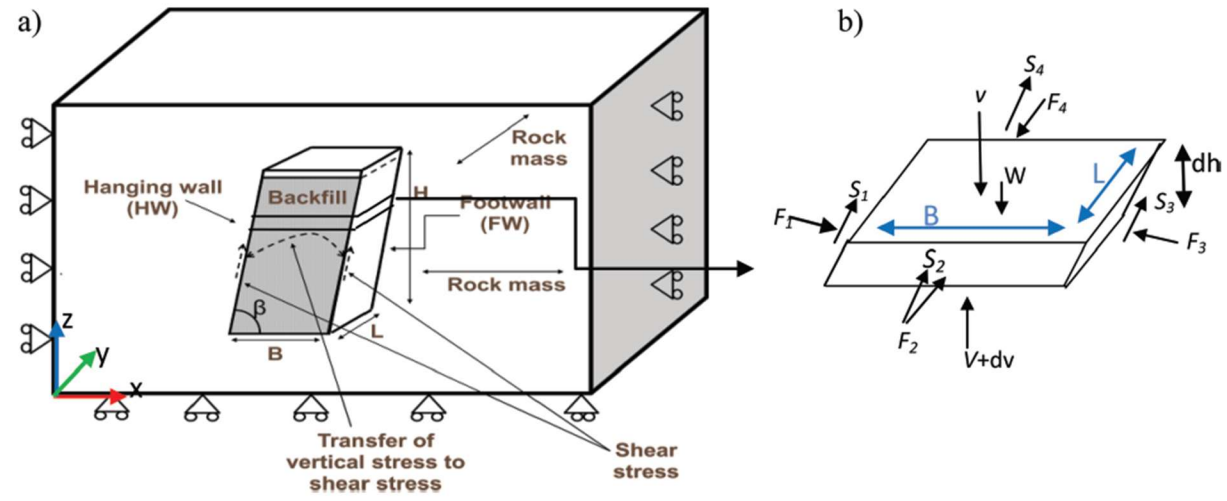

Figure 2-3 : 3D inclined backfilled stopes: (a) reference conceptual model; (b) forces acting on isolated layer element (Jahanbakhshzadeh et al., 2018).

2.3 Numerical simulations of stress state in backfilled stopes

Several numerical analyses have been carried out by many researchers in the aim of validating the aforementioned closed-form solutions successfully found by many authors. In this activity, the effects of many factors such as the geometry of the stope and the backfill properties have been investigated in order to check their effect on the stress and strain distributions within a backfilled stope.

In this sector of activity, Aubertin et al. (2003) performed several finite element analyses (FEA) using PHASES2 commercial software (RocScience, 2002) to assess stress distribution in a vertical and inclined backfilled stope. The predicted values deduced from these analyses permitted to conclude that the vertical stress at the bottom of the stope remains lower than the overburden stress applied at the same bottom place. It was concluded that this last result was caused by arching effects. It was also found that the maximum value of the vertical stress is located around mid-height of the stope and it is higher than the overburden stress at the same location. This finding is due to the inward wall convergence squeezing the backfill. In the case of an inclined stope, these authors mentioned that arching effects are less developed and severe than in the case of a vertical backfilled stope. They also compared the numerical results found in Aubertin et al. (2003) with closed-form solution developed within the same paper i.e. stresses acting on the stope floor and wall in Eq. (2.4) and (2.5).

Li et al. (2003) used FLAC (Itasca, 2002), a commercial finite difference software to study the arching effects in a backfilled stope. The analysis ran to completion after using two successive steps:

- In the first step it was assumed that the stope was excavated instantaneously, and no sequence of successive excavated layers was used; and
- In the second step, it was assumed that the empty excavated stope was perfectly rigid, and all initial deformations are set to zero (i.e., the excavated stope does not undergo any deformation during this step). This assumption has been necessary to avoid numerical divergence of the solution. Here the filling of the excavated stope was achieved in this step. The interpretation of the outputted solution-variables permitted to conclude that the phenomenon of arching is quite present since the vertical and horizontal stresses are lower near the wall. They also noticed that the vertical stress is not uniform across the width of the stope.

Fahey et al. (2009) performed numerical simulations using Plaxis 2D (Brinkgreve et al., 2006) a commercial finite element code in the aim of investigating aspects of the arching effects within backfilled stopes. In this study, they assumed the following different modelling conditions:

- At the first place, the backfill material was assumed to be dry, and no pore water pressure was considered. In these conditions it was found that the arching effects occurring inner the dry backfill and for a plane strain state are less important and severe than those occurring in an axisymmetric stress state.
- They also conducted 2D FEM analyses assuming different filing types: a) saturated undrained backfill, b) saturated drained backfill, and c) partially drained backfill in order to investigate the effect of drainage and consolidation on stress distribution. They concluded that for an undrained filling condition, total horizontal and vertical stresses are almost equal to the total overburden stress; consequently, no arching effects have been developed. During the consolidation process, excess pore water pressure dissipates and decreases with time permitting an increase of effective stresses and therefore the arching effects are developed. Fahey et al. (2009) also concluded based on their results that the filling types does not influence the final stress state.

Li and Aubertin (2009a) performed finite difference analyses using FLAC2D (Itasca, 2002) to study the effects of pore water pressure on the stress state in backfilled stopes. They considered three different cases in their study:

- a submerge backfill in which the phreatic line was located on the surface of the backfill,
- a backfill under water i.e., the backfill surface remains below the phreatic surface, and
- a partially submerged backfill, in this case the phreatic surface is located within the backfill and lower than the backfill surface. In this case, there is a stress transition at the phreatic surface. For the submerged and backfill under water cases, numerical solutions for effectives stresses are in accordance with their proposed analytical solution.

Li and Aubertin (2009b) conducted numerical analyses using FLAC2D (Itasca, 2002) , a commercial finite difference code to study the stress state in an inclined backfilled stope. Also, the influence of the stope's geometry and the backfill's properties were investigated herein. It was concluded throughout this study that along the hanging wall and inclined center line the horizontal stress was not affected by the stope's inclination. Regarding the vertical stress, the computed values

showed that it decreases in a significant matter when the stope's inclination decreases. They also noticed that vertical and horizontal stresses decrease with a decreasing stope's width. Regarding the Young's modulus of elasticity E, these authors found that the stress state remains unchangeable when the value of E remains lower than $300MPa$. It was also deduced throughout this study, that for the highest values of E until reaching $3GPa$, the stresses exhibit an irregular state. They also observed a slight increase of the horizontal stress accompanied by a significant decrease of the vertical stress when the Poisson's ratio (ν) increases. It was found also that an increase of the friction angle ($\emptyset'$) tends to decrease both vertical and horizontal stresses. Moreover, for friction angles having values higher than $20°$, it was found that the vertical stress tends to be insensitive to the variation of $\emptyset'$. They also found that, for cohesion values in the range of $10kPa \leq c' \leq 50kpa$, the stress distribution on stopes depends on the backfill's cohesion (c'). For values of c' outside this range, it was concluded that the stress state is independent of c'. The stresses also tend to decrease when the dilatation's angle ψ' increases.

Jahanbakhshzadeh et al. (2018) used a finite difference code in FLAC3D (Itasca, 2013) to assess the stress state in the case of an inclined backfilled stope. The effects of stope's geometry and the backfill's properties on stress distribution were investigated in this study. Here, the finite difference results found were in perfect agreement with those found by Li and Aubertin (2009b). Comparisons have been carried out between their new 3D analytical solution and numerical results deduced from their finite element model.

CHAPTER 3 THEORY OF SMOOTHED PARTICLE METHOD

3.1 Introduction

The theory of the smoothed particle hydrodynamics method (SPH) is presented in this chapter, as well as its formulations and modeling for soil mechanics and geotechnical applications. SPH applications in the geotechnical field are also presented as well as the results and discussions of published numerical simulations.

3.2 Description and use of currently available numerical techniques

Modeling techniques using numerical methods such as standard finite elements methods (which is implemented in Abaqus/Standard), explicit finite element method (which is also implemented in Abaqus/Explicit), discrete element methods (DEM), coupled Eulerian-Lagrangian technique (CEL), and particulate method including the smoothed particle hydrodynamic SPH technique (which is implemented in Abaqus and has been used in the present study) are becoming the only efficient tools to obtain a numerical solution for complicated engineering simulated events marked by excessive deformations. Grid based methods are the most used ones in various areas of computational fluid dynamics (CFD) and computational solid dynamics (Liu & Liu, 2016). For solid dynamic problems, finite element methods (FEM) represent a Lagrangian description of the physical governing equations and are the most used ones for problem solving through the discretization of the continuum domain in small subdomains or elements with a meshing step. This step can be a problem when dealing with free surfaces, deformable boundaries, moving interfaces, and large deformation problems (Liu & Liu, 2016).

Meshfree methods have been introduced in past years to solve those problems that grid based methods meet when it comes to numerical simulations. Meshfree methods have the advantage of solving large deformations problems by dividing the domain in a set of distributed nodes or particles that are not connected with each other.

One of the most used meshfree methods is the smoothed particle hydrodynamics (SPH) based on pure Lagrangian description and consists of the discretization of the domain in a set distributed macro-scale particles with material properties and analyzing of their movements and interactions.

3.3 The SPH method

The smoothed particle hydrodynamics method was used first for astrophysics and hydrodynamics problems in open space as particles movements using equations of classical Newtonian hydrodynamics are closed to that of fluid (liquid or gas) flow (Gingold & Monaghan, 1977; Lucy, 1977) . Those applications were mainly based on the explanation of astrophysics phenomena like stellar collisions by Benz (1988) and formation and collapse of galaxies by Monaghan and Lattanzio (1991); (1992). Hydrodynamic applications were used among others to simulate free surface flow and fluid-solid interaction, i.e. impact simulation presented by Huang et al. (2014). The SPH technique has been intentionally developed to be used for simulating complex physical events involving fluid and/or solid mechanics dealing with extreme deformations. These applications are among others flow-like landslide, i.e., soil slope progressive collapse, internal failure due to seepage, dam breaks (Bui et al., 2008). Some of the applications on geotechnical problems will be described in section 3.5.

3.4 The SPH formulation

The SPH method is a mesh free based numerical method composed of two distinct steps of formulation. The first step includes the kernel approximation which consists in approximating a function and its derivatives as an integral (Liu & Liu, 2016) using the smoothing kernel function (also called weight function). In the second step named particle approximation, the computing domain is discretized using a set of particles in which values of field variables for each particle are obtained by summation of the neighbour particles weighted with the smoothing kernel function (Liu & Liu, 2016).

3.4.1 The kernel approximation

A kernel function or smoothing function or weight function is used to represent a function and its derivatives as an integral representation in the kernel approximation (Liu & Liu, 2016). In the SPH method, the kernel representation of a $f(\boldsymbol{x})$ function is:

$$f(\boldsymbol{x}) = \int_{\Omega} f(\boldsymbol{x}')\delta(\boldsymbol{x} - \boldsymbol{x}')\, d\boldsymbol{x}' \tag{3.1}$$

where:

f is a function of the position vector $\boldsymbol{x}$,

Ω is the computing domain containing the position vector $\boldsymbol{x}$,

$\delta(\boldsymbol{x}-\boldsymbol{x}')$ the Dirac delta function described as:

$$\delta(\boldsymbol{x}-\boldsymbol{x}') = \begin{cases} \infty, & \boldsymbol{x}=\boldsymbol{x}' \\ 0, & \boldsymbol{x}\neq\boldsymbol{x}' \end{cases} \tag{3.2}$$

Due to the use of the Dirac delta function, as long as $f(\boldsymbol{x})$ is defined and continuous in the computing domain, the integral representation is exact and rigorous. The delta function $\delta(\boldsymbol{x}-\boldsymbol{x}')$ can be replaced by a smoothing kernel function $W(\boldsymbol{x}-\boldsymbol{x}',h)$, and the integral representation becomes an approximation as following (Liu & Liu, 2016):

$$\langle f(\boldsymbol{x})\rangle = \int_{\Omega} f(\boldsymbol{x}')W(\boldsymbol{x}-\boldsymbol{x}',h)\,d\boldsymbol{x}' = \int_{\Omega} f(\boldsymbol{x}')W(\boldsymbol{r},h)\,d\boldsymbol{x}' \tag{3.3}$$

where $\boldsymbol{r}=\boldsymbol{x}-\boldsymbol{x}'$ and h the smoothing length limiting the area of influence of the smoothing function W (explained in section 3.4.3) and h is the smoothing length delimiting the effective area of the particle at $\boldsymbol{x}$.

The kernel approximation for spatial derivative $\nabla\cdot f(\boldsymbol{x})$ can be obtained by replacing $f(\boldsymbol{x})$ by $\nabla\cdot f(\boldsymbol{x})$ in Eq. (3.3) to obtain (Liu & Liu, 2016):

$$\langle \nabla\cdot f(\boldsymbol{x})\rangle = \int_{\Omega} [\nabla\cdot f(\boldsymbol{x}')]W(\boldsymbol{x}-\boldsymbol{x}',h)\,d\boldsymbol{x}' \tag{3.4}$$

we also know that:

$$[\nabla\cdot f(\boldsymbol{x}')]W(\boldsymbol{x}-\boldsymbol{x}',h) = \nabla\cdot[f(\boldsymbol{x}')W(\boldsymbol{x}-\boldsymbol{x}',h)] - f(\boldsymbol{x}')\cdot\nabla[W(\boldsymbol{x}-\boldsymbol{x}',h)] \tag{3.5}$$

and

$$\begin{aligned} \langle \nabla \cdot f(\boldsymbol{x}) \rangle &= \int_{\Omega} \nabla \cdot [f(\boldsymbol{x}')W(\boldsymbol{x}-\boldsymbol{x}',h)]\, d\boldsymbol{x}' - \int_{\Omega} f(\boldsymbol{x}') \cdot \nabla[W(\boldsymbol{x}-\boldsymbol{x}',h)]\, d\boldsymbol{x}' \\ &= \int_{S} f(\boldsymbol{x}')W(\boldsymbol{x}-\boldsymbol{x}',h) \cdot \vec{n} dS - \int_{\Omega} f(\boldsymbol{x}') \cdot \nabla W(\boldsymbol{x}-\boldsymbol{x}',h)\, d\boldsymbol{x}' \end{aligned} \tag{3.6}$$

where $\vec{n}$ is a unit vector normal to the surface *S*.

Due to the compact condition ($W(\boldsymbol{x}-\boldsymbol{x}',h) = 0 \;\; when \;\; |\boldsymbol{x}-\boldsymbol{x}'| > \kappa h$) of the smoothing function, W is equal to zero at the surface of the integral in Eq. (3.6).

The kernel approximation for spatial derivatives is then (Liu & Liu, 2016):

$$\langle \nabla \cdot f(\boldsymbol{x}) \rangle = -\int_{\Omega} f(\boldsymbol{x}') \cdot \nabla W(\boldsymbol{x}-\boldsymbol{x}',h)\, d\boldsymbol{x}' \tag{3.7}$$

3.4.2 Particle Approximation

In the phase of particle approximation, the computing domain is replaced by a set of particles, and field variables are then estimated through those particles. Each one of them is assigned field properties and is represented as an element volume ΔV defined using the mass and the density ratio ($\triangle V = m/\rho$). The continuous form of the kernel approximation in Eq. (3.3) may be represented in discretized form as a summation of near particles as follows (Liu & Liu, 2016):

$$\langle f(\boldsymbol{x}) \rangle = \sum_{j=1}^{N} \frac{m_j}{\rho_j} f(\boldsymbol{x}_j) W(\boldsymbol{x}-\boldsymbol{x}_j,h) \tag{3.8}$$

The parameter h was previously defined as the smoothing length; the parameter N stands for the number of particles j in the effective area of the particle at $\boldsymbol{x}$; the parameters m_j and ρ_j are respectively the mass and the density of each particle j.

Value of field variables for the particle at $\boldsymbol{x}$ is obtained by summation of neighbor particles j weighted with the smoothing kernel function W. The particle approximation of derivative is also obtained in a similar manner (Liu & Liu, 2016).

$$\langle \nabla \cdot f(\boldsymbol{x}) \rangle = -\sum_{j=1}^{N} \frac{m_j}{\rho_j} f(\boldsymbol{x}_j) \cdot \nabla W(\boldsymbol{x} - \boldsymbol{x}_j, h) \tag{3.9}$$

Figure 3-1 is a representation of a two-dimensional computational domain Ω as a set of particles with i being a particle whose field variables are approximated as an average of particles j in the smoothing length h using the smoothing function W. In a two-dimensional computational domain Ω, the smoothing length h delimits a surface S (see Figure 3-1).

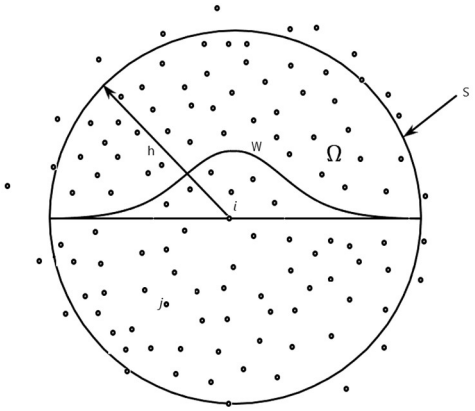

Figure 3-1 Particle approximation of an SPH two-dimensional problem.

Figure 3-2 is a three-dimensional representation of the computational domain Ω with the cone. The three-dimensional form of the smoothing function W is obtained by a rotation of the smoothing function in Figure 3-1 around an axis.

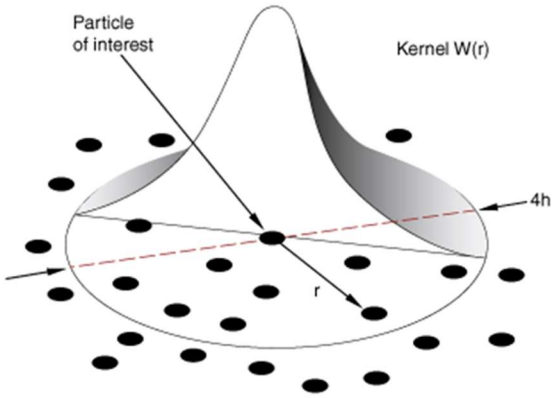

Figure 3-2 Three-dimensional representation of the computational domain Ω (Dassault Systèmes Simulia Corp., 2020)

The replacement of the continuous integral form by particle summation is an important part of the SPH method, making it a simple method with no need for meshing for numerical integration (Liu & Liu, 2016).

3.4.3 The smoothing function W

A number of smoothing functions W have been developed and used in the SPH method. The smoothing function must respect the following properties and conditions, as cited by (Liu & Liu, 2016):

- the smoothing function W should be normalized over the computing domain (i.e., unity condition):

$$\int_{\Omega} W(\boldsymbol{x}-\boldsymbol{x}', h)\, d\boldsymbol{x}' = 1 \tag{3.10}$$

- the smoothing function must be equal to the Dirac delta function as the smoothing length value approaches zero:

$$\lim_{h\to 0} W(\boldsymbol{x}-\boldsymbol{x}', h) = \delta(\boldsymbol{x}-\boldsymbol{x}') \tag{3.11}$$

- the compact condition which states that:

$$W(\boldsymbol{x}-\boldsymbol{x}', h) = 0 \quad when \ |\boldsymbol{x}-\boldsymbol{x}'| > \kappa h \tag{3.12}$$

where κ being a constant for a particle in the smoothing function and κh denotes the effective area of the smoothing function. This condition ensures that particles out of the effective area of particle x have no effect on that particle.

- the smoothing function should be positive within the support domain (positivity)

$$W(\boldsymbol{x}-\boldsymbol{x}') \geq 0 \tag{3.13}$$

- the value of the smoothing function should decrease with the increase of the distance from the particle at $\boldsymbol{x}$. The influence of the nearest particles must be greater.

- the smoothing function must be an even function: particles at the same distance from the particle at $\boldsymbol{x}$ should have the same effect on that particle. Finally,
- the smoothing function should be smooth enough to ensure a better approximation.

In Abaqus/Explicit, the kernel function used is the cubic spline function (Dassault Systèmes Simulia Corp., 2020) initially used by Monaghan and Lattanzio (1985) as reported by Liu and Liu (2016) :

$$W(R,h) = \alpha_d \times \begin{cases} \frac{2}{3} - R^2 + \frac{R^3}{2} & 0 \le R < 1 \\ \frac{2 - R^3}{6} & 1 \le R < 2 \\ 0 & R \ge 2 \end{cases} \tag{3.14}$$

where $R = r/h = |\boldsymbol{x} - \boldsymbol{x}'|/h$ is the relative distance between two points (particles) at $\boldsymbol{x}$ and $\boldsymbol{x}'$ and,

$$\alpha_d = \begin{cases} \frac{1}{h} & \text{in one} - \text{dimensional space} \\ \frac{15}{7\pi h^2} & \text{in two} - \text{dimensional space} \\ \frac{315}{208\pi h^3} & \text{in three} - \text{dimensional space} \end{cases}$$

The smoothing length (h) in ABAQUS is chosen by default such as the number of particles in the influence area is between 50 and 60 (Dassault Systèmes Simulia Corp., 2020).

3.4.4 SPH Model for Solid Mechanics

3.4.4.1 Governing equations

As used by Huang et al. (2014), the Smoothed Particle Hydrodynamics (SPH) model for solid mechanics and for continuum mechanics were based on the Drucker-Prager material law. Here, two sets of partial differential equations are used for describing the conservation of mass and momentum as presented by Eq. (3.15) and Eq. (3.16), respectively (Bui et al., 2008; Kermani & Qiu, 2018).

$$\frac{D\rho}{Dt} = -\rho \frac{\partial v^{\alpha}}{\partial x^{\alpha}} \tag{3.15}$$

$$\frac{Dv^{\alpha}}{Dt} = \frac{1}{\rho} \frac{\partial \sigma^{\alpha\beta}}{\partial x^{\beta}} + f^{\alpha} \tag{3.16}$$

where:

$\frac{D}{Dt} = \frac{\partial}{\partial t} + v^{\alpha} \frac{\partial}{\partial x^{\alpha}}$ is the material derivative.

α and β denote coordinate directions,

ρ is the material (or soil) density,

$\sigma^{\alpha\beta}$ is the total stress tensor,

v stands for the velocity, and

f^{α} is the component of the acceleration caused by external forces such as gravity force, among others.

The total stress is given by the following equation (Kermani & Qiu, 2018):

$$\sigma^{\alpha\beta} = -P\delta^{\alpha\beta} + s^{\alpha\beta} \tag{3.17}$$

where

δ is the Kronecker's delta defined by $\delta^{\alpha\beta} = \begin{cases} 1, & \alpha = \beta \\ 0, & \alpha \neq \beta \end{cases}$

α and β denote coordinate directions,

P is the hydrostatic pressure of granular material given in Eq. (3.18) by Kermani and Qiu (2018)

$$P = -\frac{\sigma^{\gamma\gamma}}{3} = -\frac{\sigma^{xx} + \sigma^{yy} + \sigma^{zz}}{3} \tag{3.18}$$

where $\sigma^{\gamma\gamma}$ represents the sum of principal stresses components in x, y and z principal directions; $\sigma^{xx}, \sigma^{yy}, \sigma^{zz}$ are the principal stresses component in x, y and z directions where $\tau = 0$. Conventionally, the negative sign in Eq. (3.18) will denote compressive stresses.

3.4.4.2 Soil constitutive modelling

For an elastic-plastic material, it is generally admitted (see e.g. (Bui et al., 2008), (Huang et al., 2014) and (Kermani & Qiu, 2018)) that the strain rate tensor $\dot{\varepsilon}^{\alpha\beta}$ is the sum of an elastic strain rate tensor component $\dot{\varepsilon}_e^{\alpha\beta}$ and a plastic strain rate tensor component $\dot{\varepsilon}_p^{\alpha\beta}$, i.e.

$$\dot{\varepsilon}^{\alpha\beta} = \dot{\varepsilon}_e^{\alpha\beta} + \dot{\varepsilon}_p^{\alpha\beta} \tag{3.19}$$

The elastic strain rate tensor $\dot{\varepsilon}_e^{\alpha\beta}$ is simply deduced from Hooke's law as follows:

$$\dot{\varepsilon}_e^{\alpha\beta} = \frac{\dot{s}^{\alpha\beta}}{2G} + \frac{1}{9K}\dot{\sigma}^{\gamma\gamma}\delta^{\alpha\beta} \tag{3.20}$$

where:

$\dot{S}^{\alpha\beta}$ is the deviatoric shear stress rate tensor,

K denotes the elastic bulk modulus $K = E/3(1-2\upsilon)$

$G = 2(1+\upsilon)E$ is the shear modulus,

υ is Poisson's coefficient,

E is Young's modulus, and

$\dot{\sigma}^{\gamma\gamma}$ is the rate of change of the sum of the normal stress components in x, y and z directions.

The plastic strain rate tensor is described with the plastic flow rule as:

$$\dot{\varepsilon}_p^{\alpha\beta} = \dot{\lambda}\frac{\partial g}{\partial \sigma^{\alpha\beta}} \tag{3.21}$$

where $\dot{\lambda}$ is the rate of change of the plastic multiplier λ and g is the plastic potential function.

Using equation (3.20) and (3.21), the total strain rate tensor as presented by Bui et al. (2008) becomes:

$$\dot{\varepsilon}^{\alpha\beta} = \frac{\dot{s}^{\alpha\beta}}{2G} + \frac{1-2\upsilon}{3E}\dot{\sigma}^{\gamma\gamma}\delta^{\alpha\beta} + \dot{\lambda}\frac{\partial g}{\partial \sigma^{\alpha\beta}} \tag{3.22}$$

The total stress tensor $\sigma^{\alpha\beta}$ is defined as:

$$\sigma^{\alpha\beta} = s^{\alpha\beta} + \frac{1}{3}\sigma^{\gamma\gamma}\delta^{\alpha\beta} \tag{3.23}$$

After development and the use of the total stress tensor, the following general expression is obtained for an elastic-plastic material, as shown by Bui et al. (2008):

$$\dot{\sigma}^{\alpha\beta} = 2G\dot{e}^{\alpha\beta} + K\dot{\varepsilon}^{\gamma\gamma}\delta^{\alpha\beta} - \dot{\lambda}\left[\left(K - \frac{2G}{3}\right)\frac{\partial g}{\partial \sigma^{mn}}\delta^{mn}\delta^{\alpha\beta} + 2G\frac{\partial g}{\partial \sigma^{\alpha\beta}}\right] \tag{3.24}$$

where:

α and β are coordinate directions,

m, n are dummy indexes,

$\dot{e}^{\alpha\beta}$ is the deviatoric shear strain rate tensor $\dot{e}^{\alpha\beta} = \dot{\varepsilon}^{\alpha\beta} - \left(\frac{1}{3}\right)\dot{\varepsilon}^{\gamma\gamma}\delta^{\alpha\beta}$

The general expression for the plastic multiplier's rate of change $\dot{\lambda}$ is then obtained as follows (Bui et al., 2008):

$$\dot{\lambda} = \frac{2G\dot{\varepsilon}^{\alpha\beta}\frac{\partial f}{\partial \sigma^{\alpha\beta}} + \left(K - \frac{2G}{3}\right)\dot{\varepsilon}^{\gamma\gamma}\frac{\partial f}{\partial \sigma^{\alpha\beta}}\delta^{\alpha\beta}}{2G\frac{\partial f}{\partial \sigma^{mn}}\frac{\partial g}{\partial \sigma^{mn}} + \left(K - \frac{2G}{3}\right)\frac{\partial f}{\partial \sigma^{mn}}\delta^{mn}\frac{\partial g}{\partial \sigma^{mn}}\delta^{mn}} \tag{3.25}$$

Most of SPH applications use the Drucker-Prager constitutive model introduced by Drucker and Prager (1952) for its plastic potential function. The yield conditions for this model are shown in Figure 3-3 and may be written as:

$$f(I_1, J_2) = \sqrt{J_2} - \alpha_\phi I_1 - k_c = 0 \tag{3.26}$$

where:

I_1 is the first invariant of the stress tensor $I_1 = \sigma^{\gamma\gamma} = \sigma^{xx} + \sigma^{yy} + \sigma^{zz}$,

J_2 the second invariant of the deviatoric stress tensor $J_2 = \frac{1}{2}s^{\alpha\beta}s^{\alpha\beta}$,

α_ϕ and k_c the Drucker-Prager's constants related to the cohesion (c) and friction angle ϕ from the Coulomb's material model by the following expressions in Eq. (3.27) (Dassault Systèmes Simulia Corp., 2020):

$$\begin{cases} \alpha_\phi = \dfrac{tan\,\phi}{\sqrt{9 + tan^2\,\phi}} \\ k_c = \dfrac{3c}{\sqrt{9 + 12\,tan^2\,\phi}} \end{cases}$$

In plane strain conditions (Bui et al., 2008) (3.27)

$$\begin{cases} \tan\alpha_\phi = \dfrac{6\sin\phi'}{3 - \sin\phi'} \\ k_c = \dfrac{18c\cos\phi'}{3 - \sin\phi'} \end{cases}$$

When matching triaxial test response (Helwany, 2007); (Dassault Systèmes Simulia Corp., 2020) (3.28)

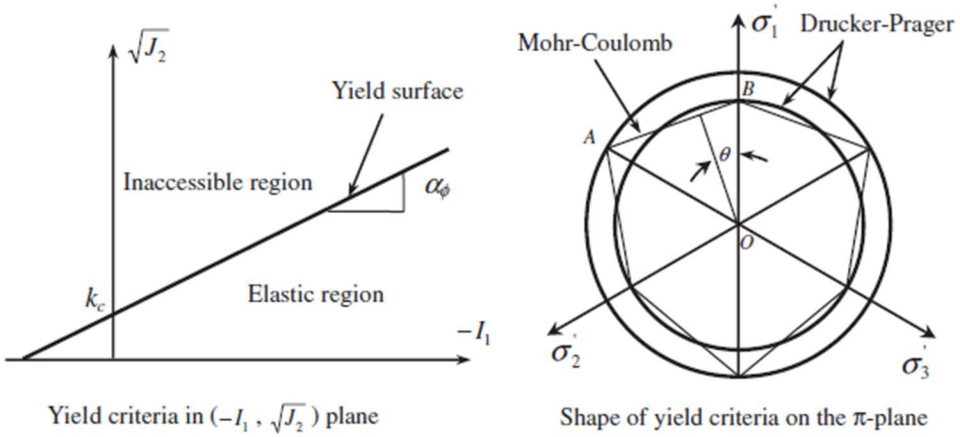

Figure 3-3 Drucker-Prager yield criterion (Bui et al., 2008).

In Figure 3-3, θ denotes the Lode's angle in deviator plane (Chen & Han, 2007) and it is defined by Eq. (3.29) as:

$$\theta = \frac{1}{3}\cos^{-1}\left[\frac{3\sqrt{3}J_3}{2J_2^{1.5}}\right] \tag{3.29}$$

where:

J_3 the third invariant of the stress deviator tensor i.e. $J_3 = \frac{1}{3}s_{ij}s_{jk}s_{ki}$ (Chen & Han, 2007).

Regarding the plastic potential function, two models are generally used in the Smoothed Particle Hydrodynamics (SPH) description: The associated plastic flow rule in which the plastic potential flow is expressed as the yield criterion ($g = \sqrt{J_2} + \alpha_\phi I_1 - k_c$) and the non-associated flow rule represented by the following expression $g = \sqrt{J_2} + 3I_1 \sin\psi$, with ψ denoting the dilatancy angle. Using the two-plastic potential functions in equations (3.24) and (3.25), we can obtain the final expression for an elastic-perfectly plastic material, that is (Bui et al., 2008):

for the associated flow rule:

$$\dot{\sigma}^{\alpha\beta} = 2G\dot{e}^{\alpha\beta} + K\dot{\varepsilon}^{\gamma\gamma}\delta^{\alpha\beta} - \dot{\lambda}\left[3\alpha_\phi K\delta^{\alpha\beta} + \frac{G}{\sqrt{J_2}}s^{\alpha\beta}\right] \tag{3.30}$$

$$\dot{\lambda} = \frac{3\alpha_\phi K\dot{\varepsilon}^{\gamma\gamma} + \left(G/\sqrt{J_2}\right)s^{\alpha\beta}\dot{\varepsilon}^{\alpha\beta}}{9\alpha_\phi^2 K + G} \tag{3.31}$$

and, for the non-associated flow rule:

$$\dot{\sigma}^{\alpha\beta} = 2G\dot{e}^{\alpha\beta} + K\dot{\varepsilon}^{\gamma\gamma}\delta^{\alpha\beta} - \dot{\lambda}\left[9K\,sin\,\psi\,\delta^{\alpha\beta} + \frac{G}{\sqrt{J_2}}s^{\alpha\beta}\right] \tag{3.32}$$

$$\dot{\lambda} = \frac{3\alpha K\dot{\varepsilon}^{\gamma\gamma} + \left(G/\sqrt{J_2}\right)s^{\alpha\beta}\dot{\varepsilon}^{\alpha\beta}}{27\alpha_\phi K\,sin\,\psi + G} \tag{3.33}$$

For problems with large deformations, an invariant stress rate is necessary, thus the Jaumann stress rate is used (Bui et al., 2008):

$$\hat{\dot{\sigma}}^{\alpha\beta} = \dot{\sigma}^{\alpha\beta} - \sigma^{\alpha\gamma}\dot{\omega}^{\beta\gamma} - \sigma^{\gamma\beta}\dot{\omega}^{\alpha\gamma} \tag{3.34}$$

where the spin rate tensor $\dot{\omega}^{\alpha\beta}$ is defined as:

$$\dot{\omega}^{\alpha\beta} = \frac{1}{2}\left(\frac{\partial v^{\alpha}}{\partial x^{\beta}} - \frac{\partial v^{\beta}}{\partial x^{\alpha}}\right) \tag{3.35}$$

With application of equations (3.34) and (3.35), the final expressions for an elastic-perfectly plastic material become (Bui et al., 2008):

For the associated flow rule:

$$\dot{\sigma}^{\alpha\beta} - \sigma^{\alpha\gamma}\dot{\omega}^{\beta\gamma} - \sigma^{\gamma\beta}\dot{\omega}^{\alpha\gamma} = 2G\dot{e}^{\alpha\beta} + K\dot{\varepsilon}^{\gamma\gamma}\delta^{\alpha\beta} - \dot{\lambda}\left[3\alpha_{\phi}K\delta^{\alpha\beta} + \frac{G}{\sqrt{J_2}}s^{\alpha\beta}\right] \tag{3.36}$$

For the non-associated flow rule:

$$\dot{\sigma}^{\alpha\beta} - \sigma^{\alpha\gamma}\dot{\omega}^{\beta\gamma} - \sigma^{\gamma\beta}\dot{\omega}^{\alpha\gamma} = 2G\dot{e}^{\alpha\beta} + K\dot{\varepsilon}^{\gamma\gamma}\delta^{\alpha\beta} - \dot{\lambda}\left[9K\sin\psi\,\delta^{\alpha\beta} + \frac{G}{\sqrt{J_2}}s^{\alpha\beta}\right] \tag{3.37}$$

3.4.5 SPH formulation of governing and constitutive equations

3.4.5.1 Equation of continuity

Using derivative properties, the right hand side of the continuity equation (i.e. equation (3.15)) becomes (Huang et al., 2014):

$$-\rho\frac{\partial v^{\alpha}}{\partial x^{\alpha}} = -\left[\frac{\partial}{\partial x^{\alpha}}(\rho v^{\alpha}) - v^{\alpha}\cdot\frac{\partial \rho}{\partial x^{\alpha}}\right] \tag{3.38}$$

The equation of continuity is then expressed as:

$$\frac{D\rho}{Dt} = -\frac{\partial(\rho v^{\alpha})}{\partial x^{\alpha}} + v^{\alpha}\frac{\partial \rho}{\partial x^{\alpha}} \tag{3.39}$$

Using the SPH particle formulation on the equation above, we obtain (Huang et al., 2014):

$$\frac{D\rho_i}{Dt} = -\sum_{j=1}^{N} \frac{m_j}{\rho_j} \rho_j v_j^{\alpha} \frac{\partial W_{ij}}{\partial x_i^{\alpha}} + v_i^{\alpha} \sum_{j=1}^{N} \frac{m_j}{\rho_j} \rho_j \frac{\partial W_{ij}}{\partial x_i^{\alpha}} = \sum_{j=1}^{N} m_j \left(v_i^{\alpha} - v_j^{\alpha}\right) \frac{\partial W_{ij}}{\partial x_i^{\alpha}} \tag{3.40}$$

3.4.5.2 Equation of momentum

Using derivative properties, the first right hand side of the momentum equation (equation (3.16)) can also be rewritten as follows (Huang et al., 2014):

$$\frac{1}{\rho} \frac{\partial \sigma^{\alpha\beta}}{\partial x^{\beta}} = \frac{\partial}{\partial x^{\beta}} \left(\frac{\sigma^{\alpha\beta}}{\rho} \right) + \frac{\sigma^{\alpha\beta}}{\rho^2} \frac{\partial \rho}{\partial x^{\beta}} \tag{3.41}$$

The momentum equation then becomes:

$$\frac{Dv^{\alpha}}{Dt} = \frac{\partial}{\partial x^{\beta}} \left(\frac{\sigma^{\alpha\beta}}{\rho} \right) + \frac{\sigma^{\alpha\beta} \frac{\partial \rho}{\partial x^{\beta}}}{\rho^2} + f^{\alpha} \tag{3.42}$$

The SPH particle approximation is then:

$$\begin{aligned} \frac{Dv_i^{\alpha}}{Dt} &= \frac{\sigma_i^{\alpha\beta}}{\rho_i^2} \sum_{j=1}^{N} \frac{m_j}{\rho_j} \rho_j \frac{\partial W_{ij}}{\partial x_i^{\beta}} + \sum_{j=1}^{N} \frac{m_j}{\rho_j} \frac{\sigma_j^{\alpha\beta}}{\rho_j} \frac{\partial W_{ij}}{\partial x_i^{\beta}} + f_i^{\alpha} \\ &= \sum_{j=1}^{N} m_j \left(\frac{\sigma_i^{\alpha\beta}}{\rho_i^2} + \frac{\sigma_j^{\alpha\beta}}{\rho_j^2} \right) \frac{\partial W_{ij}}{\partial x_i^{\beta}} + f_i^{\alpha} \end{aligned} \tag{3.43}$$

To avoid numerical oscillation and penetration between particles, it is required to add an additional artificial viscosity term $\boldsymbol{\Pi_{ij}}$ in the equation of motion (Huang et al., 2014).

$$\frac{Dv_i^\alpha}{Dt} = \sum_{j=1}^{N} m_j \left(\frac{\sigma_i^{\alpha\beta}}{\rho_i^2} + \frac{\sigma_j^{\alpha\beta}}{\rho_j^2} - \delta^{\alpha\beta} \Pi_{ij} \right) \frac{\partial W_{ij}}{\partial x_i^\beta} + f_i^\alpha \tag{3.44}$$

with

$$\Pi_{ij} = \frac{-a\bar{c}\mu_{ij} + b(\mu_{ij})^2}{\overline{\rho^{\alpha\beta}}} \tag{3.45}$$

$$\mu_{ij} = \frac{h(v_i - v_j)\sqrt{(x_i - x_j)^2 + (y_i - y_j)^2}}{(x_i - x_j)^2 + (y_i - y_j)^2 + kh^2} \tag{3.46}$$

$$\bar{c} = \frac{1}{2}(c_i - c_j) \tag{3.47}$$

$$\bar{\rho} = \frac{1}{2}(\rho_i - \rho_j) \tag{3.48}$$

where

a and b are constants, usually equal to 1 (Huang et al., 2014),

k is a free parameter, usually equal to 0.01 (Huang et al., 2014),

c_i and c_j denote the velocity of sound at point i and j, respectively.

3.4.5.3 Constitutive equations

For a particle i, the SPH formulation of the stress-strain relation is given below for the associated and non-associated flow rules soil models (Bui et al., 2008):

For the associated flow rule:

$$\frac{D\sigma_i^{\alpha\beta}}{Dt} = \sigma_i^{\alpha\gamma}\dot{\omega}_i^{\beta\gamma} + \sigma_i^{\gamma\beta}\dot{\omega}_i^{\alpha\gamma} + 2Ge_i^{\alpha\beta} + K\dot{\varepsilon}_i^{\gamma\gamma}\delta_i^{\alpha\beta} - \dot{\lambda}_i\left[3\alpha_\phi K\delta^{\alpha\beta} + \frac{G}{\sqrt{J_2}}s_i^{\alpha\beta}\right] \quad (3.49)$$

where:

$$\dot{\lambda}_i = \frac{3\alpha_\phi K\dot{\varepsilon}_i^{\gamma\gamma} + \left(G/\sqrt{J_2}\right)s_i^{\alpha\beta}\dot{\varepsilon}_i^{\alpha\beta}}{9\alpha_\phi^2 K + G} \quad (3.50)$$

and for the non-associated flow rule:

$$\frac{D\sigma_i^{\alpha\beta}}{Dt} = \sigma_i^{\alpha\gamma}\dot{\omega}_i^{\beta\gamma} + \sigma_i^{\gamma\beta}\dot{\omega}_i^{\alpha\gamma} + 2Ge_i^{\alpha\beta} + K\dot{\varepsilon}_i^{\gamma\gamma}\delta_i^{\alpha\beta} - \dot{\lambda}_i\left[9K\sin\psi\,\delta^{\alpha\beta} + \frac{G}{\sqrt{J_2}}s_i^{\alpha\beta}\right] \quad (3.51)$$

$$\dot{\lambda}_i = \frac{3\alpha_\phi K\dot{\varepsilon}_i^{\gamma\gamma} + \left(G/\sqrt{J_2}\right)s_i^{\alpha\beta}\dot{\varepsilon}_i^{\alpha\beta}}{27\alpha_\phi K\sin\psi + G} \quad (3.52)$$

Finally, the strain and spin rate tensors are discretized for a particle i using the SPH formulation as (Bui et al., 2008):

$$\dot{\varepsilon}^{\alpha\beta} = \frac{1}{2}\left(\frac{\partial v^\alpha}{\partial x^\beta} + \frac{\partial v^\beta}{\partial x^\alpha}\right) = \frac{1}{2}\left[\sum_{j=1}^{N}\frac{m_j}{\rho_j}\left(v_j^\alpha - v_i^\alpha\right)\frac{\partial W_{ij}}{\partial x_i^\beta} + \sum_{j=1}^{N}\frac{m_j}{\rho_j}\left(v_j^\beta - v_i^\beta\right)\frac{\partial W_{ij}}{\partial x_i^\alpha}\right] \quad (3.53)$$

$$\dot{\omega}^{\alpha\beta} = \frac{1}{2}\left(\frac{\partial v^\alpha}{\partial x^\beta} - \frac{\partial v^\beta}{\partial x^\alpha}\right) = \frac{1}{2}\left[\sum_{j=1}^{N}\frac{m_j}{\rho_j}\left(v_j^\alpha - v_i^\alpha\right)\frac{\partial W_{ij}}{\partial x_i^\beta} - \sum_{j=1}^{N}\frac{m_j}{\rho_j}\left(v_j^\beta - v_i^\beta\right)\frac{\partial W_{ij}}{\partial x_i^\alpha}\right] \quad (3.54)$$

3.5 Use of the SPH technique in geotechnical engineering

3.5.1 Modeling of slope stability using the SPH method

The smoothed particle hydrodynamics method has been used by many authors in the geotechnical field, mostly for assessing and analysing the stability of slopes in granular media. Some of these authors used the SPH model which is implemented in Abaqus/Explicit software, but most of them performed SPH analyses using numerical codes that they had programmed themselves.

In the following, we present two numerical applications obtained by Kitano et al. (2016) and An et al. (2016) in order to show the relevance of the SPH method in geotechnical applications.

Kitano et al. (2016) studied the effect of the failure of an embankment slope on a buried pipeline using a combined finite element method (FEM) and smoothed particle method implemented and built in Abaqus 6.14. Figure 3-4 shows the model used in their study based on the large scale experiment of Itoh and Toyosawa (2009) and the analytical research of Nonoyama et al. (2012).

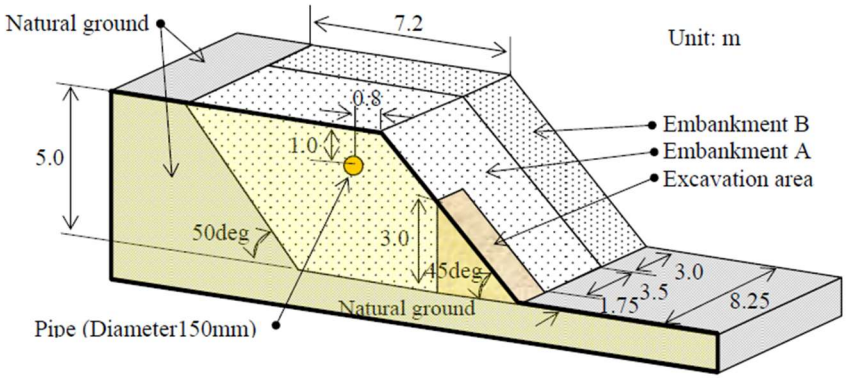

Figure 3-4 Model of analysis (Kitano et al., 2016)

The natural ground and the embankments (Figure 3-4) are modeled as elasto-plastic materials using the Mohr-Coulomb's failure criterion. The pipe is also modeled as an elasto-plastic material with a nominal stress-strain relationship. Kitano et al. (2016) analysis is divided in two steps: in step 1, a gravity load analysis of 1 second of duration is performed, and in step 2, the slope failure analysis of 4 seconds of duration is performed by removing the excavated area. Three different analyses have been performed based on the conversion of embankment A (Figure 3-4) into SPH particles:

1. The first one is a finite element analysis performed with Abaqus/Explicit, by using its explicit dynamic procedures. During this first step, none of the elements have been converted into smoothed particles and therefore no SPH analysis has been performed yet.
2. In the second analysis, the material of embankment A was converted in SPH particles at the beginning of the slope failure analysis, i.e., at time t = 1 second or 1 s (time-based criterion).
3. In the third and last analysis, embankment A was converted in SPH particles when the absolute value of the maximum principal strain reaches a threshold of 30% (strain-based criterion).

For the first analysis, the slope failure cannot be shown or represented due to the use of a continuum finite element analysis. For the second analysis which is using the SPH method and where the material of embankment A has been converted to SPH particles at the beginning of the slope failure analysis, a large force is applied to the buried pipeline at an early stage. As for the last analysis, the strain-based criterion is the fitting in their case. The authors concluded that the FEM-SPH method using the strain-based criterion is the best analysis model that can be used to study the effect of the failure of a slope on the buried pipe because the progression of the slope failure is the most consistent with the large-scale experiment. They also confirmed that the soil surrounding the pipe has an important effect on the pipe during the failure as the pressure generated a large amount of stress in the pipe and moved it in the direction of the slope failure.

An et al. (2016) developed a three-dimensional model using smoothed particle hydrodynamics to study the progression of large deformation and failure of slopes. The soil is assumed to behave as an elasto-plastic material using the Drucker-Prager model with the non-associated plastic flow rule. The authors used two examples to verify their SPH model: 1) a two-dimensional clay slope failure by strength reduction technique, and 2) a three-dimensional granular material slope failure.

For the two-dimensional case their results are consistent with the example results and the result of the limit equilibrium method. The three-dimensional example results show a little overestimation of the elevation and a slight underestimation of the slide width at the toe. They concluded that in general the results of their three-dimensional model are acceptable. The next step for the authors

was to apply their model to study two special three-dimensional slope configurations: a curving slope surface (Figure 3-5 a, b and c) and a turning corners slope (Figure 3-5 d and e) as shown in Figure 3-5.

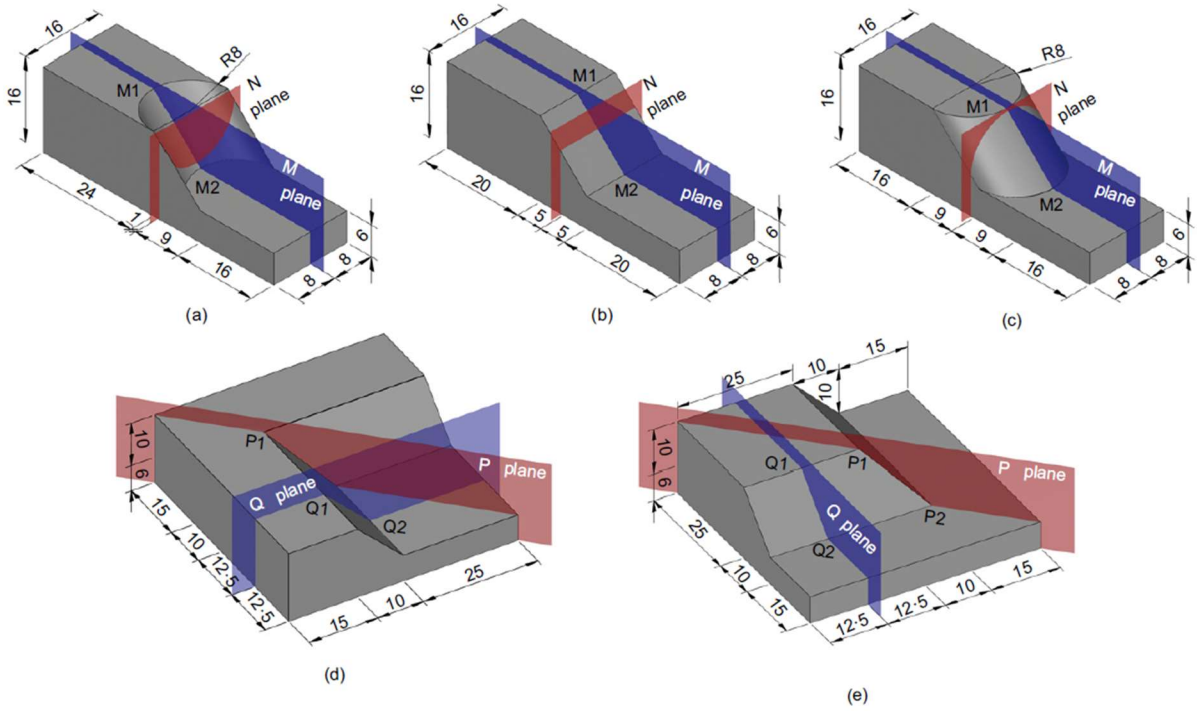

Figure 3-5 Three-dimensional slope configurations. Curving slope surface: a) concave surface, b) common surface, c) convex surface. Turning corners slope: d) concave subbase, e) convex subbase (An et al., 2016)

An et al. (2016) noted that the SPH method used describe well the entire process of the slope failure, from the occurrence and development of the failure to the final stable state. They also concluded that the final profile of a slope failure is related to its initial configuration, thus results of three-dimensional simulations are different from two-dimensional analyses. For the curving slopes, the concave slope plastic area is thinner than the convex one with the common slope plastic area in between. The settlement distance of the top and the slope toe translation distance of the convex slope are greater than the two-dimensional one. The authors noted that the opposite has been observed for the concave and the common slope. Finally, for the two subbases model, the difference is even greater with small displacement at the corner toe of the two models with

instability more likely to occur at the top corner for the convex subbase and at the side slope of the concave subbase.

3.5.2 Modeling of granular flow using the SPH method

Chen and Qiu (2012) used the smoothed particle hydrodynamics for assessing the flow of granular materials submitted to extreme deformation. These authors assumed that the modeled granular material behaves plastically by obeying the Drucker-Prager constitutive model with the use of a non-associated flow rule in the continuum scheme. Moreover they first validated their SPH model with experimented study conducted by Bui et al. (2008) and Lube et al. (2005).

Bui et al. (2008) conducted an experimental test in which aluminum bars were used for the simulation of granular flow. Bui et al. also conducted a two-dimensional SPH simulation from which it was concluded that numerical results were found to be in good agreement with experimentally measured test results.

Lube et al. (2005) performed a three-dimensional experimentation using real granular materials such as sand, sugar, and rice. Here again, the numerical results deduced from SPH simulations performed by the authors were found to be in good agreement with the measured experimental findings.

After validation of their model, Chen and Qiu (2012) performed a three-dimensional SPH simulation representing the experimental collapse of a three-dimensional axisymmetric vertical column of granular material (sand, sugar, and rice) performed by Lube et al. (2004). The simulations were performed using different values of the aspect ratio a defined as

$$a = \frac{h_i}{r_i} \tag{3.55}$$

where

h_i is the initial height of the column of granular material, and

r_i is the initial radius of the column of granular material.

The results shown in Figure 3-6 show that:

- the final runout distance and final profile are nearly independent of the material properties (bulk modulus and Poisson's ratio), except for the frictional angle which has an influence on the final configuration;
- the aspect ratio has an influence on the granular material flow pattern: for small aspect ratios, the top surface is undisturbed and only the material on the edge of the initial column is disturbed (Figure 3-6). Moreover, for larger aspect ratios, more granular particles are disturbed with a tip at the top for the final configuration;
- the aspect ratio has an influence on the final runout distance and the final deposit height;
- the non-disturbed region of the sand column in the performed simulation is smaller than the experimental one. For the authors, this might be explained by the precision of the numerical simulation able to record smaller deformations which in the test they may not be visually easily detectable.
- the use of the developed SPH model is effective for large deformation and dense flow of granular material.

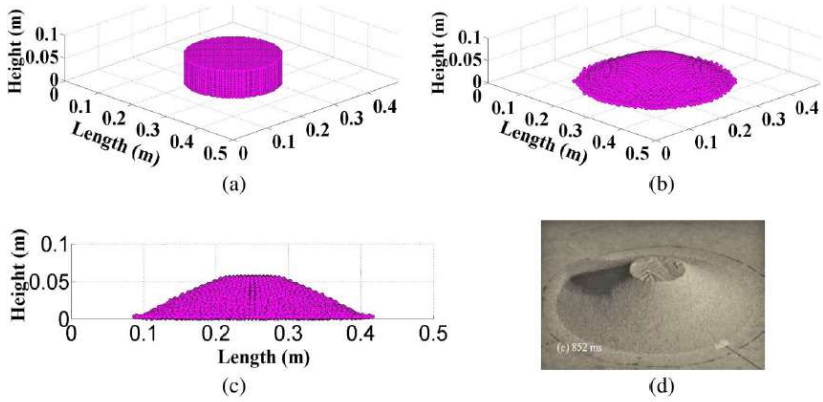

Figure 3-6 : Comparison of SPH simulation and experiment with $a = 0.55$: (a) initial configuration of sand column; (b) simulated final profile after collapse; (c) side view of simulated final profile; (d) experimental final profile by Lube et al. (2004). (Chen & Qiu, 2012).

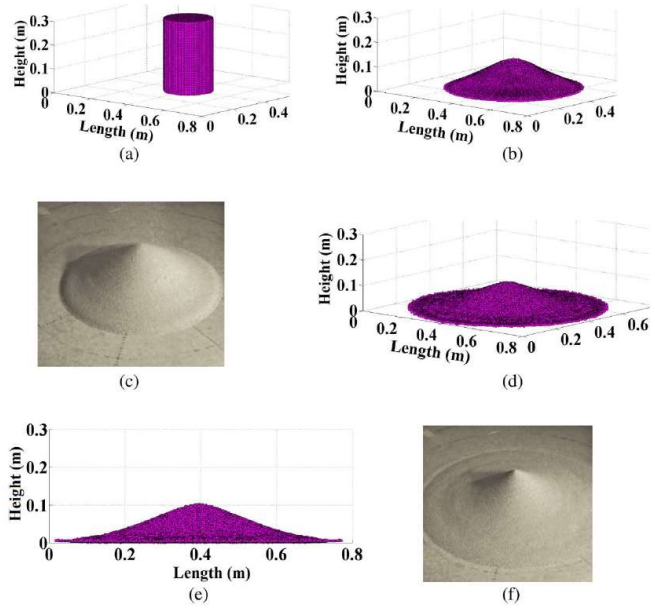

Figure 3-7 : Comparison between SPH simulation and experiment with $a = 2.75$: (a) initial configuration of sand column; (b) simulated flow during collapse; (c) experimental flow during collapse by Lube et al. (2004); (d) simulated final profile after collapse; (e) side view of simulated final profile; and (f) experimental final profile by Lube et al. (2004). (Chen & Qiu, 2012).

Kermani and Qiu (2018) developed a three-dimensional SPH model to investigate the collapse of quasi-static and dynamic collapses of granular materials as well as the intermediate behavior between the two types of collapses. They used the Drucker-Prager constitutive model with the non-associated flow rule for modeling the sand in the SPH formulations. A representation of the three-dimensional SPH model used by the authors is presented in Figure 3-8. For all models, only the value of the height (h_i) is variable, giving different values of the aspect ratio, as defined by equation (3.55).

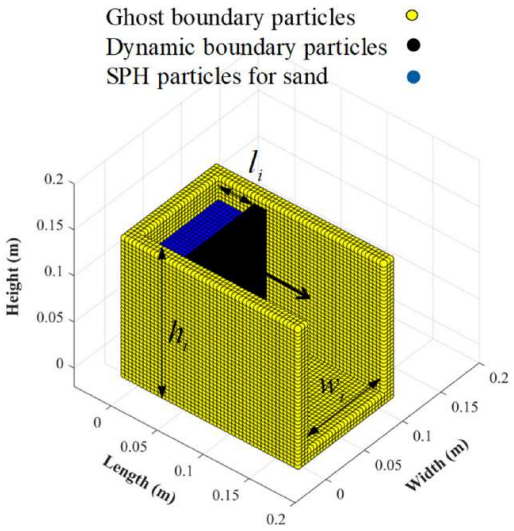

Figure 3-8 : Schematics of SPH 3D model (Kermani & Qiu, 2018).

The quasi-static numerical simulation models the physical experiment made by Meriaux (2006). Here, the black particles in Figure 3-8 model the moving wall which retains the SPH particles of sand. This moving wall or simply the dynamic boundary of particles is slowly moved. The SPH predicted results by Kermani and Qiu (2018) are shown in Figure 3-9 to Figure 3-11 where t_n represents the normalized time as $t_n = \mathrm{t}/t_f$ and t_f the final time. For $a = 0.58$ (Figure 3-9), the sand particles located near the moving wall are only the ones being disturbed. For $a = 1.53$ (Figure 3-10), there is complete deformation of the top surface with an undisturbed region near the fixed wall. For $a = 3.0$ in Figure 3-11, most part of the sand mass is disturbed. Based on these observations, the authors made the following conclusions:

- the results are consistent with the findings of Meriaux (2006), Owen et al. (2009) and Zhang et al. (2016);
- the SPH simulations results are in accordance with the experiment and the theoretical calculations regarding the normalized final height, the runout distance, and the dissipated energy.

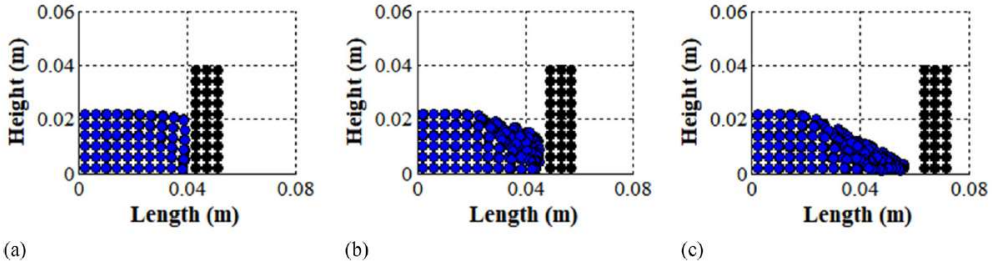

Figure 3-9 : Evolution of deposit profile for a column with $a = 0.58$: (a) $t_n = 0.06$; (b) $t_n = 0.36$; and (c) $t_n = 1.10$ (Kermani & Qiu, 2018).

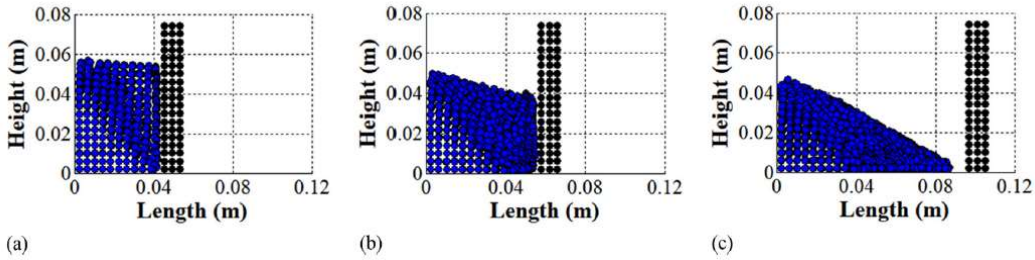

Figure 3-10 : Evolution of deposit profile for a column with $a = 1.53$: (a) $t_n = 0.06$; (b) $t_n = 0.30$; and (c) $t_n = 1.08$ (Kermani & Qiu, 2018).

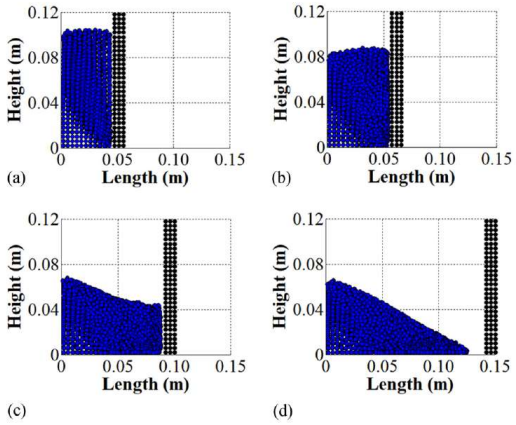

Figure 3-11 : Evolution of deposit profile for a column with $a = 3.0$: (a) $t_n = 0.06$; (b) $t_n = 0.17$; (c) $t_n = 0.55$; and (d) $t_n = 1.09$ (Kermani & Qiu, 2018).

For the dynamic collapse, the moving wall (black particles in Figure 3-9 to Figure 3-11) retaining SPH sand particles is suddenly removed. Kermani and Qiu (2018) observed two collapse patterns based on the initial aspect ratio. Final deposition for small aspect ratios shows a flat surface at the

top with a truncated wedgelike form. As for larger aspect ratios, the final deposition takes a wedgelike form with tip at the top. The authors concluded that:

- the results are consistent with the experimental findings of Lube et al. (2005), Lajeunesse et al. (2005) and Balmforth and Kerswell (2005) and the numerical results of Girolami et al. (2012) and Zhang et al. (2014);
- the velocity of the moving wall has relatively no influence on the normalized final height;
- the normalized runout distance, influenced by the inertia and the dynamic effect of the suddenly removed wall, is longer in the dynamic collapse.

3.5.3 Impact on a rigid retaining wall

Zhan et al. (2019) conducted a three-dimensional (3D) simulation using the SPH method in order to assess the impact of granular flow on rigid and deformable structures. They used a coupled total-Lagrangian and conventional Euler kernel based SPH (TL-CE SPH) method to model the interaction between the granular material and the rigid and deformable structures. The granular medium was modeled using the CESPH method, and the TLSPH method was used to model the rigid and deformable structures. The three distinct simulations, which all used the Drucker-Prager model, were performed by Zhan et al. (2019) in order to verify their proposed TL-CE SPH method, i.e.:

1. a granular collapse between two parallel planes to verify the performance of the method for granular modeling according to the experiments of Lube et al. (2005) and Lajeunesse et al. (2005) as well as the numerical simulations of Chen and Qiu (2012) and Kermani and Qiu (2018);
2. a quasi-static granular material at rest in a tank to verify the efficiency of the method for granular material and structures interaction where numerical results are compared to analytical calculations; and
3. a flexible retaining wall undergoing deformations and submitted to geo-stress to verify the efficiency of the method in the case of soil-structure interaction. The results are compared with FEM simulations result since there is no analytical solution for this case.

After validation of their model, Zhan et al. (2019) performed a three-dimensional simulation of the impact of granular flow on rigid and deformable structures.

The study of the impact on a rigid structure follows the experiments of Moriguchi et al. (2009) and the numerical analysis of He et al. (2018) and Fávero Neto and Borja (2018). The granular material (blue material in Figure 3-12) is placed on an inclined flume and starts flowing down toward the rigid wall (orange material in Figure 3-12) once the simulation is started. The result of their analysis shows that front particles accelerate until they reach the wall. After the impact a wedge is formed at the wall and continues to grow bigger until reaching the top surface of the wall and then particles start to overflow (Figure 3-13). The authors also observed that the interaction force between the particles and the wall is higher after the impact, then gradually decreases to approximately match the experiment and additional numerical simulations.

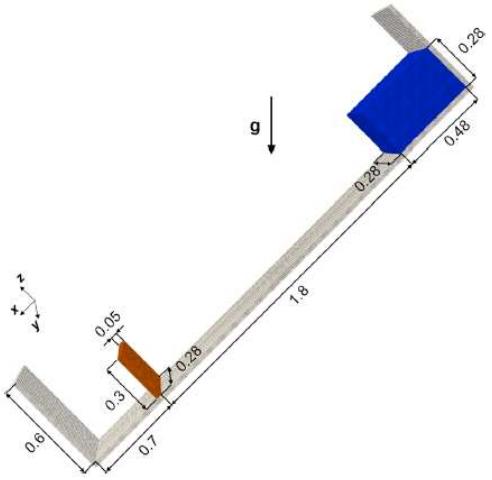

Figure 3-12: Initial configuration of the system: Granular flow impact on a rigid wall. Dimensions are in m (Zhan et al., 2019).

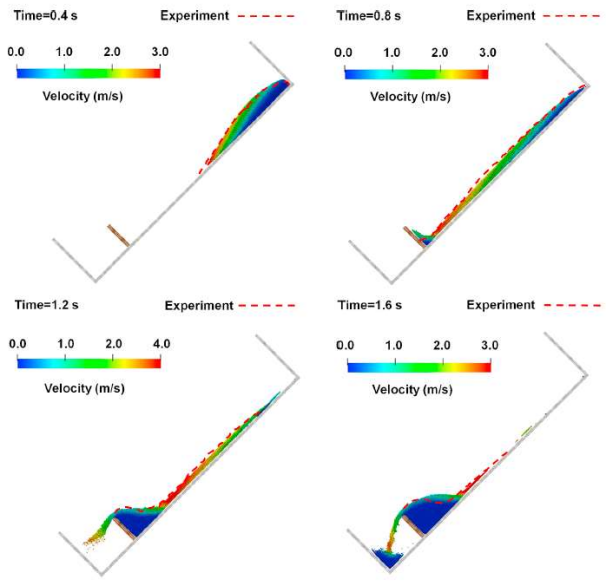

Figure 3-13: Configurations of the granular flow as well as the resultant velocity field at selected time instances (Zhan et al., 2019).

The authors performed analyses to assess the impact of a Drucker-Prager granular material on a deformable structure using a dam break test model. The model's configuration is presented in Figure 3-14. The confined sand column (blue material in Figure 3-14) is placed at the left end of the container and the deformable wall (orange material in Figure 3-14) is placed at the base of the container. The deformable wall is modeled using the Saint Venant-Kirchhoff material model. The collapse pattern of the sand particles is similar to regular granular collapse pattern. After the impact with the wall, high interaction forces are registered and the wall deforms until it reaches a steady state before the end of the simulation. Zhan et al. (2019) also noted that the vertical stress in the granular material does not always match the overburden stress and the maximum value of the stress is located at the bottom of the wall and a stress value of zero is registered at the top of the wall.

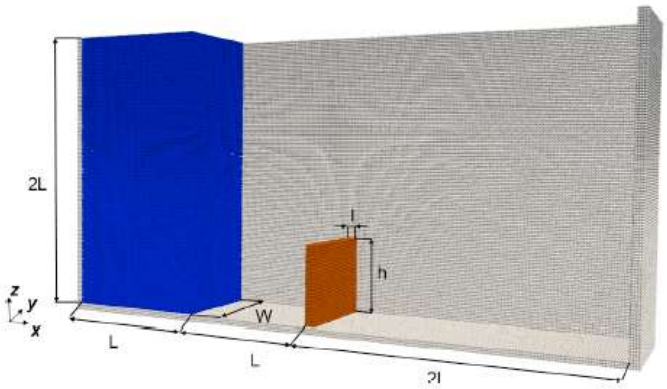

Figure 3-14 : Initial configuration of the system: Granular flow impact on a hyperelastic wall (Zhan et al., 2019).

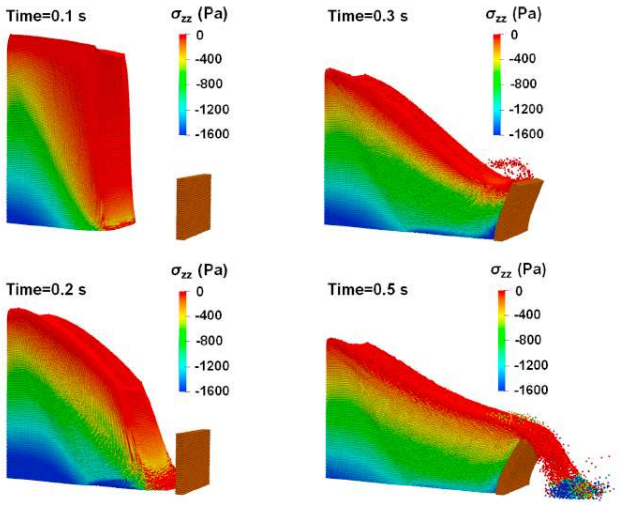

Figure 3-15 : Configurations of the granular flow and the elastic wall as well as the stress σ_{zz} field of granular material at selected time instances ($E_s = 1\text{MPa}$) (Zhan et al., 2019).

Zhou and Li (2022) studied the impact of tailings slurry on catch dams and the dynamic interaction between the tailings and the modelled catch dam during a breach of a tailing storage facility. They used LS_DYNA (Hallquist, 2007), a commercial finite element code in which the smoothed particle hydrodynamics method is built-in. The SPH model used is presented hereafter in Figure 3-16.

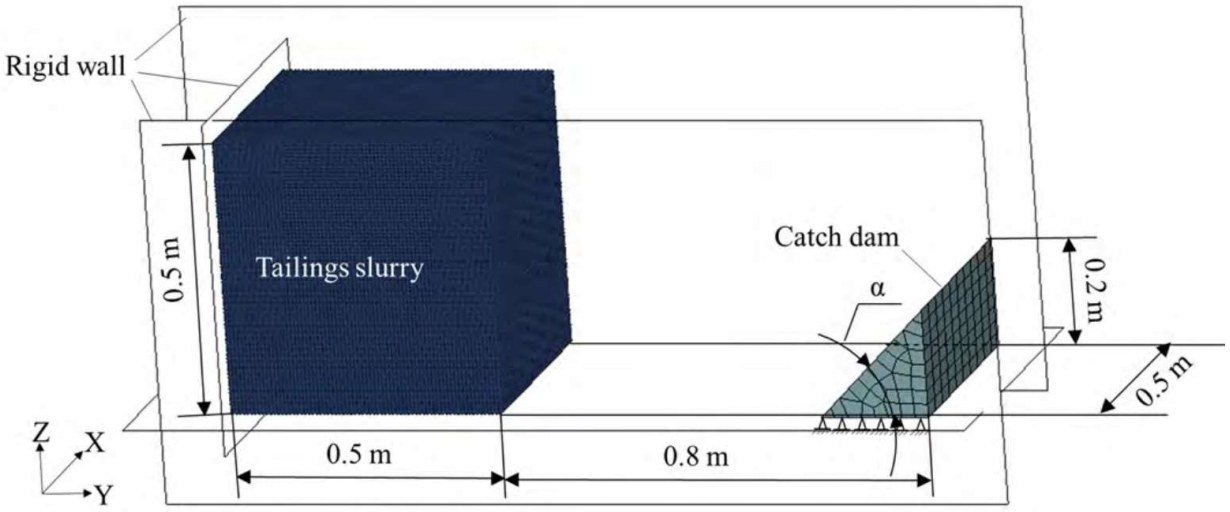

Figure 3-16 : Numerical model of the simulation of tailings pond break (Zhou & Li, 2022)

Zhou and Li (2022) studied the effects of different values of the angles (α) of the upstream slope of the catch dam. Figure 3-17 shows results of the flow process of the tailing particles from the tailings dam breach as presented by the authors.

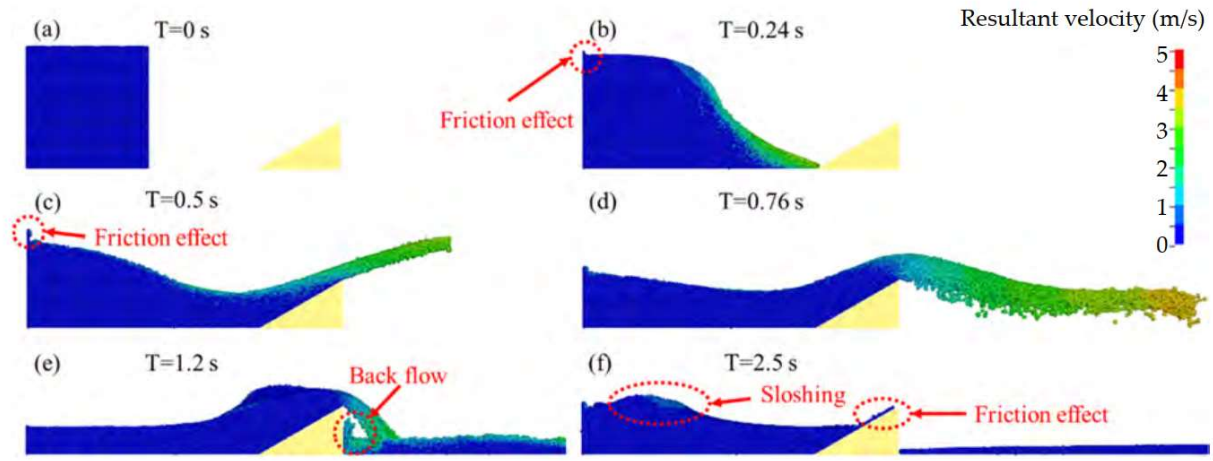

Figure 3-17 : Tailing particles flow stages for a catch dam with an upstream slope angle of 30° (Zhou & Li, 2022)

The flow process is composed of four successive steps:

- A first stage named “the initiation” which begins at time (T in seconds i.e. s) $T = 0s$ and ending at $T = 0.38s$ in which the tailing particles start moving and accelerate until reaching the toe of the catch dam that starts to be impacted.
- A second stage named herein “the peak stage” which starts at $T = 0.38s$ and ends at $T = 0.76s$. The system here exhibits a decrease of the kinetic energy and the impacting force at a first time followed by an increase of these two variables at a second later time till reaching a second peak.
- A third stage named by the authors “the ebb” starts at $T = 0.76s$ and ends at $T = 1.2s$. The crest of the tailing particles is moving back to the tailing pond with a decrease of the kinetic energy while impacting force does not vary much.
- The last stage is “the sloshing” starting at $T = 1.2s$ during which there is a back-and-forth movement of the tailing slurry between the tailing pond and the catch dam until the tailing slurry reach a state of equilibrium. During this stage the kinetic energy and the impacting force continuously decrease. Zhou and Li (2022) also studied the effect that the catch dam upstream slope inclination can have on the kinetic energy and the impacting forces (Figure 3-18).

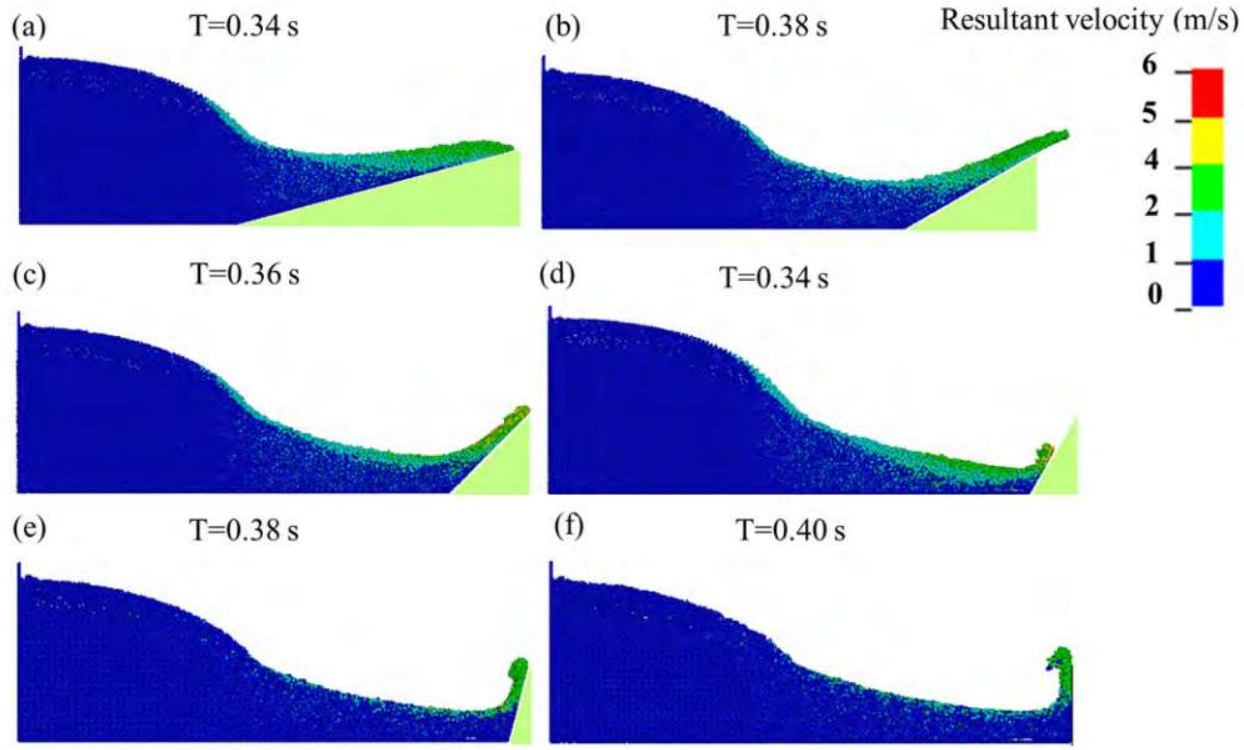

Figure 3-18 : Flow state of the tailings slurry with catch dams upstream slope inclinations from 15° to 90°: a) 15°; b) 30°; c) 45°; d) 60°; e) 75°; f) 90°.(Zhou & Li, 2022)

The authors concluded that to reduce the tailings slurry maximum velocity, the catch dam should be placed as close as possible of the tailing pond. But in this later position a second catch dam may be needed if the first one is not high enough. They also concluded that the best catch dams upstream slope inclination is between 30° and 37.5° and that a vertical catch dam construction should be avoided since the contact between the tailings slurry and the catch dam is smoother for small upstream slope inclinations.

CHAPTER 4 SPH MODELING OF VERTICAL MINE STOPES: EFFECT OF BACKFILLING MODE

4.1 Introduction and content of the chapter

The present chapter contains the main numerical works and simulations program performed in this thesis. Detailed descriptions and explanations of the conducted numerical program are given in the following paragraphs, including: i) descriptions of all interacting parts in all finite element (FE) and SPH analyses, ii) material properties of all parts involved in the performed simulations, iii) explanation of the analyses steps adopted for running FE and SPH analyses, definition of contact properties used in performing contact computations, iv) modeling of the applied loads on the whole assembled parts during the whole simulated backfilling event, v) construction of different meshes used in all simulations, and finally vi) presentation of all predicted numerical results, mainly curves showing distributions of contact pressures along contact interface paths (along the horizontal bottom of the excavation). Curves are shown for different times corresponding to different frames of the performed analyses.

4.2 The Mohr-Coulomb material model

In this thesis, the backfill granular soil was modeled as an elastic-plastic material for which the total strain ε_{ij} is composed of an elastic strain ε_{ij}^{e} and a plastic strain ε_{ij}^{p}.

$$\varepsilon_{ij} = \varepsilon_{ij}^{e} + \varepsilon_{ij}^{p} \tag{4.1}$$

Due to loading, the material has two regimes that are delimited by the yield criterion: the elastic and the plastic regime. The elastic behavior implemented in Abaqus/Explicit and used in this thesis is an isotropic linear elastic one. Generally such behavior is suitable for describing small elastic strains behavior that are recoverable and usually smaller than 5% (Dassault Systèmes Simulia Corp., 2020). The elastic strains are evaluated using Hooke's law in which the Young's modulus E and the Poisson's ratio ν of the isotropic elastic material are the same in the three directions X, Y, and Z. For a linear elastic isotropic material, the three dimensional stress-strain relationship is the following, as presented by Helwany (2007):

$$\begin{Bmatrix} \varepsilon_{11} \\ \varepsilon_{22} \\ \varepsilon_{33} \\ \varepsilon_{12} \\ \varepsilon_{13} \\ \varepsilon_{23} \end{Bmatrix} = \begin{bmatrix} 1/E & -\nu/E & -\nu/E & 0 & 0 & 0 \\ -\nu/E & 1/E & -\nu/E & 0 & 0 & 0 \\ -\nu/E & -\nu/E & 1/E & 0 & 0 & 0 \\ 0 & 0 & 0 & 1/2G & 0 & 0 \\ 0 & 0 & 0 & 0 & 1/2G & 0 \\ 0 & 0 & 0 & 0 & 0 & 1/2G \end{bmatrix} \cdot \begin{Bmatrix} \sigma_{11} \\ \sigma_{22} \\ \sigma_{33} \\ \sigma_{12} \\ \sigma_{13} \\ \sigma_{23} \end{Bmatrix} \quad (4.2)$$

where the shear modulus $G = E/2(1 + \nu)$.

As the stress on the material exceeds the yield stress, the material goes into plasticity and a part of the total strain is not recoverable (Dassault Systèmes Simulia Corp., 2020). The material behavior is then model using plasticity theories. In this study, the Mohr-Coulomb plasticity model was used in all simulations. The plasticity theory is usually formulated using three components:

- the yield surface which determines the threshold for which the material goes into plasticity;
- the flow rule which describes how the material flows beyond the yield surface;
- and the hardening rule that describes the evolution of the yield surface through loading (Dassault Systèmes Simulia Corp., 2020).

For the Mohr-Coulomb plasticity model, the material yield surface is a linear function of the material shear stress τ and the normal effective stress σ' at the same place at yield. As it can be observed in Figure 4-1, the yield line represents the tangent to the Mohr's circles of different stress states at yield.

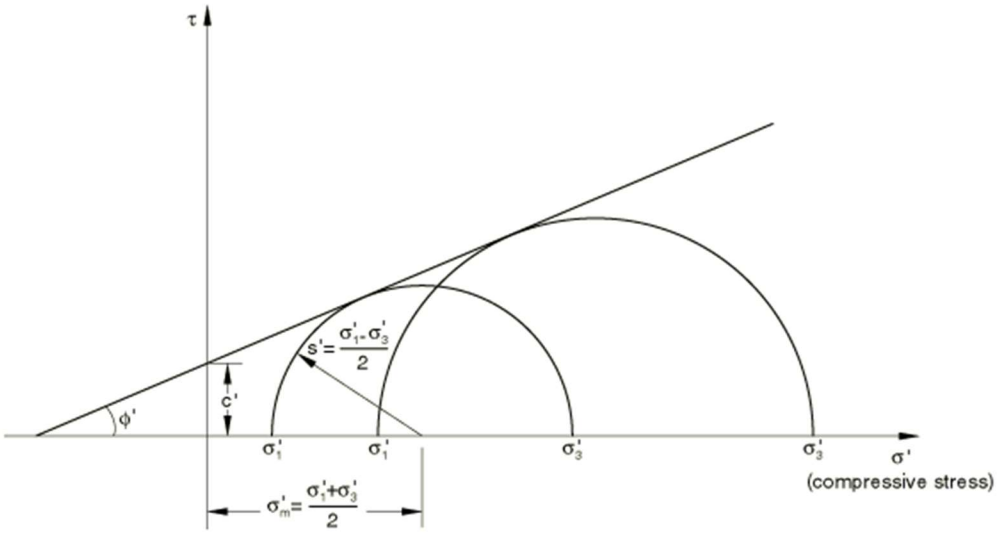

Figure 4-1 Mohr-Coulomb yield model.(Dassault Systèmes Simulia Corp., 2020)

The Mohr-Coulomb model is formulated as follows:

$$\tau = c' - \sigma' \tan \phi' \tag{4.3}$$

where

ϕ' is the material effective friction angle,

c' is the material effective cohesion, and

σ' is the positive effective compressive stress.

τ and σ' can be simply deduced from Mohr's circle as:

$\tau = s' \cos \phi'$ and

$\sigma' = \sigma'_m + s' \sin \phi'$.

By substituting τ and σ' in Eq. (4.3), we have:

$$s' + \sigma'_m \sin \phi' - c' \cos \phi' = 0 \tag{4.4}$$

where $s' = \frac{1}{2}(\sigma'_1 - \sigma'_3)$ is the maximum shear stress and,

$\sigma'_m = \frac{1}{2}(\sigma'_1 + \sigma'_3)$ is the equivalent pressure stress.

The general three-dimensional form of the Mohr-Coulomb plasticity criterion is expressed as (Dassault Systèmes Simulia Corp., 2020):

$$F = R_{mc}q - p'\tan\phi' - c' = 0 \tag{4.5}$$

with

$$R_{mc}(\Theta, \phi') = \frac{1}{\sqrt{3}\cos\phi'}\sin(\Theta + \frac{\pi}{3}) + \frac{1}{3}\cos(\Theta + \frac{\pi}{3})\tan\phi' \tag{4.6}$$

where Θ is the deviatoric polar angle described by $\cos(3\Theta) = \left(\frac{r}{q}\right)^3$,

$p' = \frac{\sigma'_{11} + \sigma'_{22} + \sigma'_{33}}{3}$ is the equivalent pressure stress,

$$q = \sqrt{\frac{1}{2}[(\sigma'_{11} - \sigma'_{22})^2 + (\sigma'_{22} - \sigma'_{33})^2 + (\sigma'_{33} - \sigma'_{11})^2] + 3(\sigma_{12}^2 + \sigma_{13}^2 + \sigma_{23}^2)}$$

$= \sqrt{\frac{3}{2}\boldsymbol{S}:\boldsymbol{S}}$ is the Mises equivalent stress, and

$r = \left(\frac{9}{2}\boldsymbol{S}\cdot\boldsymbol{S}:\boldsymbol{S}\right)$ is the third invariant of the deviatoric stress, and

$\boldsymbol{S} = \boldsymbol{\sigma} + p\boldsymbol{I}$ is the deviatoric stress.

The flow rule gives a relation between the plastic strain and the state of stress in the plastic regime, thus representing the evolution of the material flow beyond the yield stress, as presented in Figure 4-2 (Dassault Systèmes Simulia Corp., 2020).

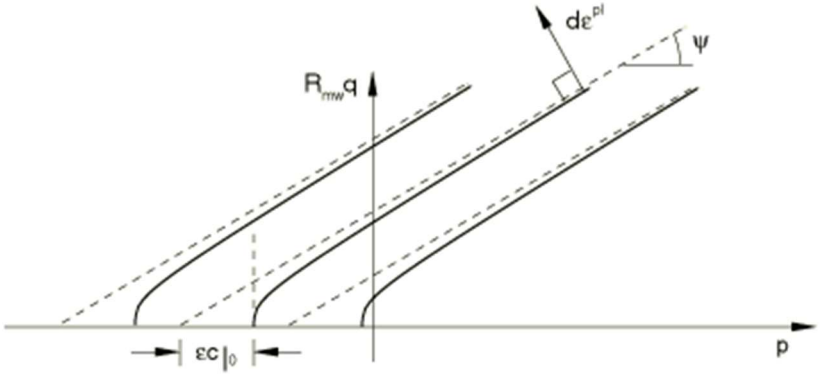

Figure 4-2 Set of hyperbolic flow potentials in the meridional stress plane (Dassault Systèmes Simulia Corp., 2020).

The flow rule is described as followed:

$$d\varepsilon_{ij}^{p} = \partial\lambda \frac{\partial G}{\partial \sigma_{ij}} \tag{4.7}$$

with $\partial\lambda$ the plastic multiplier's rate of change, function of the stress state and the load history and G the plastic flow potential for the Mohr-Coulomb criteria and the smooth elliptic function of Menétrey and William (1995) in the deviatoric stress, as referred in Figure 4-3 (Dassault Systèmes Simulia Corp., 2020) as follows:

$$G = \sqrt{(\epsilon c|_0 \tan\psi)^2 + (R_{mw} q)^2} - p\tan\psi \tag{4.8}$$

where $R_{mw}(\Theta, e) = \dfrac{4(1-e^2)\cos^2\Theta + (2e-1)^2}{2(1-e^2)\cos\Theta + (2e-1)\sqrt{4(1-e^2)\cos^2\Theta + 5e^2 - 4e}} R_{mc}\left(\dfrac{\pi}{3}, \phi'\right)$,

$$R_{mc}\left(\frac{\pi}{3}, \phi'\right) = \frac{3 - \sin\phi'}{6\cos\phi'}$$

ψ is the dilation angle measured in the $p - R_{mw}q$ plane at high confining pressure,

$c|_0 = c|_{\bar{\varepsilon}^{pl}=0}$ is the initial cohesion yield stress,

Θ is the deviatoric polar angle,

ϵ is the meridional eccentricity defining the rate of approach of the hyperbolic function to the asymptote, chosen as 0.1 by default,

$e = \frac{3 - \sin\phi'}{3 + \sin\phi'}$ is the deviatoric eccentricity.

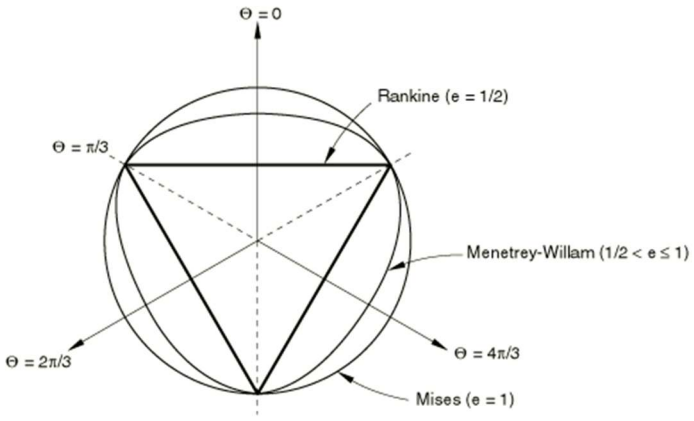

Figure 4-3 Menétrey-William flow potential in the deviatoric stress plane (Dassault Systèmes Simulia Corp., 2020).

For the hardening rule that defines the evolution of the yield surface through loading, a perfectly plastic behavior has been chosen for all simulations, thus there is no hardening or softening exhibited beyond yielding.

4.3 Explicit versus implicit dynamic procedures

The general dynamic equation of motion in mechanics is represented as:

$$\boldsymbol{M\ddot{d} + C\dot{d} + Kd = F} \tag{4.9}$$

where $\boldsymbol{M}$ represents the mass matrix,

$\boldsymbol{C}$ is the viscous damping matrix,

$\boldsymbol{K}$ is the stiffness matrix,

$\boldsymbol{F}$ is the vector of applied force,

$\boldsymbol{\ddot{d}}$ is the acceleration vector,

$\boldsymbol{\dot{d}}$ is the velocity vector, and

$\boldsymbol{d}$ is the displacement vector.

In Abaqus (2020), Eq. (4.9) is solved using direct integration of the system, implemented through two methods: i) the implicit direct integration in Abaqus/Standard using Hilber-Hughes-Taylor (Dassault Systèmes Simulia Corp., 2020) implicit operators, and ii) the explicit direct integration in Abaqus/Explicit using the central-difference operator. Analyses using the implicit dynamic procedure require that the operator matrix inversion and the resolution of a set of nonlinear equilibrium equations at each time increment and each one of them must converge. For the explicit dynamic analyses, there is no need to determine and to invert the global mass and stiffness matrices as displacement and velocities are directly calculated using known quantities at the beginning of each increment, thus the time requirement for each increment is small compared to an increment in an implicit dynamic analysis. However, for the explicit dynamic analysis a maximum size of time increment is required to have a stable solution which is not needed in the implicit analysis (Dassault Systèmes Simulia Corp., 2020).

In this study, some of simulations of backfilling processes were conducted using the explicit dynamic procedure implemented just in Abaqus/Explicit and based on an explicit solver and a finite difference operator.

The procedure for the explicit dynamic solver follows the central difference time integration rule performed at many small-time increments t. At the beginning of each time increment, the program solves the following dynamic Eq. (4.10) of motion and finds the accelerations at time t.

$$\boldsymbol{M\ddot{u} = P - I} \tag{4.10}$$

where $\boldsymbol{M}$ represents the mass matrix,

$\boldsymbol{P}$ is the applied load vector, and

$\boldsymbol{I}$ is the internal force vector.

The acceleration $\boldsymbol{\ddot{u}^N_{(i)}}$ is then used to determine the velocity solution $\boldsymbol{\dot{u}^N_{\left(i+\frac{1}{2}\right)}}$ to time $t + \Delta t/2$ (Eq. (4.11)) as well as the displacement solution $\boldsymbol{u^N_{(i+1)}}$ to time $t + \Delta t$ (Eq. (4.12) (Dassault Systèmes Simulia Corp., 2020)).

$$\dot{u}^N_{\left(i+\frac{1}{2}\right)} = \dot{u}^N_{\left(i-\frac{1}{2}\right)} + \frac{\Delta t_{(i+1)} + \Delta t_{(i)}}{2}\ddot{u}^N_{(i)} \tag{4.11}$$

$$u^N_{(i+1)} = u^N_{(i)} + \Delta t_{(i+1)}\dot{u}^N_{\left(i+\frac{1}{2}\right)} \tag{4.12}$$

As mentioned above, the explicit method is conditionally stable, thus the time increment Δt must be small enough to keep a good precision. A maximum value for that time increment called stability limit is set and is an estimation function of the highest frequency of the system ω_{max} as follows:

$$\Delta t \leq \frac{2}{\omega_{max}} \qquad \text{No damping} \tag{4.13}$$

$$\Delta t \leq \frac{2}{\omega_{max}}\left(\sqrt{1 + \xi^2_{max}} - \xi_{max}\right) \qquad \text{With damping} \tag{4.14}$$

where ξ_{max} is the fraction of critical damping in the mode with the highest frequency.

The time increment limit used in Abaqus is an approximation based on the smallest transit time of a dilatational wave across any of the elements in the mesh, expressed as (Dassault Systèmes Simulia Corp., 2020):

$$\Delta t \approx \frac{L_{min}}{c_d} \tag{4.15}$$

where L_{min} is the smallest element dimension, and

c_d the dilatational wave speed:

$$c_d = \sqrt{\frac{\hat{\lambda} + 2\hat{\mu}}{\rho}} \tag{4.16}$$

where ρ is the density of the material, and

$\hat{\lambda}$ and $\hat{\mu}$ are effective Lamé's constants defined as:

$$\hat{\lambda} = \frac{E\upsilon}{(1+\upsilon)(1-2\upsilon)} \tag{4.17}$$

$$\hat{\mu} = \frac{E}{2(1+\upsilon)} \tag{4.18}$$

where E is Young's modulus and υ is Poisson's ratio.

4.4 The Abaqus contact properties

At the interface separating the rock and the backfill material, shear and normal forces are transmitted through a tangential and normal contact behavior.

The tangential or frictional behavior in Abaqus uses a classical isotropic Coulomb friction model (Dassault Systèmes Simulia Corp., 2020). In this model a maximum frictional stress τ_{crit} at the interface between the two surfaces (SPH particles and surrounding rock mass surfaces here) is defined and represents the point where those surfaces start slipping. The maximum shear stress is defined as a fraction of the contact pressure p as follows:

$$\tau_{crit} = \mu p \tag{4.19}$$

where $\mu = \tan\phi'$ is the coefficient of friction used in the simulations. Eq.(4.19) delimits a surface acting as a transition from sticking to slipping for the contact surfaces, as represented in Figure 4-4.

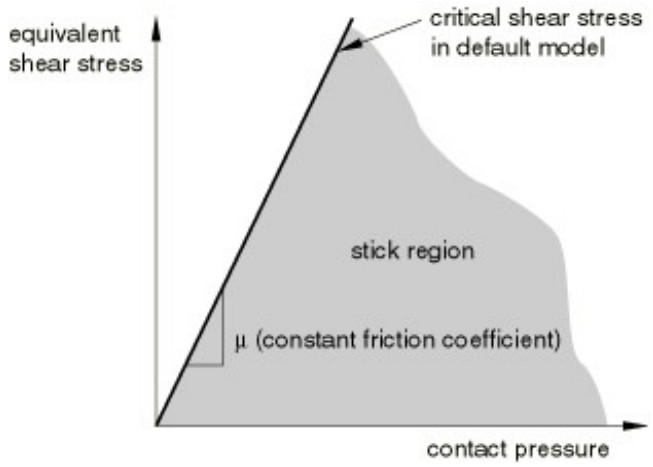

Figure 4-4 Slip regions for Coulomb's friction model (Dassault Systèmes Simulia Corp., 2020).

The coefficient of friction μ is defined as isotropic (same in all directions) giving two orthogonal shear stress components τ_1 and τ_2 in three-dimensions. These two components are combined to give an equivalent shear stress $\tau_{eq} = \sqrt{{\tau_1}^2 + {\tau_2}^2}$ (Dassault Systèmes Simulia Corp., 2020).

The normal contact behavior is defined in Abaqus as a contact pressure-overclosure relationship. The hard contact pressure-overclosure relationship is the most common contact relationship, and it was used in performing all present simulations that were described in section 4.5.1. It represents the most the reality as it does enforce a zero-penetration condition that can be numerically challenging (Dassault Systèmes Simulia Corp., 2020). Figure 4-5 shows the hard contact relationship. When contact pressure is equal to zero, we have a separation of the two surfaces.

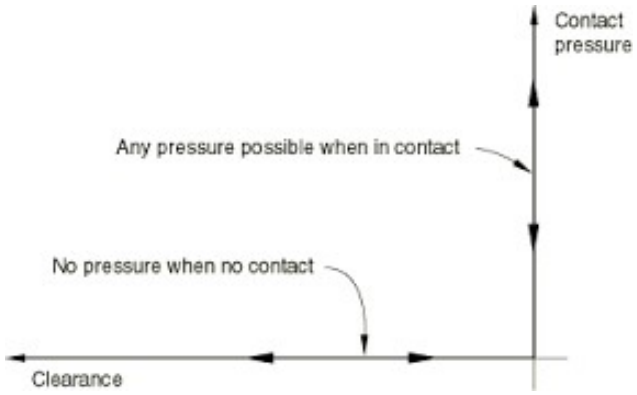

Figure 4-5 Hard contact pressure-overclosure relationship (Dassault Systèmes Simulia Corp., 2020)

4.5 Description of longitudinal and transversal backfilling modes in this study

To study the impact of the backfilling mode on predicted solution-variables, two modes of backfilling were considered in this study. Both backfilling processes represent a uniform continuous progressive backfilling process (UCPBP) starting from the side of one vertical cavity and ending after filling completely the whole excavation:

- The first mode is a continuous backfilling process progressing with a constant backfilling velocity along the longitudinal direction (or along the longest side of the horizontal rectangular section of the trench).
- The second mode is a continuous backfilling process progressing along the transversal direction (or along the shortest side of the horizontal rectangular section of the trench).

Different backfilling velocities were also considered for both backfilling modes in order to study the impact of the backfilling speed on the stress distribution. The backfill material used in the simulations especially performed to achieve this goal was discretized in SPH particles and they were conditioned to fill completely the stope at the end of the backfilling process. The process starts from the cavity side of the first vertical plane and ends at the opposite vertical cavity side of the rectangular trench. The purpose of these two processes is to simulate the dynamic backfilling process and to compare the predicted results to those obtained from a

standard finite element method used in conjunction with a static-general procedure like the one based on an in-situ wished-in-place backfilling finite element analysis. The dimensions of the backfill material

4.5.1 Description and characteristics of the performed simulations

Table 4.1 and the following list summarize the characteristics of all performed simulations in this thesis.

- ✓ Model I, Model II, and Model III simulations use the same stope dimensions, i.e., $\mathrm{B(m)} \times \mathrm{L(m)} \times \mathrm{H(m)} = 15\mathrm{m} \times 30\mathrm{m} \times 45\mathrm{m}$.
- ✓ PS Model's simulations use the same stope dimensions, i.e., $\mathrm{B(m)} \times \mathrm{L(m)} \times \mathrm{H(m)} = 18\mathrm{m} \times 90\mathrm{m} \times 45\mathrm{m}$.
- ✓ In all simulations, the Mohr-Coulomb plastic criterion was used to model the mechanical behavior of the backfill.
- ✓ Model I, Model II, Model III and PS Model (plain strain model) contain distinct performed simulations.
- ✓ Model I, Model II, and Model III simulations were performed using the SPH approach (with an explicit dynamic procedure), the standard finite element method (with a static general procedure FEM); and the SPH approach (also with an explicit dynamic procedure), respectively.
- ✓ PS Model simulations were performed using the SPH approach (with an explicit dynamic procedure) and the standard finite element method (with a static general procedure FEM).
- ✓ Each simulation of Model III and PS Model-long-1m/s's simulation of PS Model was run to completion by imposing a uniform continuous progressive backfilling process (UCPBP).
- ✓ Model I, Model II, PS-SPH Model, and PS-FEM Model were run by imposing an initial wished-in-place (WIP) configuration.
- ✓ The results deduced from the simulations served to determine the influence of UCPBP on contact pressures and distribution of stresses within the backfilled stopes.

Table 4.1 Characteristics of performed simulations

Identification of numerical simulations	Numerical simulation	Technique	Simulation type	Dimensions of the backfill material $B(m) \times L(m) \times H(m)$	Rate of backfilling process[1]	Seed[2]
Model I	Model-I-0.3m-SPH	SPH Explicit	WIP[3]	$15 \times 30 \times 45$	N/A	0.3
	Model-I-0.5m-SPH	SPH Explicit	WIP	$15 \times 30 \times 45$	N/A	0.5
	Model-I-0.8m-SPH	SPH Explicit	WIP	$15 \times 30 \times 45$	N/A	0.8
Model II	Model-II-0.3m-FEM	FEM Standard	WIP	$15 \times 30 \times 45$	N/A	0.3
	Model-II-0.5m-FEM	FEM Standard	WIP	$15 \times 30 \times 45$	N/A	0.5
	Model-II-0.8m-FEM	FEM Standard	WIP	$15 \times 30 \times 45$	N/A	0.8
Model III	Model-III-long-1m/s-(0.5m)	SPH Explicit	UCPBP (longitudinal)	$15 \times 30 \times 45$	1m/s	0.5
	Model-III-long-1m/s-(0.8m)	SPH Explicit	UCPBP (longitudinal)	$15 \times 30 \times 45$	1m/s	0.8
	Model-III-long-1m/s-(0.25m)	SPH Explicit	UCPBP (longitudinal)	$15 \times 30 \times 45$	1m/s	0.25
	Model-III-long-0.75m/s-(0.5m)	SPH Explicit	UCPBP (longitudinal)	$15 \times 30 \times 45$	0.75m/s	0.5
	Model-III-long-0.5m/s-(0.5m)	SPH Explicit	UCPBP (longitudinal)	$15 \times 30 \times 45$	0.5m/s	0.5
	Model-III-trans-1m/s-(0.5m)	SPH Explicit	UCPBP (transversal)	$15 \times 30 \times 45$	1m/s	0.5
	Model-III-trans-0.75m/s-(0.5m)	SPH Explicit	UCPBP (transversal)	$15 \times 30 \times 45$	0.75m/s	0.5
	Model-III-trans-0.5m/s-(0.5m)	SPH Explicit	UCPBP (transversal)	$15 \times 30 \times 45$	0.5m/s	0.5
PS Model	PS-SPH-Model	SPH Explicit	WIP	$18 \times 90 \times 45$	N/A	0.5
	PS-FEM-Model	FEM Standard	WIP	$18 \times 90 \times 45$	N/A	0.5
	PS-Model-long-1m/s	SPH Explicit	UCPBP	$18 \times 90 \times 45$	1m/s	0.5
	Li & Aubertin (2008)	Finite Difference	WIP	18×45 Plane strain simulation	N/A	N/A
interaction	In all simulations and for the rock-backfill interface, it was assumed that $\delta = \phi = 30^{o}$					
Plasticity criterion	Mohr-Coulomb criterion was used in all simulations					

Notes:
[1]Velocity or rate of the backfilling process
[2]Seed: length of the side of the C3D8R element.
C3D8R (Continuum stress/displacement-3Dimensional-8 nodes-Reduced integration): meshing elements.
WIP: whished in place.
[3]Velocities chose for the backfilling process in model III simulations are relatively high because of the the long computation time required for the completion of the simulations.

4.6 Model I: An SPH Abaqus/Explicit wished-in-place backfill mode basic model

4.6.1 The SPH Abaqus/Explicit model I: the basic model

The international unit system was used in this thesis to perform all Abaqus/Explicit and Abaqus/Standard simulations, as shown in Table 4.2.

Table 4.2: Unit System

Variable	length	time	force	stress
Unit	m	s	N	Pa

4.6.1.1 The assembled parts of Model I

The Model I described in Table 4.1 is an assembly of two following different parts:

a. The backfill

The backfill's initial shape is a parallelepiped having a height of $45\ m$, a width of $15\ m$ (i.e., the transversal direction) and depth (i.e., the longitudinal direction) of $30\ m$ corresponding to the initial time $t = 0\ s$ and prior to loading as shown in Figure 4-6.

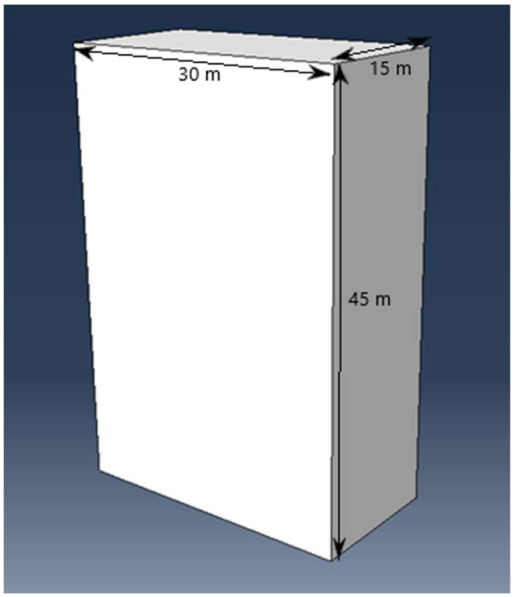

Figure 4-6 Part of the backfill material. Configuration corresponding to Model I at the initial time t=0s and prior to loading.

b. The excavated rock

The entire excavated rock part (Figure 4-7) has a height of $49\ m$, a width of $155\ m$ (i.e., the transversal direction) and depth (i.e., the longitudinal direction) of $170\ m$. These dimensions correspond to the configuration at the initial time $t = 0\ s$ and prior to loading.

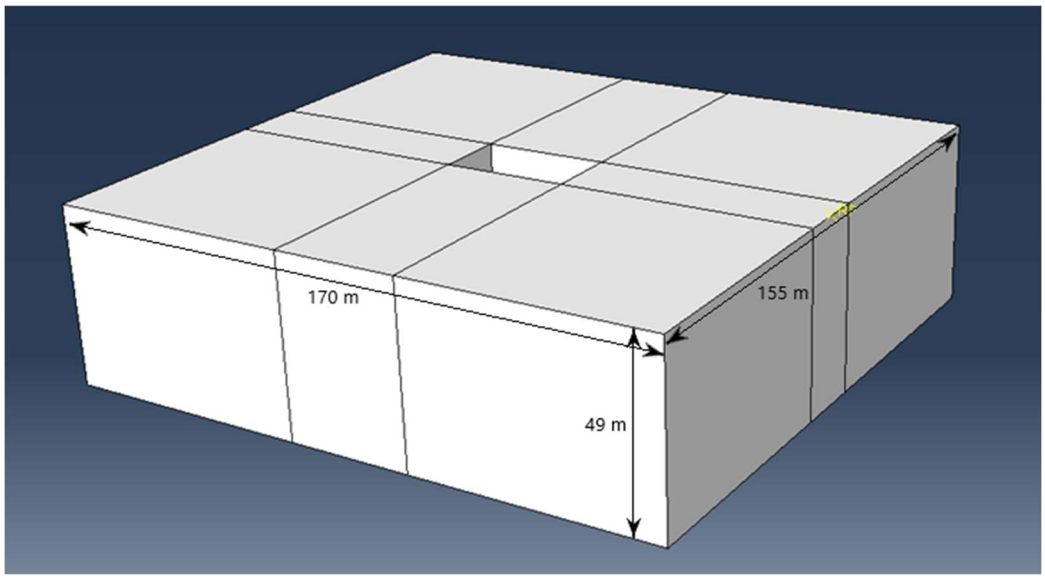

Figure 4-7: 3D representation of the in-situ rock part. Configuration corresponding to model I at initial time $t = 0s$ and prior to loading.

For numerical reasons, the excavated rock was partitioned in two distinct subparts:

i) An elastic-plastic base rock (Figure 4-8) having its internal surfaces forming the cavity in direct contact with the backfill material particles. The 2m-thikness cavity is a 45m-height, 15m-width, and 30m-length.

ii) A rigid bedrock having the following global outer dimensions: a height of $49\ m$, a width of $155\ m$ and a depth of $170\ m$. The bedrock was extruded to obtain a cavity of $47m$-height, $19m$-width, and $34m$-depth (Figure 4-9). The extrusion is necessary to make room for the base rock whose external surfaces are fixed to the extruded cavity in the bedrock.

iii)

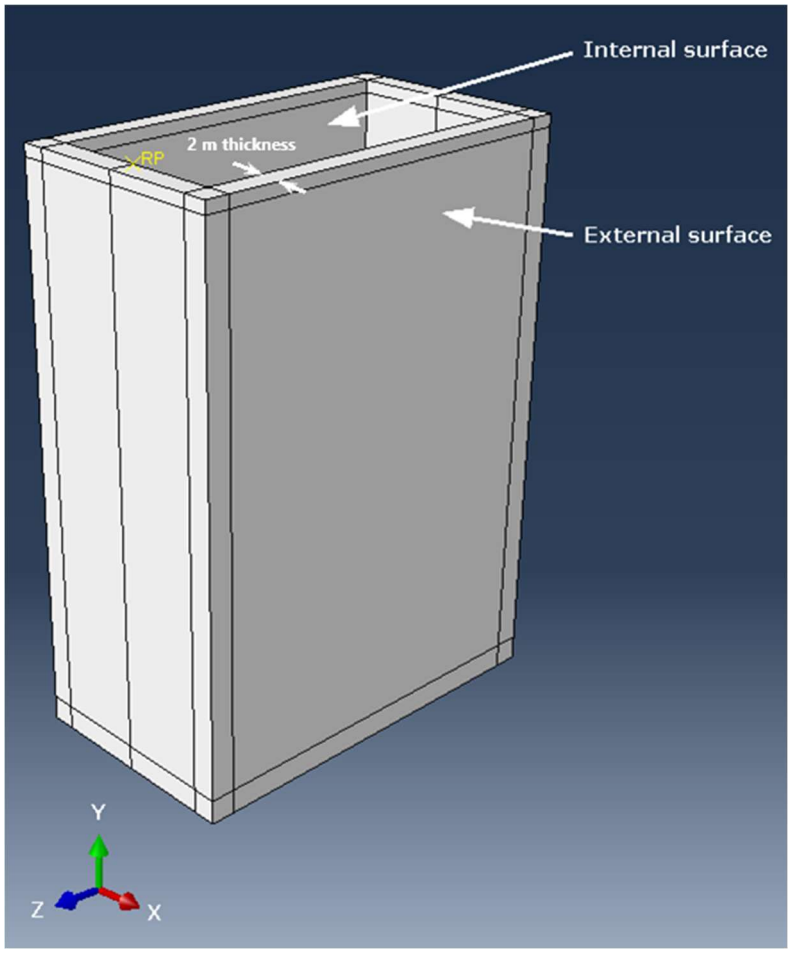

Figure 4-8 : 3D representation of the base rock. Configuration corresponding to Model I at initial time t=0s and prior to loading.

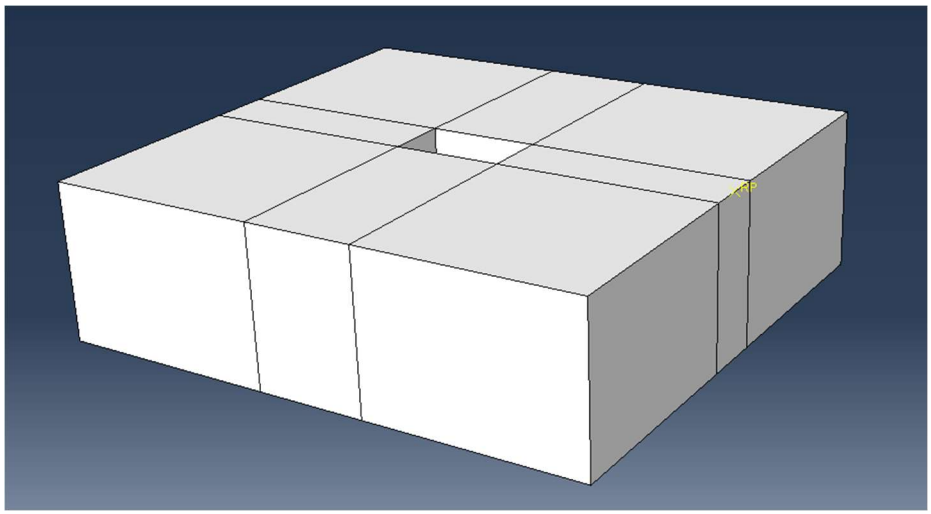

Figure 4-9 : 3D representation of the rigid bedrock. Configuration unchanged with time.

At the initial time, i.e., $t = 0s$, the two parts are assembled to form the initial configuration of Model I, as shown in Figure 4-10. The base rock part of Figure 4-8 is first placed in the trench cavity of the bedrock of Figure 4-9, then the backfill part is preinstalled inside the trench cavity of the base rock shown in Figure 4-8. A 3D representation of the two assembled parts and longitudinal section of the assembled parts which constitute the Model I geometry are shown in Figure 4-10 and Figure 4-11, respectively.

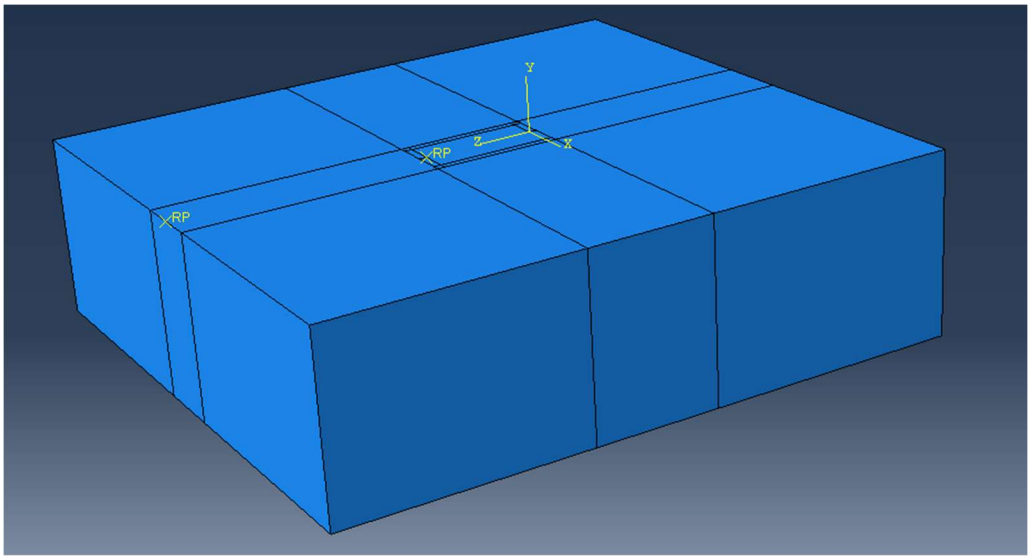

Figure 4-10 : A 3D representation of the two assembled parts. Configuration corresponding to model I at the initial time $\mathrm{t} = 0\mathrm{s}$ and prior to loading.

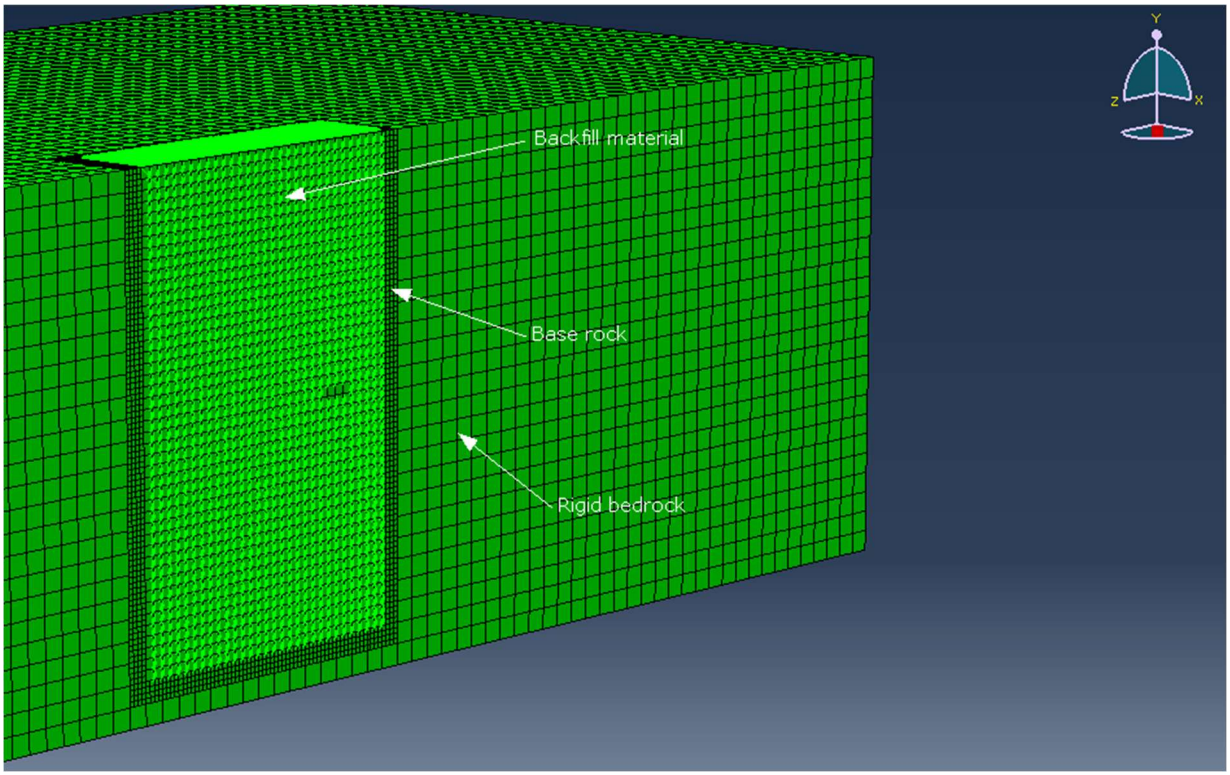

Figure 4-11 : A longitudinal vertical middle section of a 3D representation of the two assembled parts. Configuration corresponding to Model I at the initial time $\mathrm{t} = 0\mathrm{s}$ and prior to loading.

The external surfaces in Figure 4-8 of the base rock are fixed (or embedded) permanently to the internal surfaces shown in Figure 4-9 of the bedrock. At initial time t = 0s, the granular backfill material shown in Figure 4-6 is assumed to be preinstalled in the trench or in the internal cavity of the base rock, and in contact with the internal cavity surfaces (Figure 4-8) which surround and confine the material prior to gravity loading, i.e., at time $t = 0s$.

Figure 4-10 and Figure 4-11 show that the backfill material is preinstalled in the trench at t = 0s; this configuration was named “a wished-in-place backfilling” in the thesis.

4.6.1.2 Mechanical properties of the backfill and the rock

a. **The backfill mechanical model.** The backfill has a density of 1800 kg/m^3 and was assumed to behave as a linear elastic material with a Young’s Modulus equivalent to $3 \times 10^8\ Pa$ and a Poisson’s ratio of 0.2. For a granular material made up of equal uniform spherical particles, the density of 1800 kg/m^3 corresponds to a void ratio of 0.50 or a

porosity of 33%; for a specific gravity of 2700 kg/m^3. In the yielding zone, the material is assumed to obey the Mohr Coulomb plasticity criterion with the following plasticity parameters: i) friction angle $\phi = 30^o$, ii) dilation angle $\psi = 2^o$, iii) cohesion $c = 0\ Pa$.

b. **The excavated rock mechanical model.** The in-place rock is assumed to behave as a linear elastic material with a Young's Modulus equivalent to $3 \times 10^{10}\ Pa$ and a Poisson's ratio of 0.3 and it has a material density of 2700 kg/m^3.

Numerical values of the backfill material and the in-situ rock parameters were taken from the data published by Li and Aubertin (2008).

4.6.1.3 The step of the analysis

In Model I, an explicit dynamic analysis was used in a single step of four seconds of duration. At the beginning of the analysis, i.e., for t = 0s, the backfill material is converted to SPH particles using the elements generated during the meshing process with one particle generated for each parent element. In this step, the automatic incrementation of time was used with conjunction of a global stable increment estimator. No time scaling factor was used throughout automatic time incrementation. Furthermore, this single step accounts for nonlinear geometric effects.

4.6.1.4 Interaction simulation between the different parts of Model I assembly

The general contact formulation which is implemented in Abaqus/Explicit was used to compute contact pressures and tangential stresses at interfaces levels connecting different parts. Regarding the contact property controlling the behavior of the interaction, the normal behavior formulation used is the pressure-overclosure one with hard contact specifications. As for the tangential behavior, the friction coefficient adopted in the computations was equivalent to $\mu = tan\ \delta = 0.578$, with $\delta = 30^o$ being the interface friction angle. The penalty friction formulation in conjunction with the explicit operator was used along this single step of analysis.

For computing efficiency and in the aim of reducing computing runtime, it was decided to rigidify the external part of the in-place or excavated rock (depicted in Figure 4-9) while the inner part of this rock (shown in Figure 4-8) which is in direct contact with the particles remains elastic-plastic. This was intentionally done for permitting computation of the contact pressures between the internal cavity of the in-situ rock and eventually the moving particles.

4.6.1.5 Boundary conditions and applied load. Case of Model I.

The rigid bedrock (which contains the base rock) was embedded and fixed at its reference point (Figure 4-12), and therefore it cannot undergo any displacement or deformation; this imposed condition was maintained in all simulations that were run successfully to completion. The external surface of the base rock, which is in contact with the bedrock's internal cavity, was embedded to the bedrock during all completed simulations. Again, in Model I, the backfill material is directly placed in the "wished-in-place" position within the internal cavity of the in-situ rock or the trench. Bearing in mind that the wished-in-place configuration implies small deformations and after applying gravity load to the whole Model I's assembly, it is expected that the base rock and the generated particles will undergo small deformations during contact. In all explicit dynamic procedures used in Model I's simulations, the internal cavity (or the trench) and the backfill material (or the particles) are free to move and to deform in any direction.

In this particular WIP model, only the gravity load was applied instantaneously to the whole assembly (rigid bedrock, base rock and backfill material). The value of the gravity acceleration was taken equal to $-9.81\ m/s^2$ (Figure 4-12). In Model I, the particles undergo small displacements to reach a quasistatic regime at time t = 4s (i.e., steps duration of all Model I's simulations), in which the particles will be at rest and in an equilibrium position as the kinetic energy becomes almost null, this is due only to the application of gravity load (or the body force). Boundary conditions for the rigid bedrock are enforced through a reference point (RP) defined on its part (Figure 4-10).

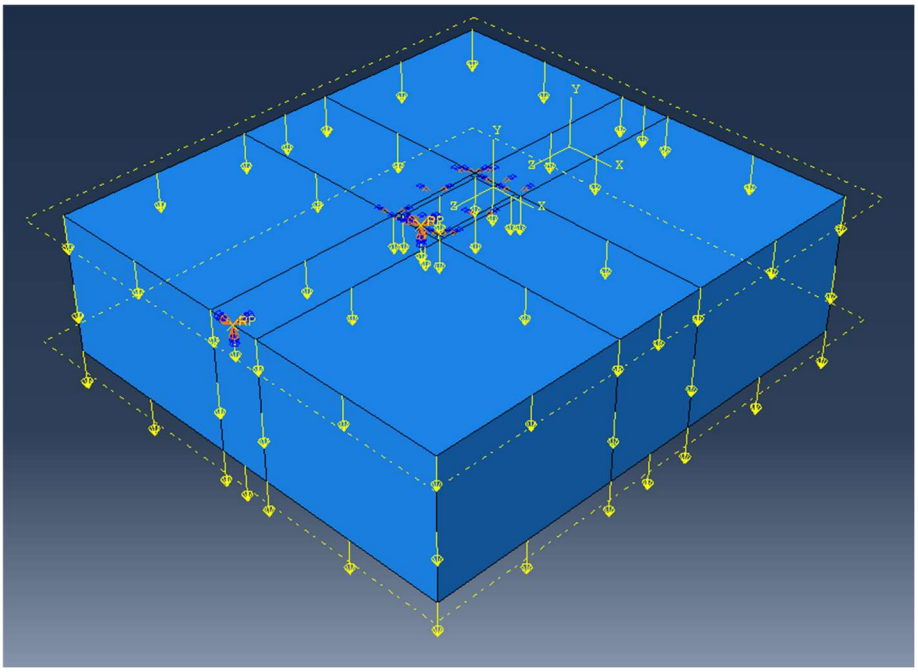

Figure 4-12 A 3D representation showing the gravity applied loads and the fixed bedrock. Configuration corresponding to Model I at the initial time t=0s and prior to loading.

4.6.1.6 Meshing process of backfill and in-situ rock parts

The in-situ rock is partitioned in two subparts as described in section 4.6.1.1. The base rock (which is the subpart directly representing the trench) is embedded and fixed to the rigid bedrock and it is in contact with the granular backfill. As shown in Figure 4-14, the base rock has a seed of 0.5 meters and the bedrock has a seed of 2 meters.

As for the backfill material part, a seed of 0.5m was used to mesh its initial geometry corresponding to t = 0s and prior to gravity loading (Figure 4-15). At the beginning of the analysis, i.e., for time t = 0s, backfill material's structured mesh is converted into SPH (smoothed particle hydrodynamics) particles, and one particle is generated per parent element using a cubic kernel described in subsection 3.4.1. Particles are then free to interact between each other and with the surrounding base rock cavity surfaces, generating then contact pressures. Considering the constructed structured mesh depicted in Figure 4-15, for a seed of 0.5m, the original structured mesh is composed of 162000 C3D8R elements having 172081 nodes for Model I.

All parts of the model were meshed originally using C3D8R elements (Continuum stress/displacement-3Dimensional-8 nodes-Reduced integration). This element is depicted in Figure 4-13.

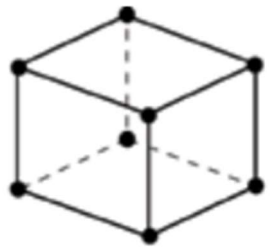

(a) Linear element
(8-node brick, C3D8)

Figure 4-13 Representation of C3D8R element implemented in Abaqus (Dassault Systèmes Simulia Corp., 2020).

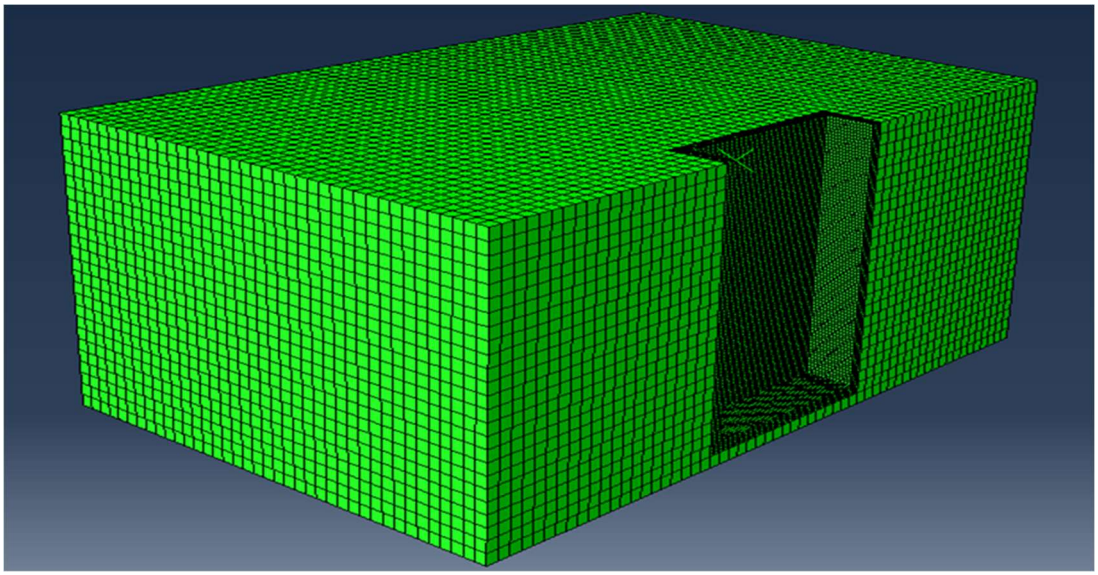

Figure 4-14 A longitudinal vertical middle section of the 3D in-situ meshed rock. Configuration corresponding to Model I at the initial time t=0s and prior to loading.

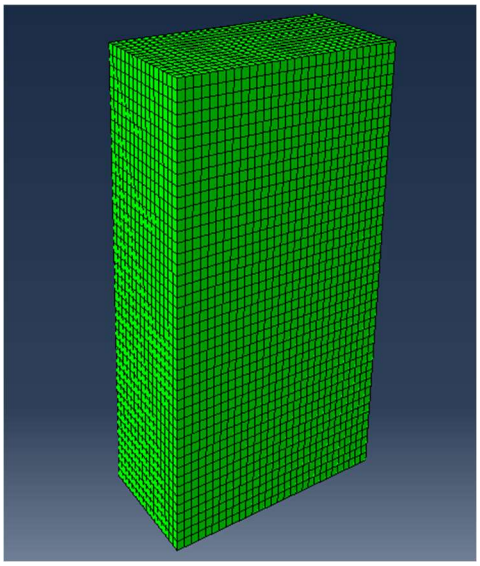

Figure 4-15 Meshing of the backfill material. Configuration corresponding to Model I at the initial time t=0s and prior to loading.

Figure 4-16 and Figure 4-17 shows the position of the assembled meshed rock and backfill before the starting running of Model I's analyses. When these analyses start, the backfill material's C3D8R elements are converted in SPH (Smoothed particle hydrodynamics) particles with one particle per parent element as shown in Figure 4-18, giving a total of 162000 generated particles.

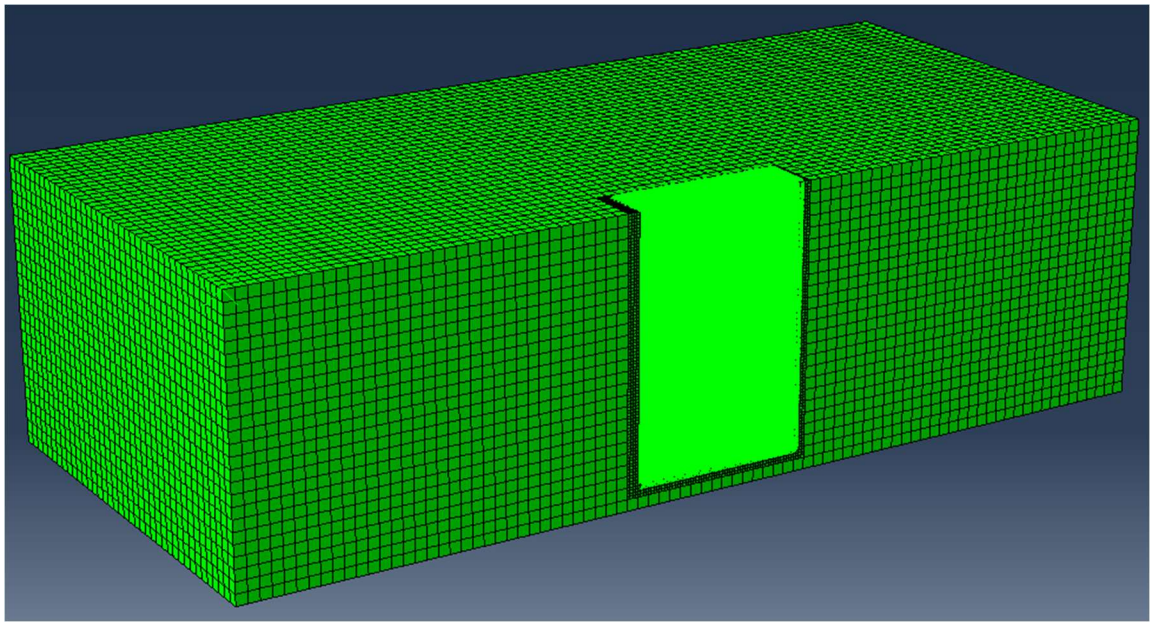

Figure 4-16 Longitudinal vertical middle section of the assembled meshed rock and backfill at initial state (t = 0s) and prior to start running Model I's analyses.

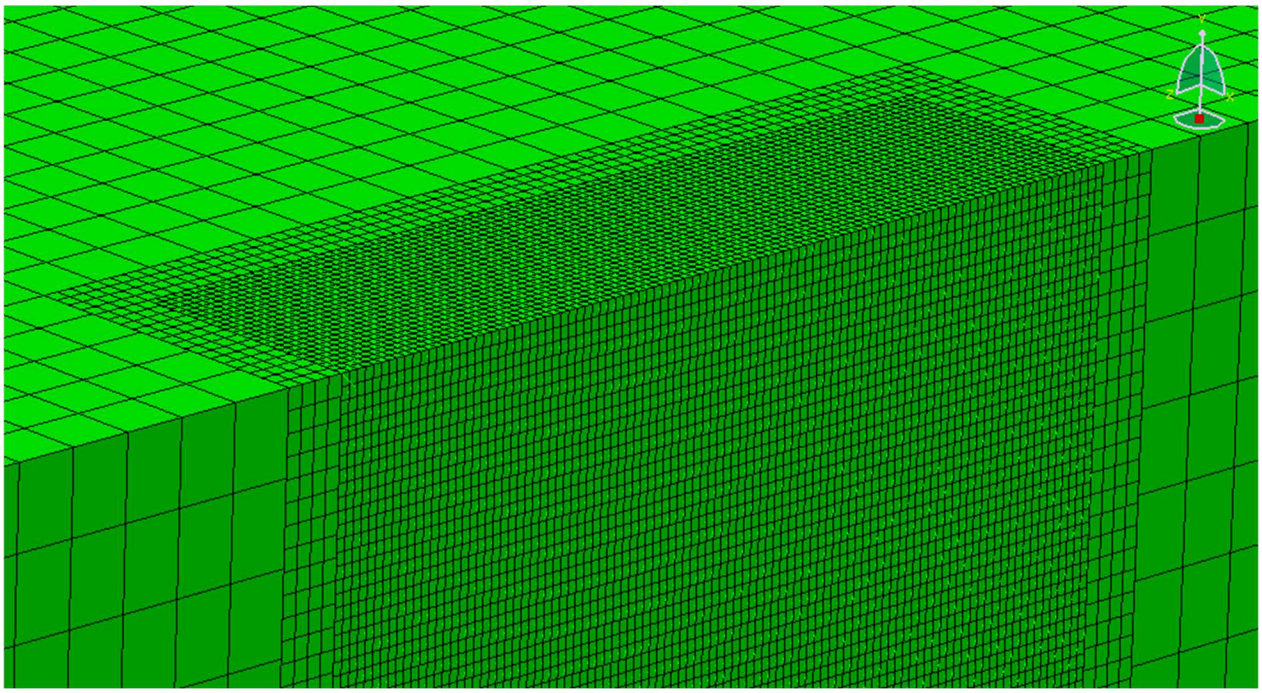

Figure 4-17 Enlargement of the longitudinal vertical middle section of the assembled meshed rock and backfill at initial state (t = 0s) and prior to start running Model I's analyses.

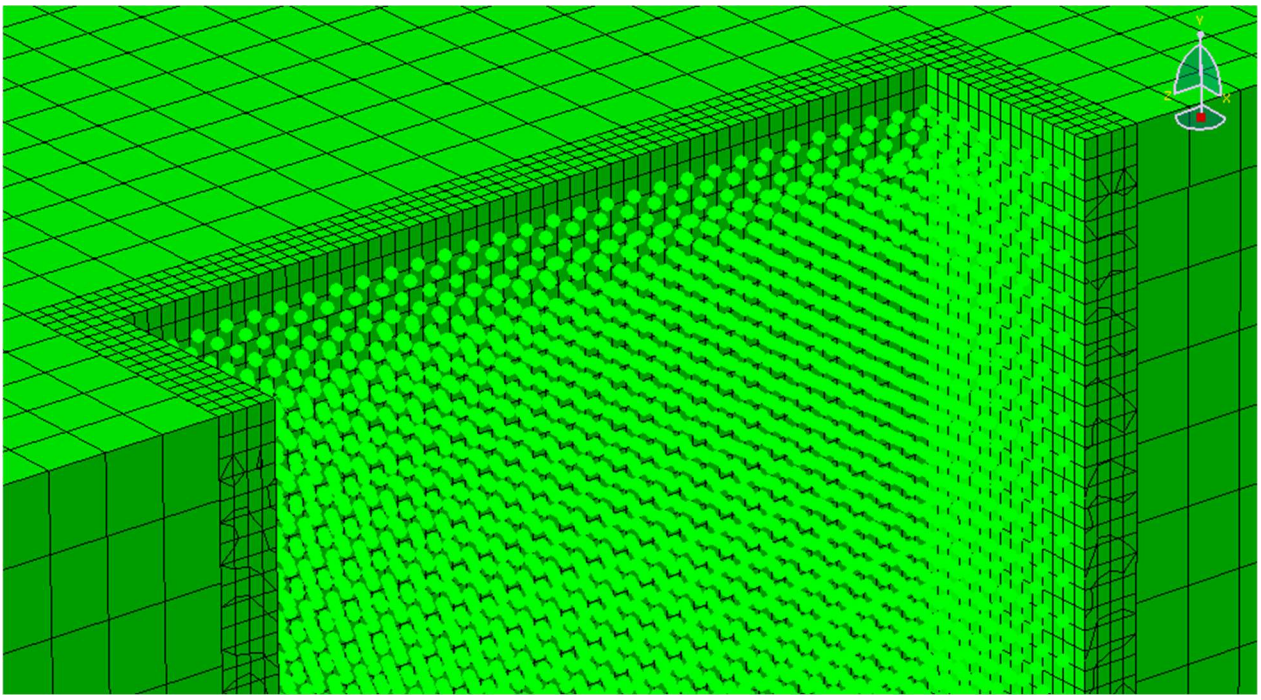

Figure 4-18 Enlargement of the longitudinal vertical middle section of the assembled meshed rock and SPH backfill material at initial state (t = 0s) and prior to start running Model I's analyses.

Simulation Model I-0.5m was chosen among three others listed in Table 4.1 for interpretation of solution-variables deduced from SPH wished-in-place analyses. Path AB is defined by the longitudinal center line and will be named as the longitudinal distance along path (L_d), as defined in Figure 4-19. The corresponding output distribution of contact pressures (CPRESSs) along the path AB are shown later in CPRESS-L_d curves in Figure 4-20.

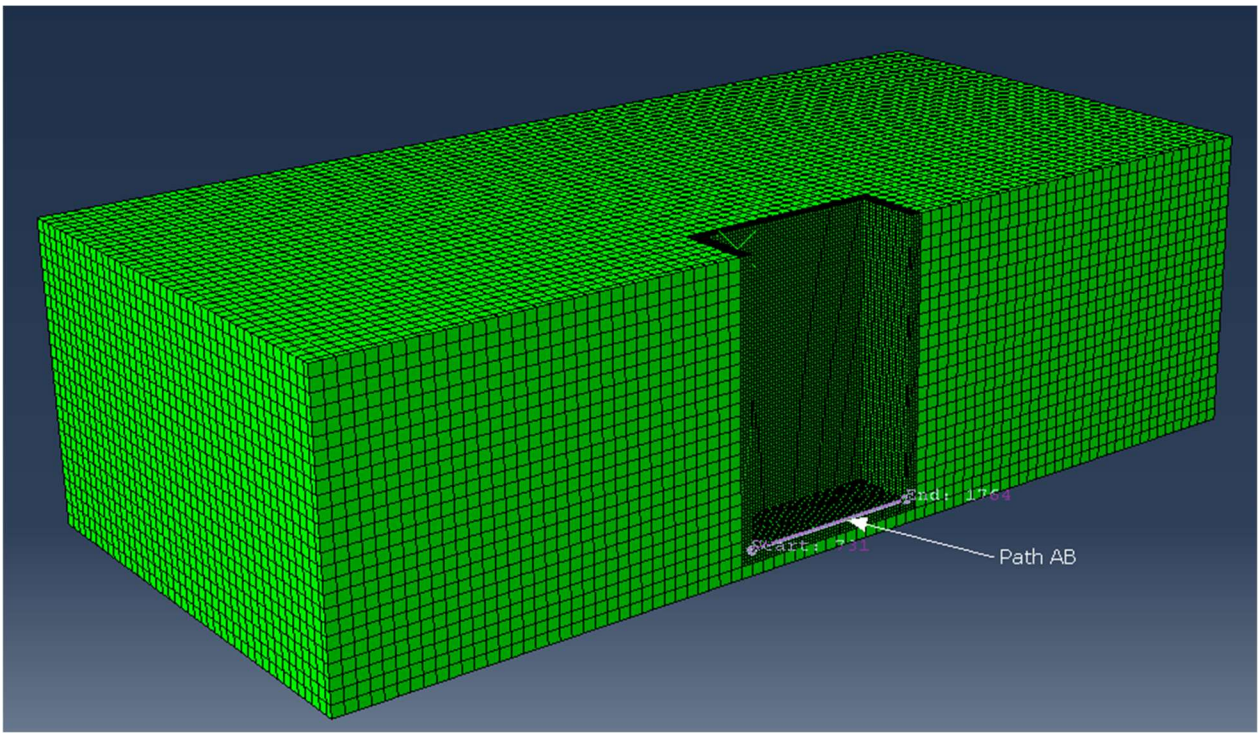

Figure 4-19 Path AB in the longitudinal vertical middle section corresponding to t = 0s. Case of all Models I's simulations.

Figure 4-20 shows that predicted CPRESS-L_d curves are not uniform. This can be interpreted and explained by the fact that in Model I-0.5m, the backfill material medium was discretized (Figure 4-18) with a set of spherical particles, all having a diameter of $0.5m$ and preinstalled in the trench in an initial WIP position. The particles are interacting with each other and are transferring contact pressures up to the base of the stope at 45m of depth. Due to the nature of this surface-particles interaction, CPRESSs will be computed only for nodes belonging to the base rock of the trench (as those composing path AB in Figure 4-19). For the rest of the nodes belonging to the base rock which have no contact with the particles, their computed CPRESSs have null values. This situation is presented by Curve (a) in Figure 4-20 which shows that CPRESS dropped to 0 kPa when L_d

ranges between 19m and 20m, again this is caused by the discontinuous nature of the rock-particles contact. For curve (a), the CPRESS reached a maximum value of 1800 kPa and, as mentioned above, it dropped to 0 kPa. For a better rational interpretation of the computed interaction curves, Curve (b) was determined based on average values of CPRESSs of Curve (a) in Figure 4-20. The average method was used for performing a local polynomial regression around each point in order to create a new smoothed value of each point.

Examination of Curve (b) shows that:

1) Most of points belonging to this curve are located under the curve "overburden stress". The reason of obtaining such a distribution is the initial mesh density, or the seed used for the initial mesh of the backfill (which was 0.5m in the case of Figure 4-20). Curve (b) can approach the overburden Curve (c) while remaining lower than Curve (c). When the seed increases, it is expected that Curve (b) moves upward to approach the overburden curve while staying below it. It is important to mention that increasing the seed will significantly increase the run time. The effect of seed increase used for meshing the backfill's part will be discussed later in this thesis.

2) Curve (b) is not perfectly symmetrical about the vertical plane passing through L_d = 15m because no symmetry was defined with respect to this plane. In the three-dimensional (3D) model, this imperfection can be caused mainly by the small particle's rearrangement after gravity loading, since one particle is internally generated per parent element and has a diameter inferior to the parent element dimensions. Here the particles dimensions were taken approximately at 0.5m.

3) Curve (b) is nearly flat close to the vertical plane passing through L_d = 15m, say for $6m \leq L_d \leq 24m$; in other words CPRESSs corresponding to this range have nearly the same value like it supposed to be in the case of the computed overburden pressure (800 kPa in Figure 4-20) which is independent of L_d because, in this particular case, the 800 kPa value was determined by assuming that the major vertical principal stress due to overburden stress is equivalent to the contact pressure at a determined depth.

4) In the intervals $0m \leq L_d \leq 6m$ and $24m \leq L_d \leq 30m$, both portions of Curve (b) exhibit fluctuations away from the mean value of CPRESSs within the range $6m \leq L_d \leq 24m$

which correspond to the nearly flat curve's portion discussed just before. By approaching each of vertical boundaries of the cavity, the effect of the rock's cavity will be felt and the CPRESSs generated now at the interfaces of both planes are normal to these vertical planes, and therefore CPRESSs values at the bottom of the trench are far from a unidirectional stress state giving an overburden pressure of 800 kPa. Close to L_d = 0m and L_d = 30m, CPRESSs are equivalent to 1125 kPa and 200 kPa respectively.

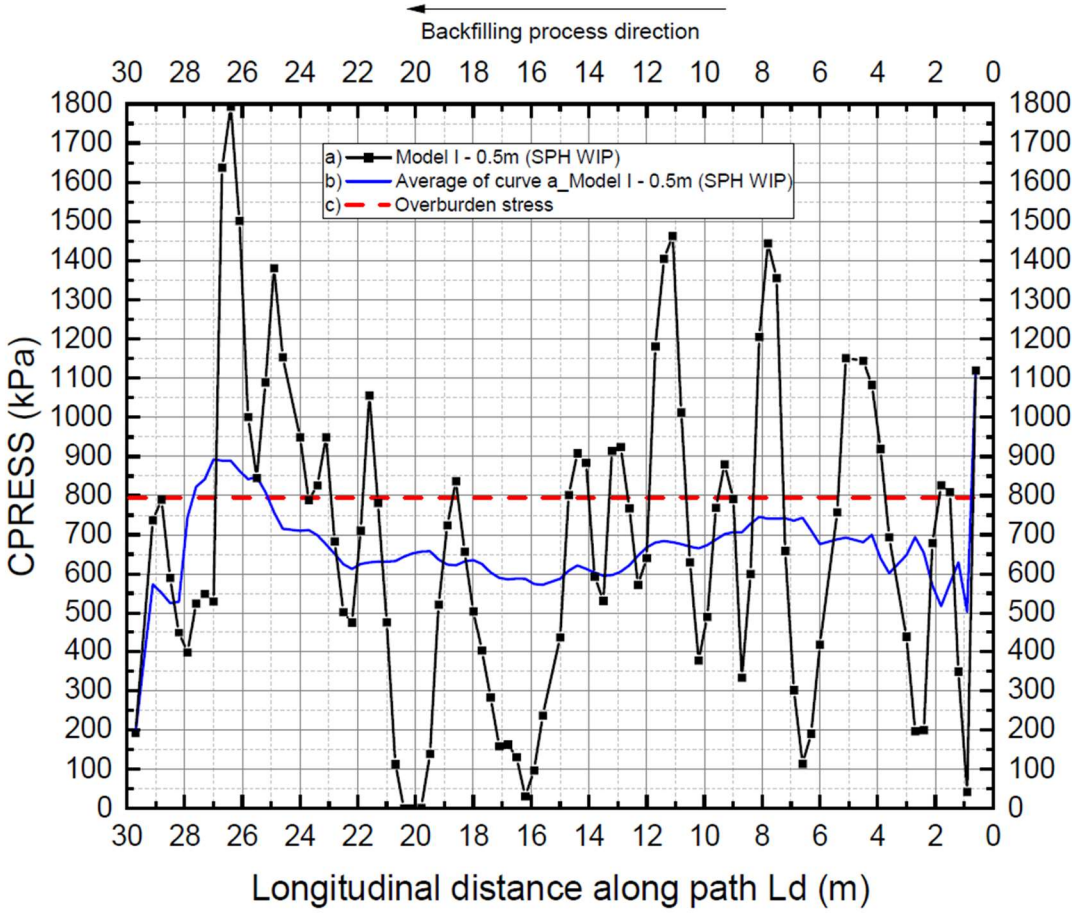

Figure 4-20 CPRESS-Ld curve and its simplified CPRESS-Ld curve. Case of Model I-0.5m (SPH-WIP).

4.7 Model II: An Abaqus/Standard FEM wished-in-place backfill mode model

4.7.1 Model II's simulations characteristics

Model II englobes three distinct simulations describes in Table 4.1. All these simulations use a standard finite element analysis which is implemented in Abaqus/Standard in conjunction with a static general procedure in which all inertia forces are neglected. In the three finite element models of Model II, a wished-in-place assembly of different parts are assumed for initial configurations, i.e., in the initial finite element frame corresponding to initial time t = 0s. Because of the use of a static general procedure in the case of Model II, the backfill material is not converted in SPH particles as mentioned in section 4.6.1.6. The backfill was meshed using a structured mesh technique and C3D8R elements.

In order to determine the effect of the seed on CPRESS's values, Model II-0.3m, Model II-0.5m and Model II-0.8m were all ran to completion using seeds of 0.3m, 0.5m and 0.8m respectively. The rest of modeling conditions such as parts definition, mechanical properties of different parts, contact properties, boundary conditions, and applied gravity load are the same as described in section 4.6.1 for Model I.

4.7.2 Interpretation of computed CPRESS-L_d curves and effect of mesh density in the case of Model-II' simulations

Predicted CPRESS-L_d curves were obtained from Model II's simulations and are depicted in Figure 4-21. A typical CPRESS-L_d curve of Model II-0.3m, Model II-0.5m, and Model II-0.8m, shows that the CPRESS strictly increases from the vertical boundaries of the trench (two vertical planes of the cavity of the trench passing through points L_d = 0m et L_d = 30m) to the symmetrical plane passing through L_d = 15m. It is shown in Figure 4-21 that values of CPRESS approach the overburden stress at the center of the trench (for L_d = 15m), where the effect of the boundary conditions of vertical planes of the trench is minimal. At the center, maximum CPRESS values corresponding to Model II-0.3m, Model II-0.5m, and Model II-0.8m reach approximatively 680 kPa, 760 kPa, and 790 kPa respectively. The latter value is much close to the overburden stress

794.6 kPa (depicted with a green straight line in Figure 4-21) determined in the case of a unidirectional stress state using equation (3.28):

$$\sigma_v = \rho \cdot g \cdot h = 1800 \frac{kg}{m^3} \times 9.81 \frac{N}{kg} \times 45m = 794.6\ kPa \tag{4.20}$$

Contact pressure does not have the same value at a given width ($45m$ in the case of Model II). This phenomenon is due to the arching effect as described by Li and Aubertin (2008), as a stress transfer between the soft backfill material and the stiffer surrounding rock mass due to friction at the interface of the two materials reducing the pressure and stress near the walls.

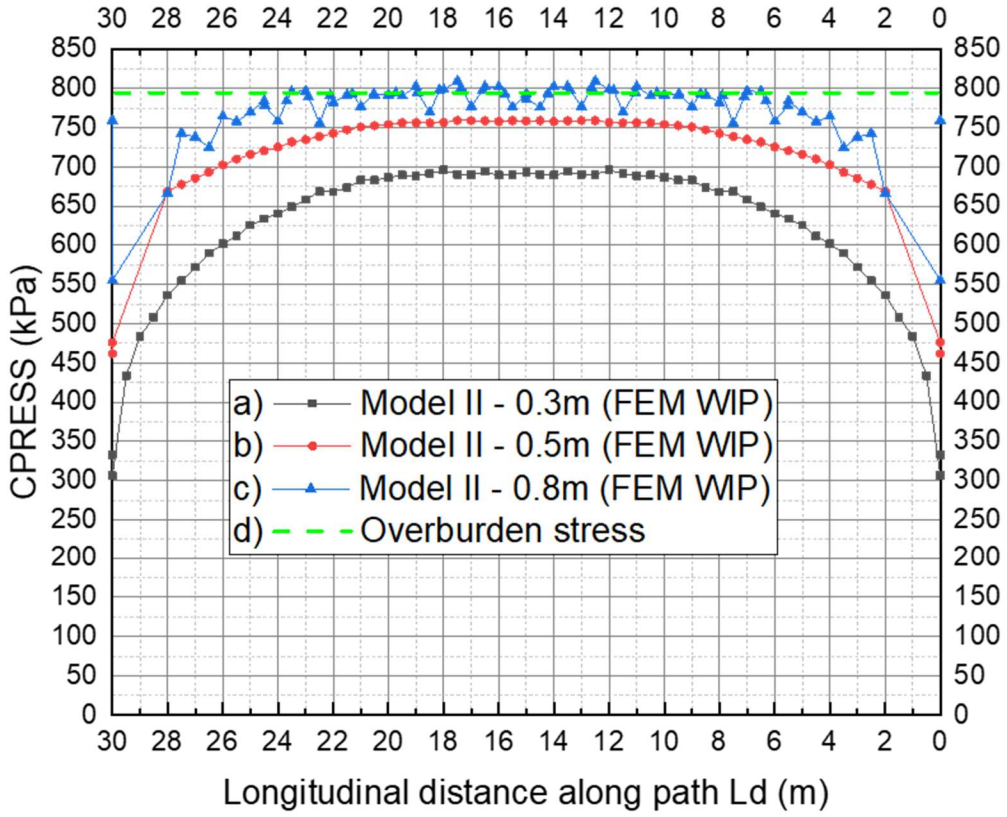

Figure 4-21 Distribution of contact pressures vs longitudinal distance along path (CPRESS-L_d curve): a) Model II - 0.3m, b) Model II - 0.5m, c) Model II - 0.8m and d) Overburden stress.

4.8 Model III: A uniform continuous progressive backfilling process (UCPBP)

All Model III simulations use the SPH (smoothed particles hydrodynamics) method, and the explicit dynamic procedure described in subsection 4.3. Some of their characteristics are the same as those of Model I described earlier in section 4.6.

4.8.1 Model III: Description of the simulations of the UCPBP

4.8.1.1 The assembled parts of Model III

Model III's simulations use the backfill part and the in-situ rock part composing Model I described in subsection 4.6.1.1. A new rigid part depicted in Figure 4-22 and Figure 4-24 was added to all Model III simulations as shown in the whole assembly of Figure 4-23 and Figure 4-25. For convenience, this new part is identified as the "upper rigid box-long" in Model III-long (Figure 4-22) and as the "upper rigid box-trans" in Model III-trans (Figure 4-24). The inner dimensions of the rigid boxes of $2m$-thickness are: $45m$ of height, $15m$ of width (in transversal direction) and $30m$ of depth (in longitudinal direction). The box has a $6.75m \times 15m$ rectangular opening as shown in Figure 4-22 for Model III-long. As for Model III-trans presented in Figure 4-24, the rectangular opening's dimensions are $6.75m \times 30m$. This opening is necessary to permit the granular material inside the upper rigid box to flow inside the trench when the rigid box is uniformly displaced to backfill the trench. The uniform displacement of this box is controlled by its reference point (RP) depicted in Figure 4-22 and Figure 4-24.

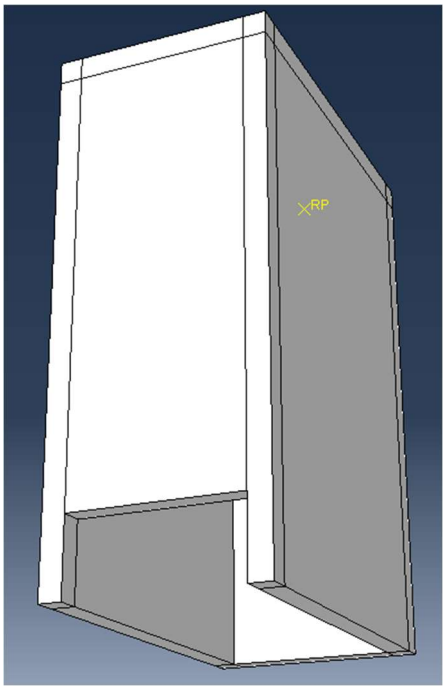

Figure 4-22 The upper rigid box-long part at initial time ($t = 0$). Case of Model III-long-1m/s

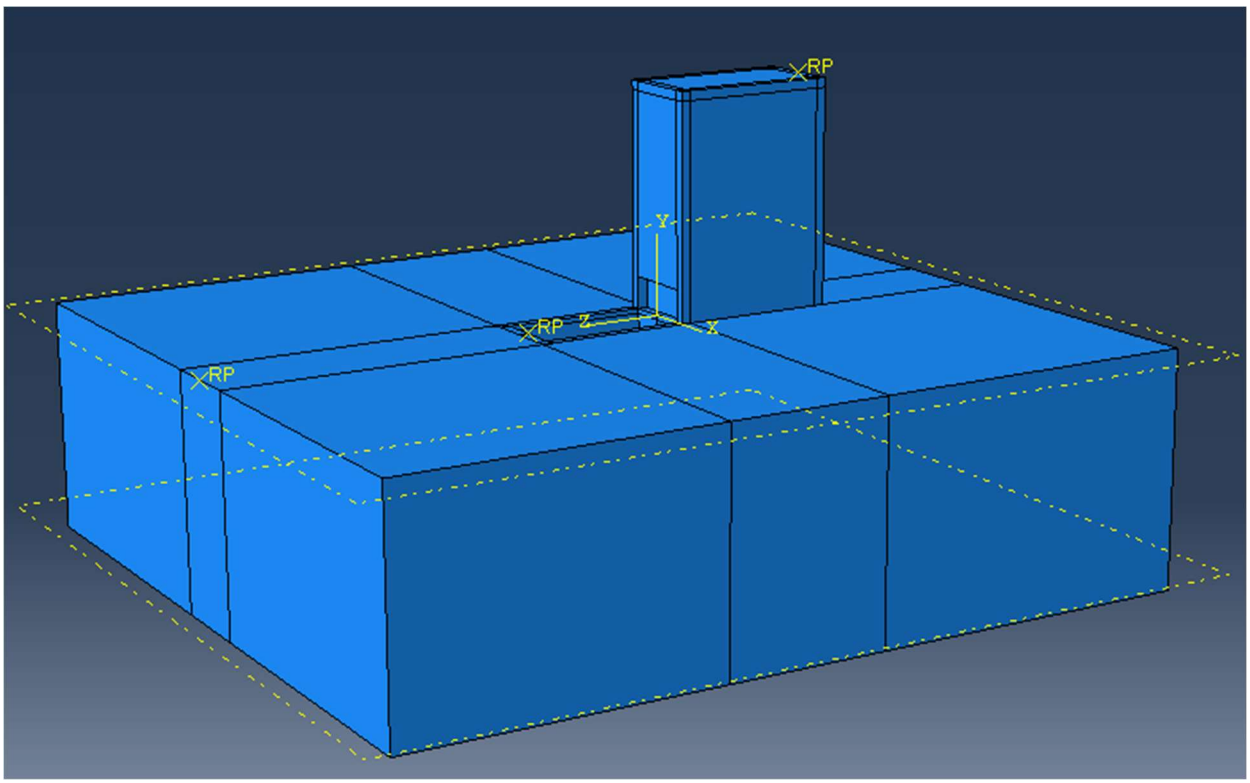

Figure 4-23 Assembled parts. Configuration corresponding to Model III-long-1m/s at the initial time t=0s and prior to gravity loading.

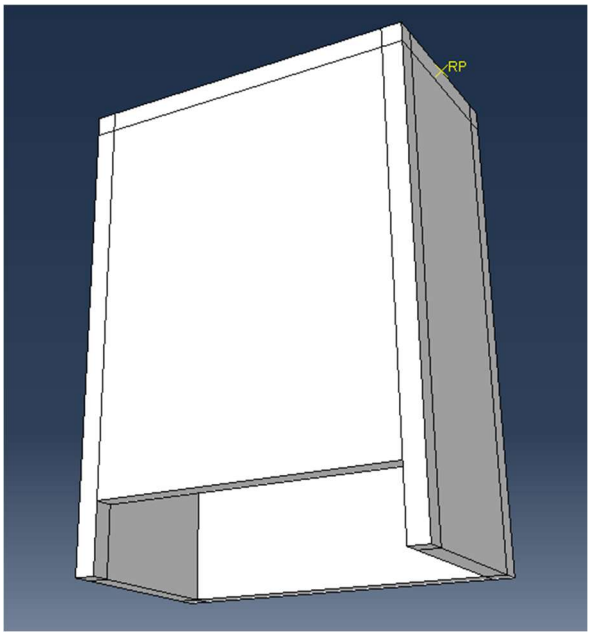

Figure 4-24 The upper rigid box-trans part at initial time ($t = 0$). Case of Model III-trans-1m/s

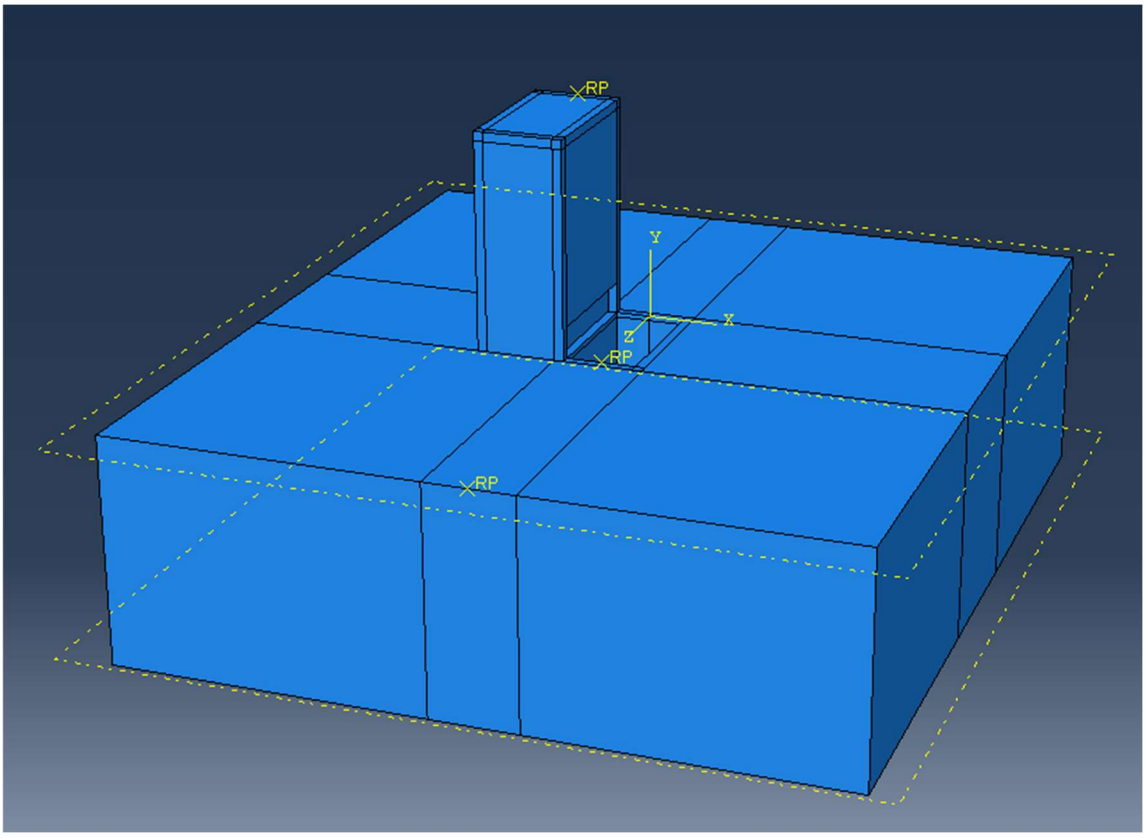

Figure 4-25 Assembled parts. Configuration corresponding to Model III-trans-1m/s at the initial time t=0s and prior to gravity loading.

4.8.1.2 The Model III's assemblies

Mechanical models of the backfill material and the rock used in Model III's SPH analysis were described previously in subsection 4.6.1.2. It is worth remembering that both, the rigid bedrock, and the upper box, were kept rigid in the present simulation except for the inner part of the rock which was assumed as an elastic-plastic material and to be in direct contact with the particles.

All parts are assembled to compose Model III's initial configuration shown in Figure 4-23, corresponding to Model III-long and in Figure 4-25 corresponding to Model III-trans. A longitudinal section of the assembled parts is also shown in Figure 4-26 for Model III-long and in Figure 4-27 for Model III-trans.

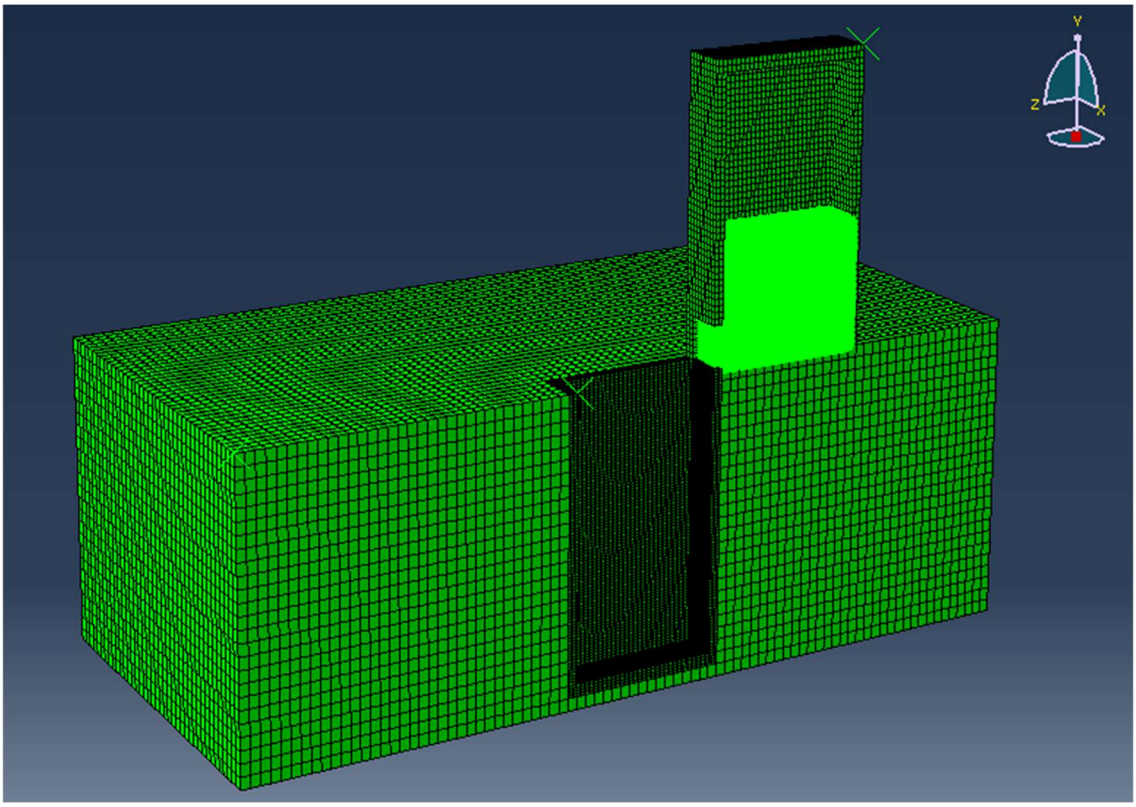

Figure 4-26 Longitudinal vertical middle section of assembled parts. Configuration corresponding to Model III-long-1m/s at the initial time t=0s and prior to gravity loading.

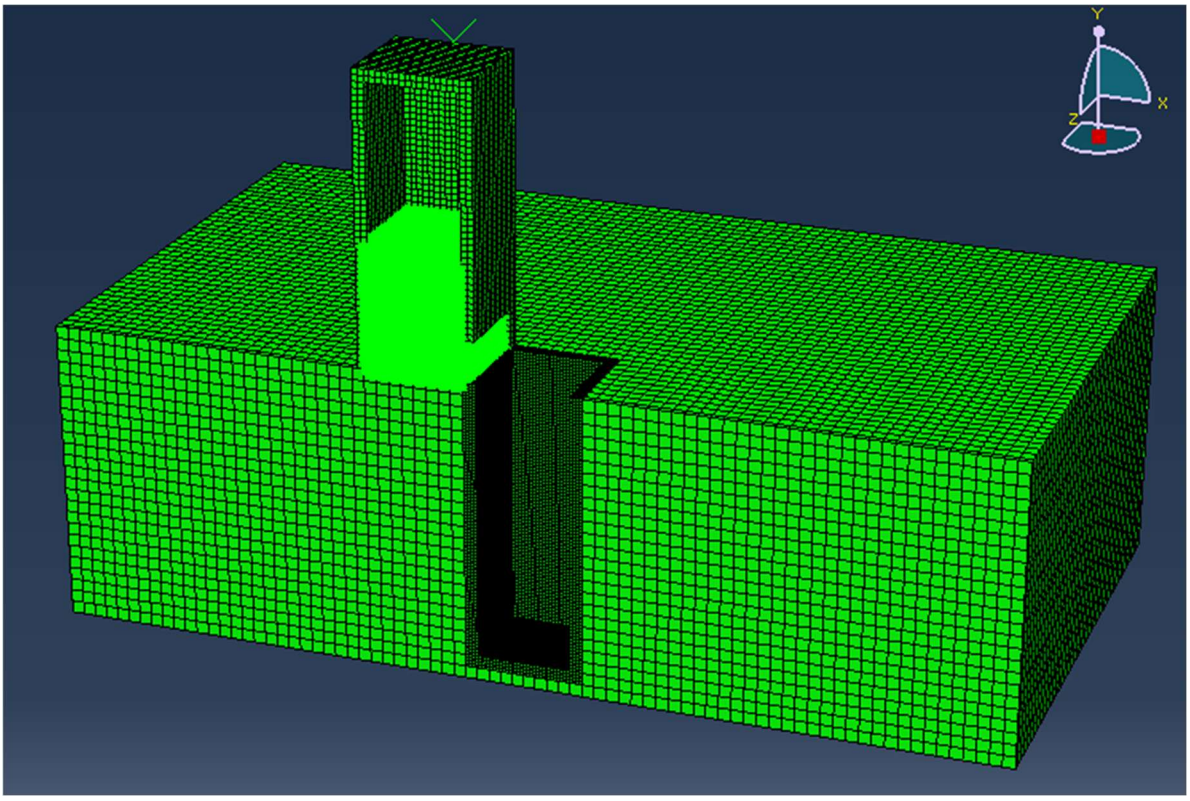

Figure 4-27 Longitudinal vertical middle section of assembled parts. Configuration corresponding to Model III-long-1m/s at the initial time t=0s and prior to gravity loading.

4.8.1.3 Steps of backfilling process of Models III's analyses

In each simulation of Model III, and in the same manner of Model I, an explicit dynamic analysis was again used here with a single step time. The duration of this step is different in all Model III' simulations because the upper rigid box defined in subsection 4.8.1.1 was assumed to move with different velocities. The different step times corresponding to the performed analyses are presented in Table 4.3.

In all models' analysis step, the automatic incrementation was used with conjunction of a global stable increment estimator. No time scaling factor was used throughout automatic time incrementation. Furthermore, this single step again accounts for nonlinear geometric effects.

Table 4.3 Characteristics of Model III's analyses: Displacements, rates of backfilling and step times

Numerical simulation	Upper box displacement (m)	Rate of backfilling process (m/s)	Analysis step time (s)
Model III-long-1m/s	70	1	70
Model III-long-0.75m/s	70	0.75	88
Model III-long-0.5m/s	70	0.5	140
Model III-trans-1m/s	40	1	40
Model III-trans-0.75m/s	40	0.75	54
Model III-trans-0.5m/s	40	0.5	80

4.8.1.4 Interaction between different parts of Model III's assemblies

As for Model I, the general contact formulation implemented in Abaqus/Explicit was used here in all Model III simulations in conjunction with a normal hard contact behavior formulation based on the pressure-overclosure contact, allowing separation when overclosure is positive. As for tangential behavior, the friction coefficient as μ was specified as $\mu = tan\,\delta = 0.578$, with $\delta = 30^o$. The penalty friction formulation in conjunction with the explicit operator were used along all steps of analyses of Model III-long-1m/s, Model III-long-0.75m/s, Model III-long-0.5m/s, Model III-trans-1m/s, Model III- trans -0.75m/s, and Model III- trans -0.5m/s. The external part of the in-situ rock was also rigidified while the inner part which is in contact with backfilling particles remains elasto-plastic as explained in section 4.6.1.4. The upper rigid box was also rigidified, so it cannot be deformed but it can undergo uniform displacement in the longitudinal or transversal directions. Moreover, contact between the in-situ rock and the upper box was not allowed; this was done in order to reduce computational CPU runtime.

4.8.1.5 Boundary conditions and applied loads.

In all simulations of Model III, the rigid bedrock was fixed and embedded at its reference point (RP) and all its displacements and rotations were restrained, as shown in Figure 4-29 and in Figure 4-31.

The backfill material is placed in upper rigid box-long for the longitudinal backfilling process analyses and in the upper rigid box-trans for the transversal backfilling process at initial time i.e., before gravity loading and before imposing velocities. The gravity load is applied instantaneously to the whole assembly (i.e., rigid bedrock, base rock, backfill material and upper rigid box). The value of the gravity acceleration was taken equal to $-9.81\ m/s^2$ (Figure 4-28 and Figure 4-30); the negative sign indicates that its direction is downward, i.e., in the opposite direction of y axis, which is oriented positively upward as shown in Figure 4-28 and Figure 4-30.

In the backfilling steps (longitudinal : long, and transversal: trans), two types of uniform velocities were imposed at reference points of rigid box-long and upper rigid box-trans : a) V-long = 1 m/s, 0.75m/s, 0.5m/s in the direction of z axis, as shown in Figure 4-28, and b) V-trans = 1 m/s, 0.75m/s, 0.5m/s in the direction of x axis, as shown in Figure 4-30. These boundary conditions are also described in Table 4.1.

A parametric study was performed in aim to determine the effect of the velocity of the backfilling process on predicted solution-variables such as the CPRESS beneath the deposited granular material at the end of the backfilling process. Therefore, the upper box-long undergoes displacements when submitted to several uniform velocities in the longitudinal (z) direction i.e., 1m/s, 075m/s, and 0.5 m/s which correspond to the analyses of Model III-long-1m/s, Model III-long-0.75m/s, Model III-long-0.5m/s.

In the same manner, the upper box-trans undergoes displacements when submitted to several uniform velocities in the transversal (x) direction i.e., 1m/s, 075m/s, and 0.5 m/s which correspond to the analyses of Model III-trans-1m/s, Model III-trans-0.75m/s, Model III-trans-0.5m/s.

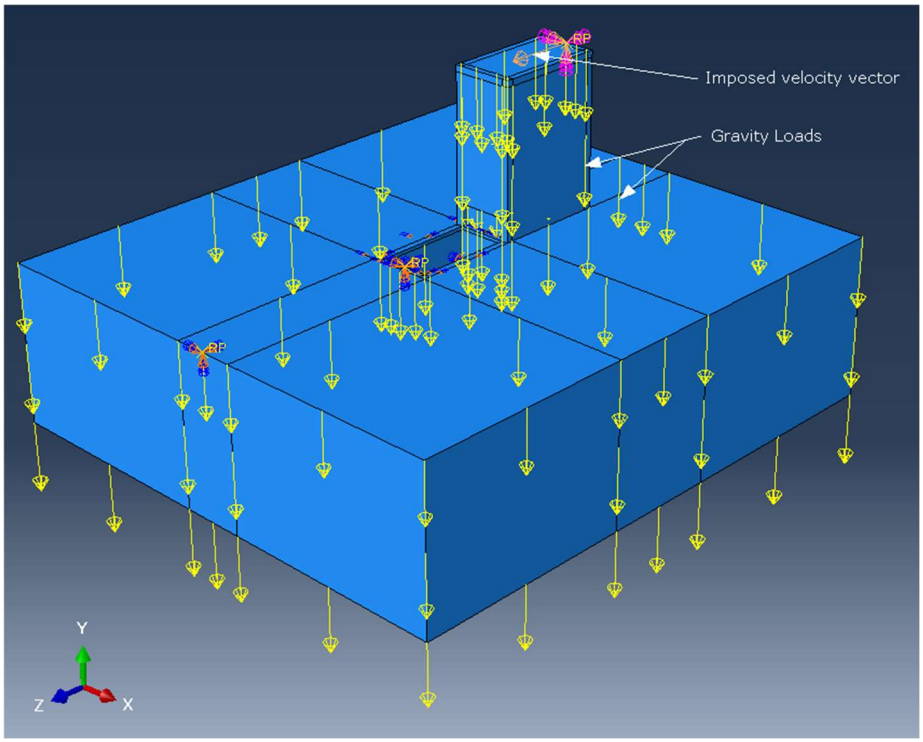

Figure 4-28 A 3D representation showing the gravity applied loads, imposed velocity vector of backfilling, and the fixed bedrock. Configuration corresponding to Model III-long-1m/s at initial time t = 0s.

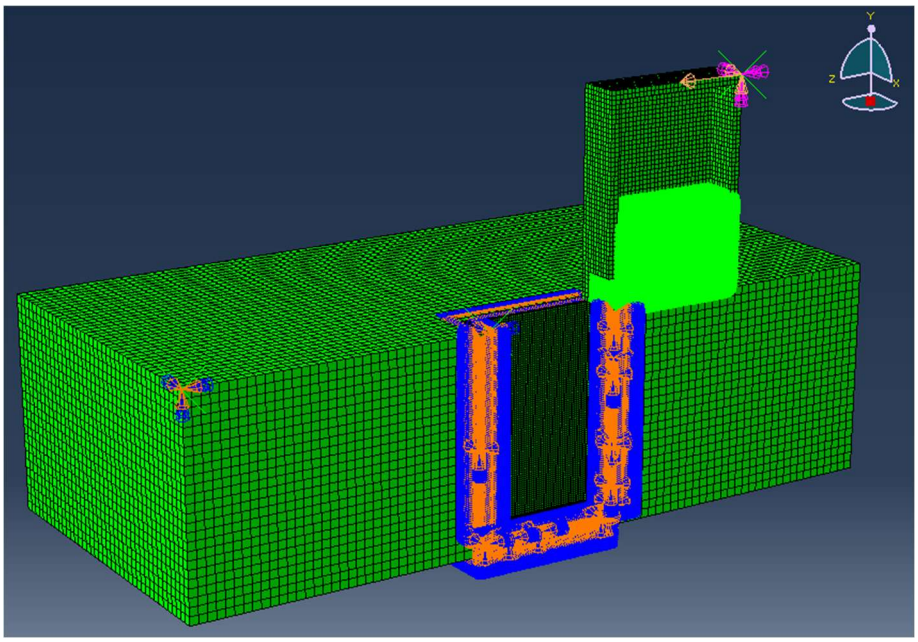

Figure 4-29 Longitudinal vertical middle section showing SPH particles, imposed velocity vector of backfilling, and the fixed bedrock. Configuration corresponding to Model III-long-1m/s at initial time t = 0s.

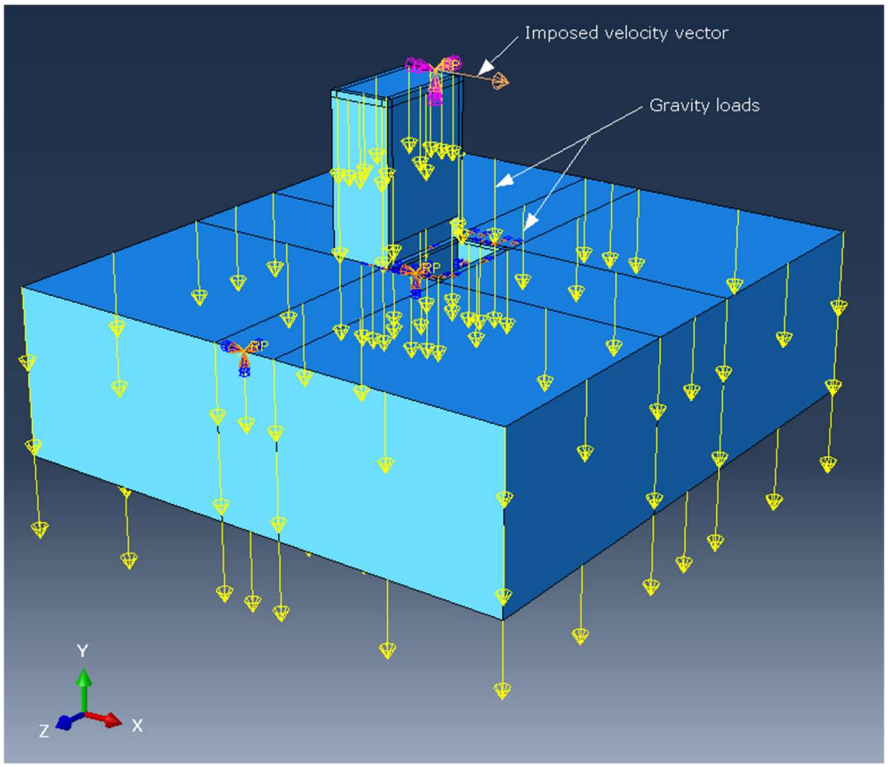

Figure 4-30 A 3D representation showing the gravity applied loads, imposed velocity vector of backfilling, and the fixed bedrock. Configuration corresponding to Model III-trans-1m/s at initial time t = 0s.

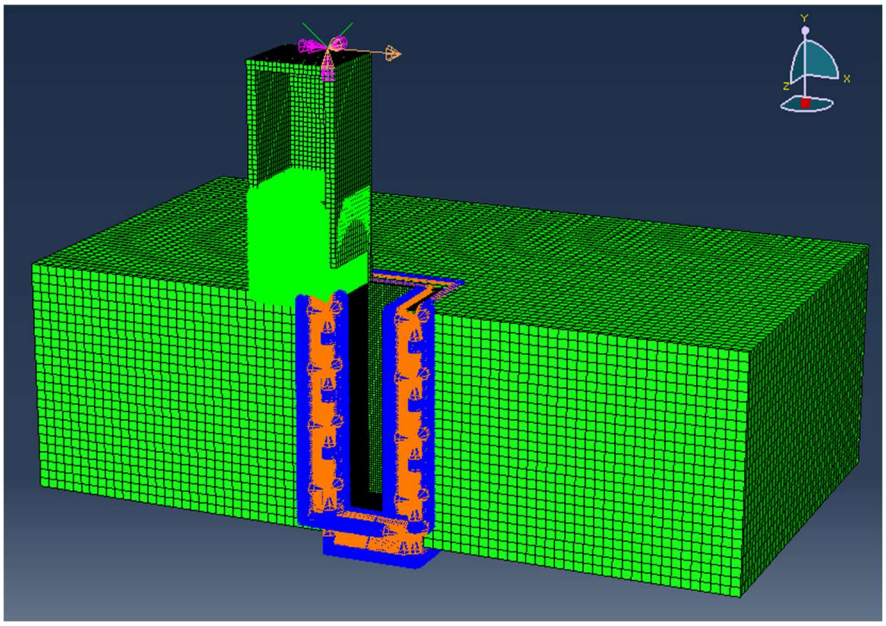

Figure 4-31 Transversal vertical middle section showing SPH particles, imposed velocity vector of backfilling, and the fixed bedrock. Configuration corresponding to Model III-trans-1m/s at initial time t = 0s.

4.8.1.6 Mesh construction of backfill and of in-situ rock parts

All Model III simulations are meshed with C3D8R elements (Continuum stress/displacement-3Dimensional-8 nodes-Reduced integration) available in Abaqus/Explicit. The dimensions of the elements are the same as those used earlier in the two previous models. As for the new part, i.e., the upper rigid box, it has been meshed with a seed of $1\ m$. For the backfill, seeds of $0.2m$, $0.5m$ and $0.8m$ were used in 3 different simulations for the longitudinal (z) direction backfilling process, as presented in Table 4.1. For the transversal (x) direction backfilling process, only a seed of $0.5m$ has been used. One particle per parent element is also generated at the beginning of all Model III simulations as the backfill material is converted into SPH particles.

These models represent an in-situ backfilling process where the stope is progressively filled from one side to the other. As shown in Figure 4-26, the backfill material is placed in the upper box with an opening to let particles go through continuously until the stope is completely filled.

4.8.1.7 Description of the UCPBP process

The UCPBP process starts from the configuration shown in Figure 4-32 (for Model III-long) or Figure 4-35 (for Modell III-trans) and ends at the configuration shown in Figure 4-34 (for Model III-long) or Figure 4-37 (for Modell III-trans). Figure 4-33 and Figure 4-36 represent the intermediate configuration at half time for Model III-long and Modell III-trans, respectively. At the beginning of the analysis, the backfill material is converted into SPH particles, with one particle generated per parent element and the upper box moves from one side of the trench to the other, freeing the particles that were contained. Particles are then free to interact with each other, with the surrounding upper rigid box, and later with the base rock walls as they fill the trench, generating contact pressures. This situation is shown in Figure 4-34 and Figure 4-37 for the case of Model III-long-1m/s and Model III-trans-1m/s, respectively.

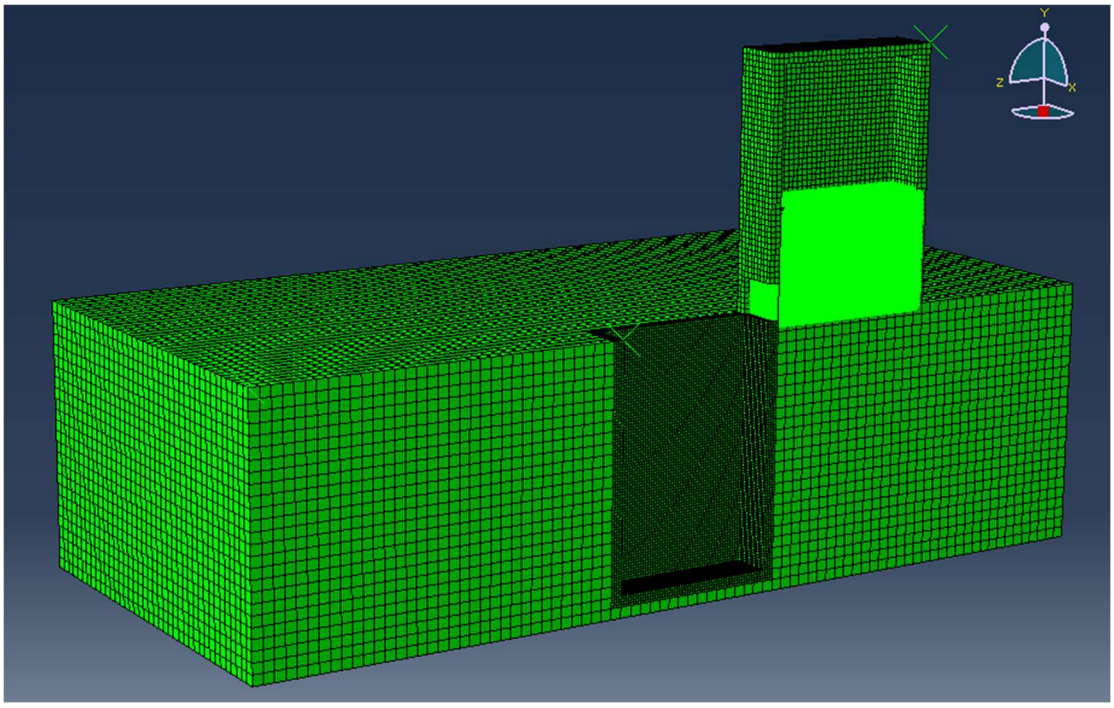

Figure 4-32 Longitudinal vertical middle section in the case of a UCPBP. Configuration corresponding to Model III-long-1m/s at initial time t = 0s.

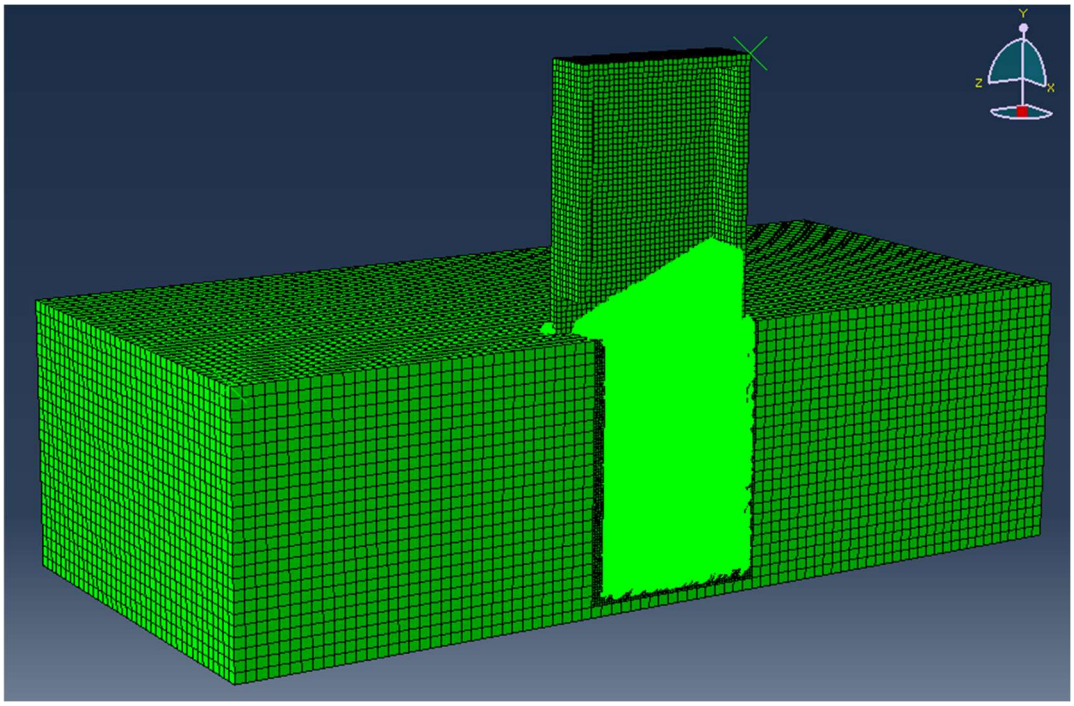

Figure 4-33 Longitudinal vertical middle section in the case of a UCPBP. Configuration corresponding to Model III-long-1m/s during the backfilling process at t = 35s.

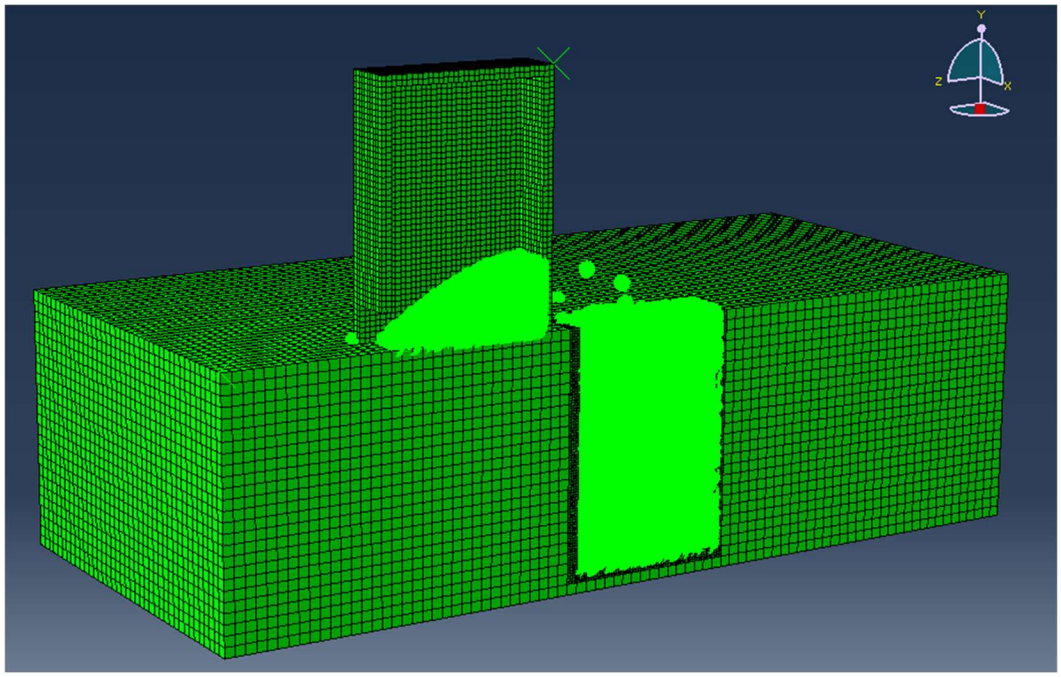

Figure 4-34 Longitudinal vertical middle section in the case of a UCPBP. Configuration corresponding to Model III-long-1m/s at the end of the backfilling process at t = 70s.

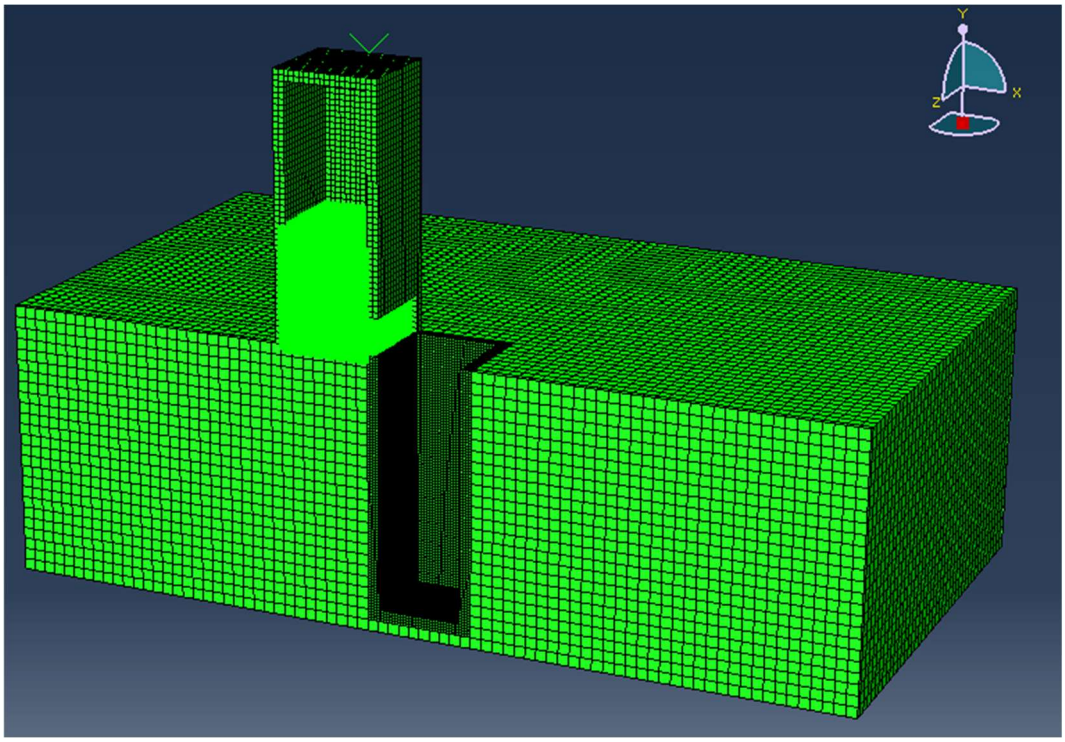

Figure 4-35 Transversal vertical middle section in the case of a UCPBP. Configuration corresponding to Model III-trans-1m/s at initial time t = 0s.

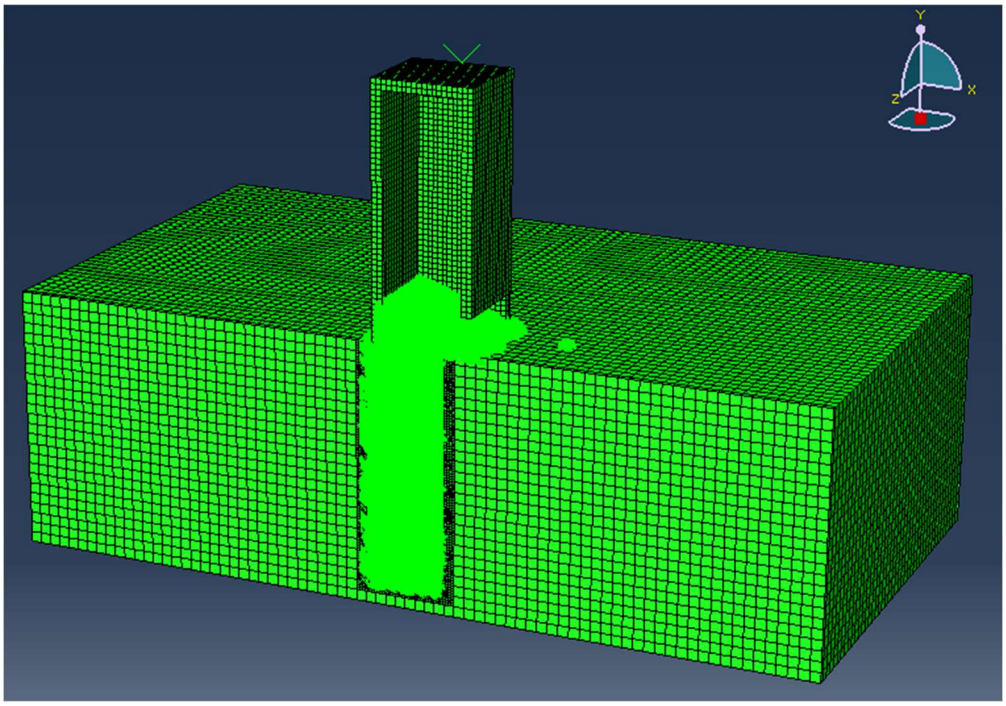

Figure 4-36 Transversal vertical middle section in the case of a UCPBP. Configuration corresponding to Model III-trans-1m/s during the backfilling process at t = 20s.

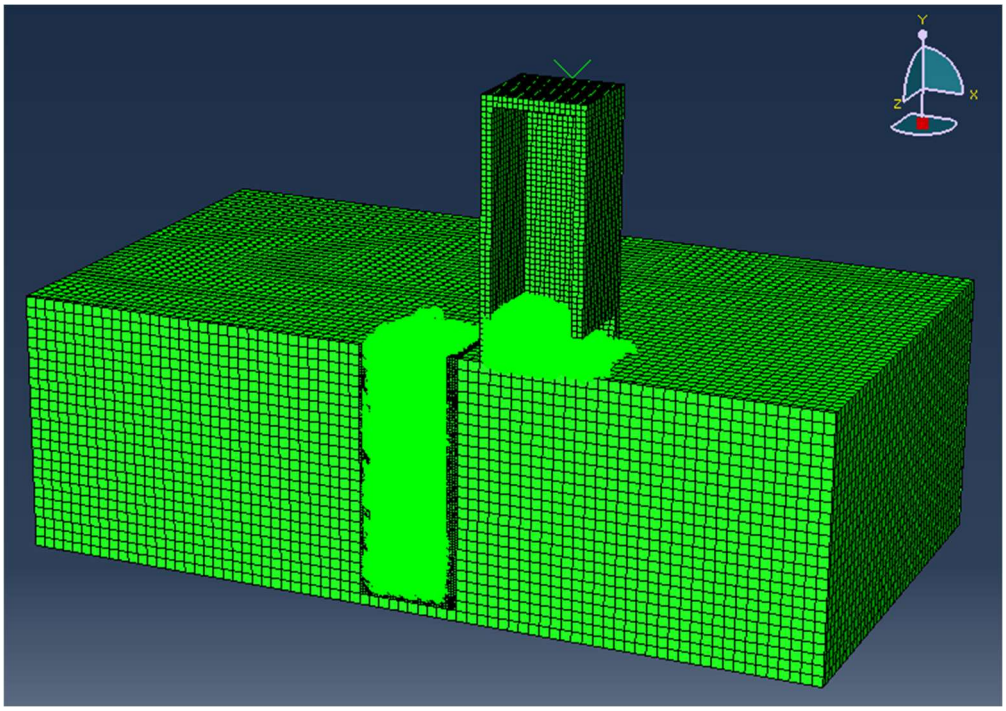

Figure 4-37 Transversal vertical middle section in the case of a UCPBP. Configuration corresponding to Model III-trans-1m/s at the end of the backfilling process at t = 40s.

4.8.2 Interpretation of the predicted variables deduced from Model-III simulations

Each of the analyses of Model III (Table 4.1) simulates a uniform continuous progressive backfilling process (UCPBP). Model III-long-1m/s (0.5m) is chosen for the interpretation of the predicted results in the present subsection.

The line AB already shown in Figure 4-19 is a path determined from the intersection of the longitudinal vertical middle section and the horizontal plan of the bottom of the trench at t = 0s, and prior to any deformation. The length of this path (L_d), and for t= 0s is the same as the interior length of the bottom of the trench, i.e., $L_d = 30m$.

Results deduced from the Model III-long-1m/s simulation show the distributions of contact pressures (CPRESSs) along path AB which is located beneath particles (Figure 4-38).

As for the Model I, the curves depicted in Figure 4-38 show a non-uniform distribution of the CPRESSs beneath particles. It is important to notice that for Curve b the null-contact pressure values at some points situated on the L_d axis are caused by the lack of soil-rock contact for two successive particles, as shown in the frame corresponding to $t = 70s$ in Figure 3.39. Examples of these points correspond to zero CPRESSs and to distances of $L_d = 5m, 7.5m, 10m, and\ 26m$ as shown in Figure 4-38.

The simplified CPRESS-L_d curve c permits to conclude that the predicted CPRESS values, at the end of the backfilling process and at the vicinity of the wall interface at $L_d = 0m$, are higher than those predicted at the wall interface at $L_d = 30m$. It can be added that along this process, the CPRESS values slightly decrease with increasing backfilling distance (L_d).

Examination of the simplified curve c deduced from the solution of Model III-long-1m/s (0.5m) permits to draw the following conclusions:

i) at the beginning of the backfilling process i.e., for $L_d = 0m$, CPRESS $= 470.8\ kPa$;

ii) then CPRESS decreases drastically from $470.8\ kPa$ at $L_d = 0m$ to $279.2\ kPa$ at $L_d = 0.5m$;

iii) during the UCPBP backfilling process, CPREES values decrease from $279.2\ kPa$ at $L_d = 0.5m$ to $84.9\ kPa$ at $L_d = 29m$ and;

iv) at the end of the backfilling process, i.e., for $L_d = 30m$, CPRESS $= 227.6\ kPa$.

Con-III-1: CPRESS decrease along the path oriented in the direction of the backfilling process direction.

CPRESS-L_d curve b in Figure 4-38 is obtained by using the exact values of contact pressures. This curve shows a maximum value of contact pressure, i.e., $CPRESS_{max} = 812\ kPa$, occurring at a backfilling distance of $L_d = 16m$. This value is slightly shifted from the median value $L_d = 15m$ or $15m/2$ with $L_d = 30m$.

The value $CPRESS_{max} = 812\ kPa$ which is an upper bound value is comparable to the vertical overburden stress value at $45m$-depth in the trench with a granular density of $1800\ kg/m^3$ i.e., $\sigma_v = \rho \cdot g \cdot h = 1800\frac{kg}{m^3} \times 9.81\frac{N}{kg} \times 45m = 794.6\ kPa.$

Con-III-2: At the end of backfilling process, when quasistatic conditions are reached, the maximum computed contact pressure value is equivalent to the overburden vertical stress at rest which constitutes an upper bound value of predicted CPRESSs, i.e., $CPRESS_{max} = \sigma_{vo} = \rho \times d$

In the case of Model III-long-1m/s (0.5m), there are more zero values of the contact pressure due to an important particle rearrangement during the backfilling process, with particles being released from the top of the stope.

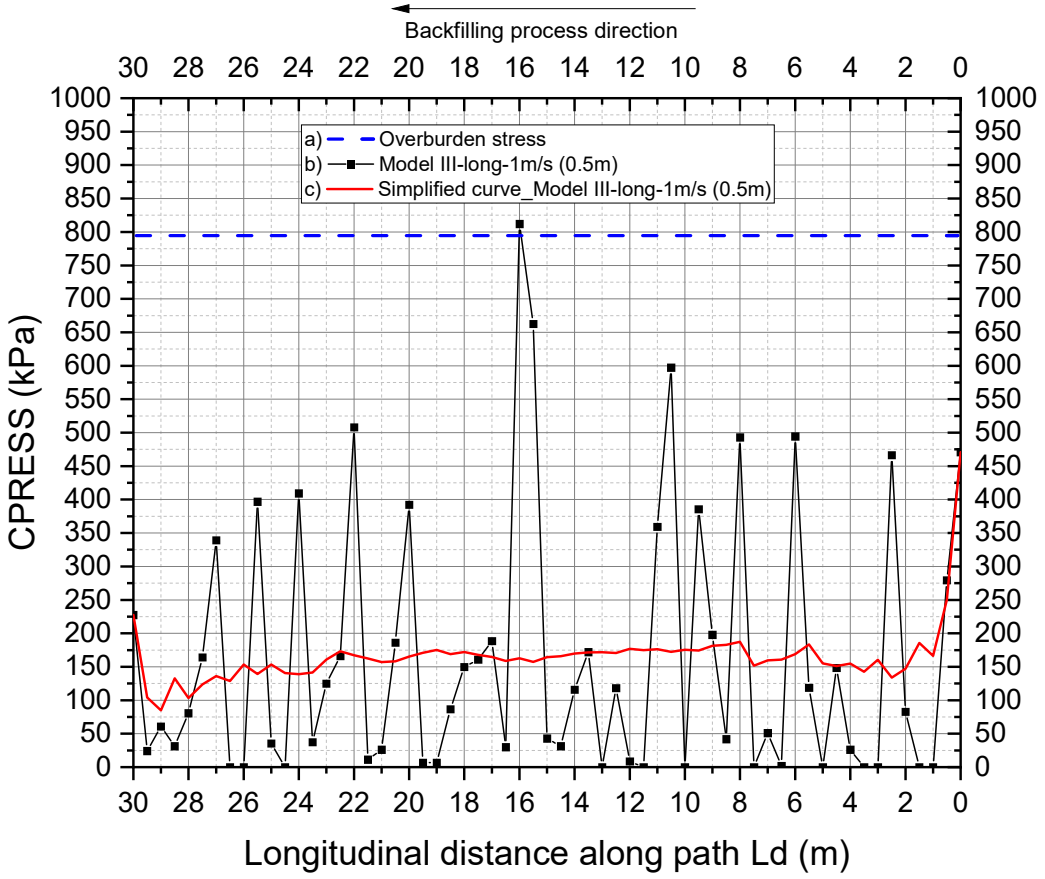

Figure 4-38 CPRESS-L_d curve and its simplified CPRESS-L_d curve, at the end of the backfilling process (t = 70s). Case of Model III-long-1m/s (0.5m).

4.9 PS Model: Plane strain conditions

To model the plane strain conditions with the SPH 3D Abaqus/Explicit model, it was assumed that the plane strain behavior can be reached when the length of the trench (L) is much greater than the value of the width (B), i.e., $L > 5B$. The three plane strain models (PS Model) described in Table 4.1 use the following trench dimensions: $B = 18m$, $H = 45m$ and $L = 90m$.

4.9.1 The PS-SPH Model

4.9.1.1 The assembled parts of PS-SPH Model

As for Model I, Model PS-SPH is composed of two distinct parts i.e.

a. The backfill

The backfill is a parallelepiped with a 45m-height (H), a 18m-width (i.e., B, the transversal direction) and a 90m-depth (i.e., L, the longitudinal direction) corresponding to the initial time $t = 0\ s$ and prior to loading, as shown in Figure 4-39.

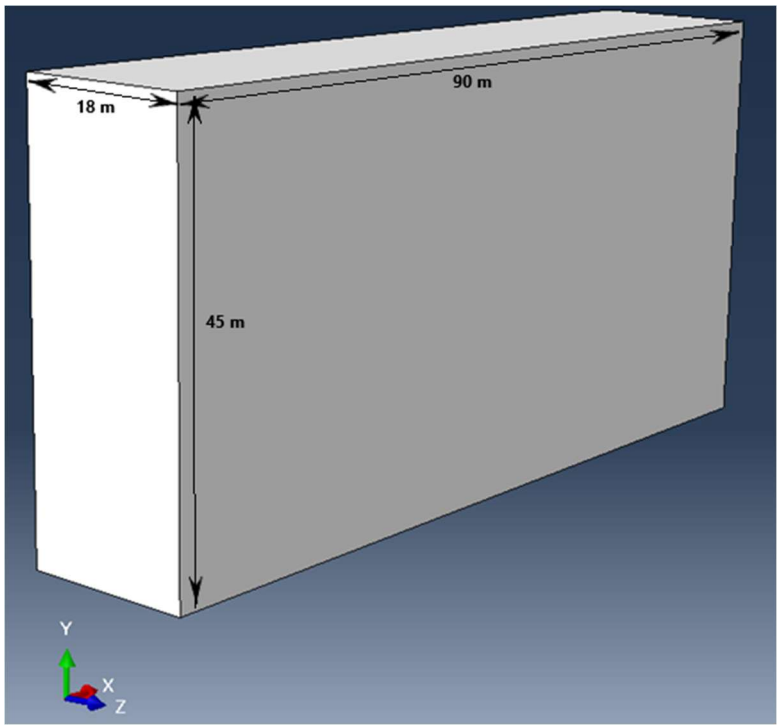

Figure 4-39 Part of the backfill material. Configuration corresponding to PS-SPH Model at the initial time $t = 0s$ and prior to loading.

b. The in-situ rock

The in-situ rock part shown in Figure 4-40 is 49m-height, 398m-width (i.e., the transversal direction) and 470m-depth (i.e., the longitudinal direction). These dimensions correspond to the configuration at the initial time $t = 0\ s$ and prior to gravity loading.

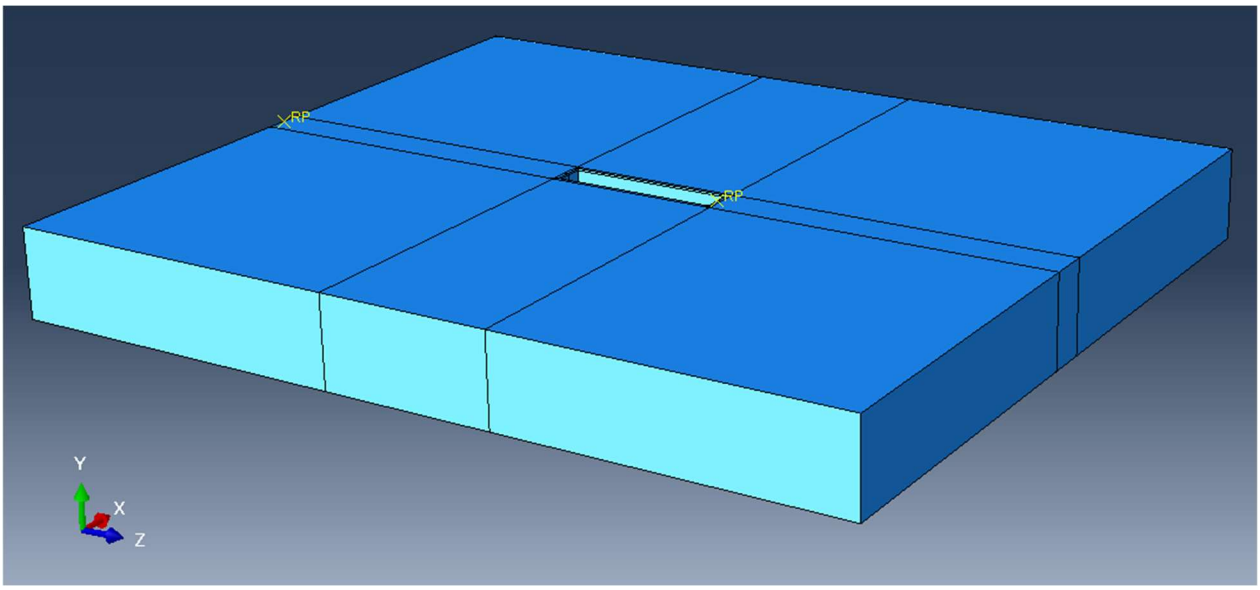

Figure 4-40: 3D representation of the in-situ rock part. Configuration corresponding to PS Model-SPH at initial time t=0s and prior to loading.

In this PS Model-SPH, the in-situ rock was also partitioned in two subparts:

i) The elastic-plastic base rock (Figure 4-41) with its internal surfaces forming the trench or its cavity which is in direct contact with the backfill material particles. The 2m-thikness base rock is 45m-height, 18m-width, and 90m-length (these are the inner dimensions of the trench).

ii) The rigid bedrock having the following global outer dimensions: a 49m-height, a 398m-width, and a 470m-depth. The bedrock was also extruded to obtain a cavity of 47m-height, 22m-width, and 94m-depth, as shown in Figure 4-42. The extrusion is necessary to make room for the base rock whom its external surfaces are fixed to the extruded cavity of in the bedrock.

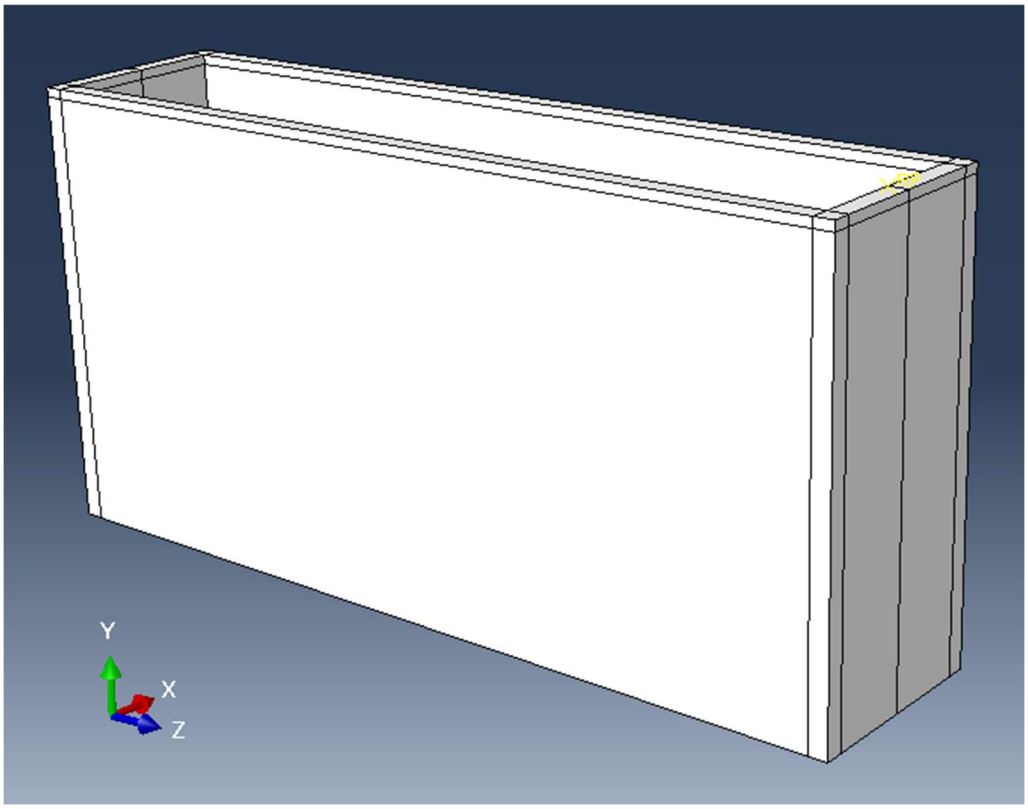

Figure 4-41 : 3D representation of the base rock. Configuration corresponding to all PS Models at initial time t=0s and prior to loading.

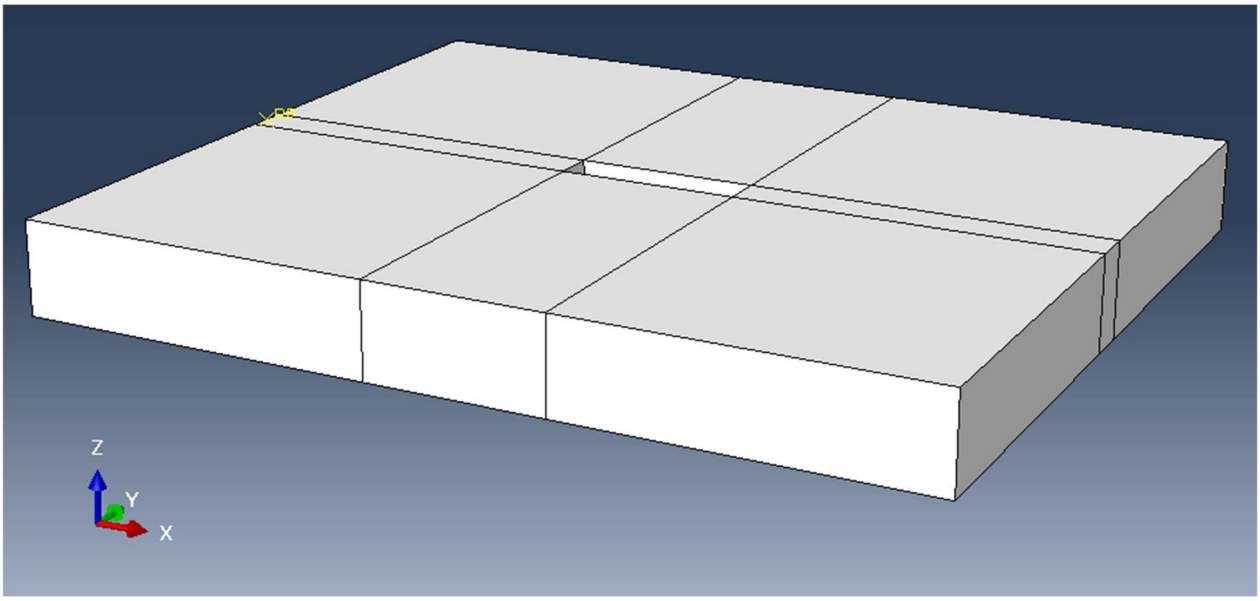

Figure 4-42 : 3D representation of the rigid bedrock. Configuration corresponding to to all PS Models at initial time t=0s and prior to loading.

All parts are assembled at the initial time t = 0s to form the initial configuration of all PS models at initial time t=0s and prior to loading. The assembly is shown in Figure 3.44.

Just like Model I, the base rock part of Figure 4-41 is placed in the trench cavity of the bedrock of Figure 4-42, then the backfill part is preinstalled inside the trench cavity of the base rock to form the assembly model shown in Figure 4-43.

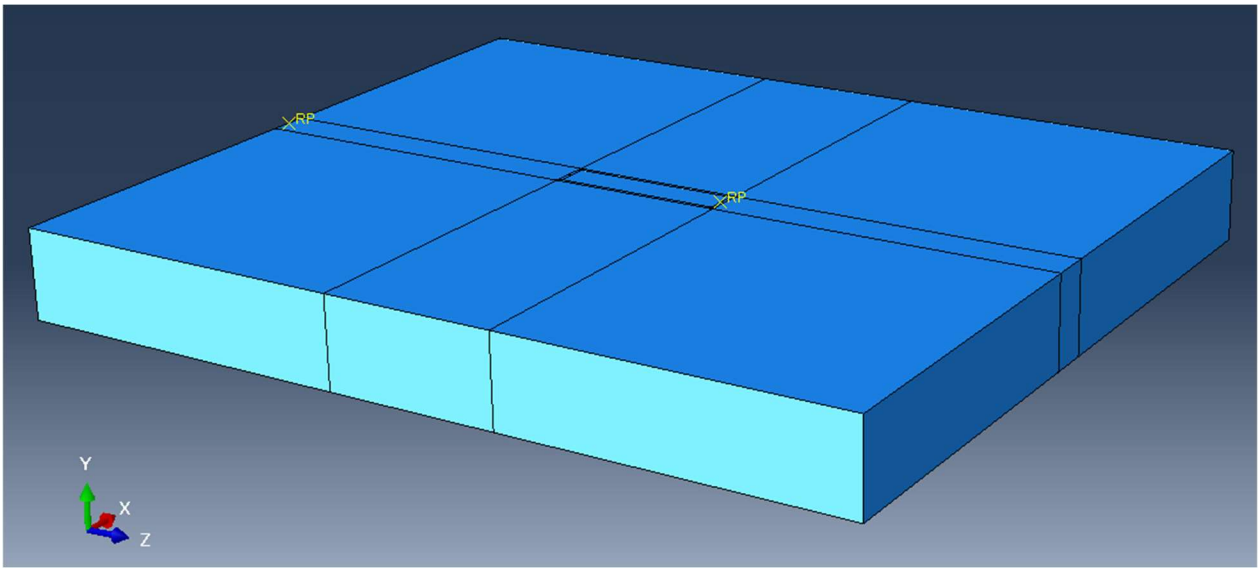

Figure 4-43 : A 3D representation of the two assembled parts. Configuration corresponding to PS Model-SPH at the initial time $t = 0s$ and prior to loading.

The remaining characteristics, such as mechanical properties, analysis step, interaction properties, loading and boundary conditions, and mesh construction properties used to perform the PS Model-SPH are the same as those used in Model I, which was described in section 4.6.1.

4.9.2 Model PS-FEM

Model PS-FEM is a finite element analysis (FEM) application model of Model PS-SPH in which the backfill material was not converted into SPH particles. Other parameters like parts definition mechanical properties, contact properties, boundary conditions, applied load and mesh definition are the same as described in section 4.9.1 for Model PS-SPH.

4.9.3 Model PS-long-1m/s

4.9.3.1 The assembled parts of Model PS-long-1m/s

The parts used in this model consist of the backfill part and the in-situ rock part described in section 4.9.1.1 with a supplemental upper rigid box (Figure 4-44). The inner dimensions of the rigid box of $2m$-thickness are: $45m$-height, $18m$-width (in transversal direction) and 90m-depth (in longitudinal direction). The box has a $6.75m \times 18m$ rectangular opening (Figure 4-44). The opening allows the granular material inside the upper rigid box to flow inside the trench when the rigid box is uniformly displaced to backfill the trench. Figure 4-45 represents Model PS-long-1m/s assembly at initial time ($t = 0$).

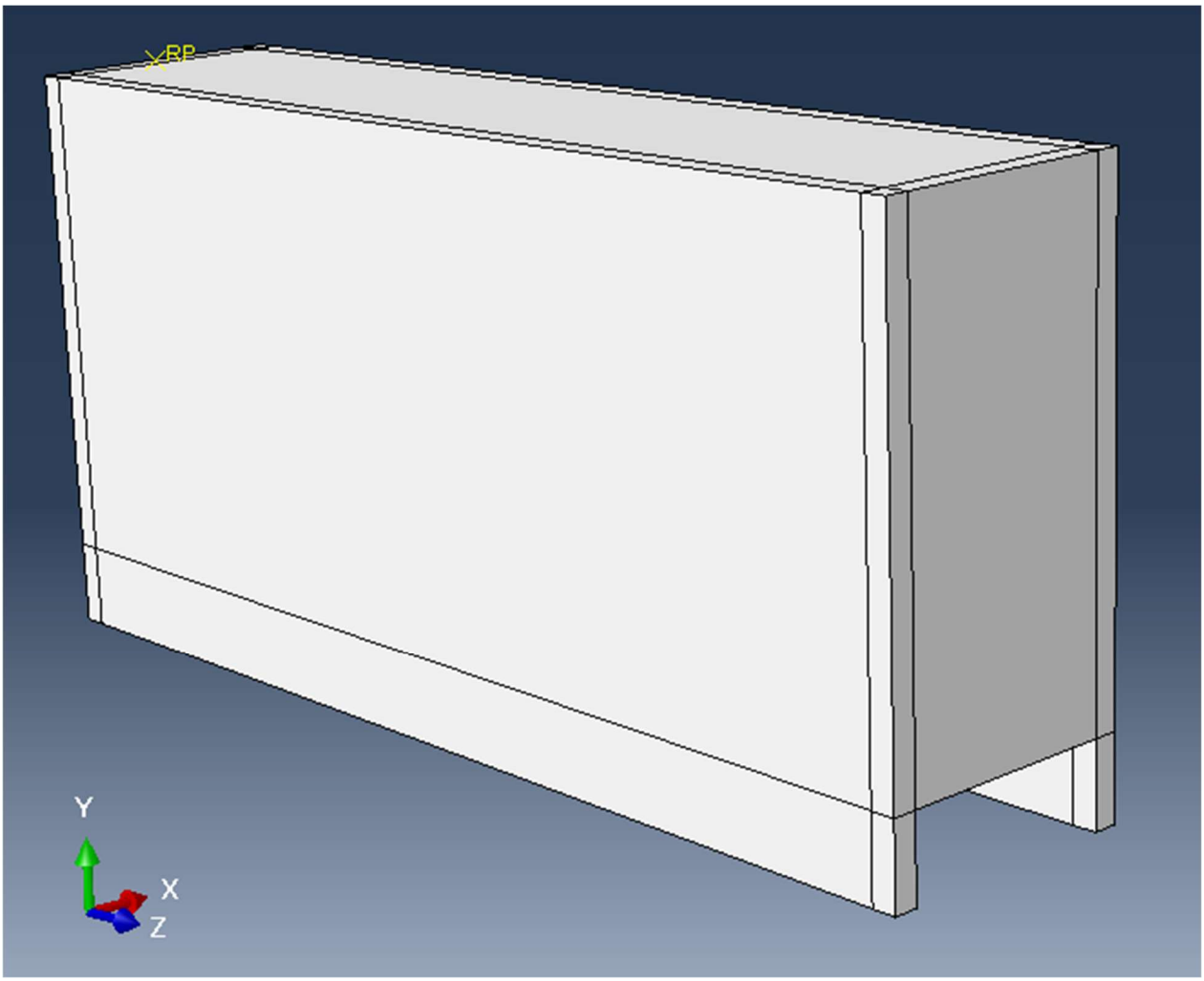

Figure 4-44 The upper rigid box-long part at initial time ($t = 0$). Case of Model PS-long-1m/s.

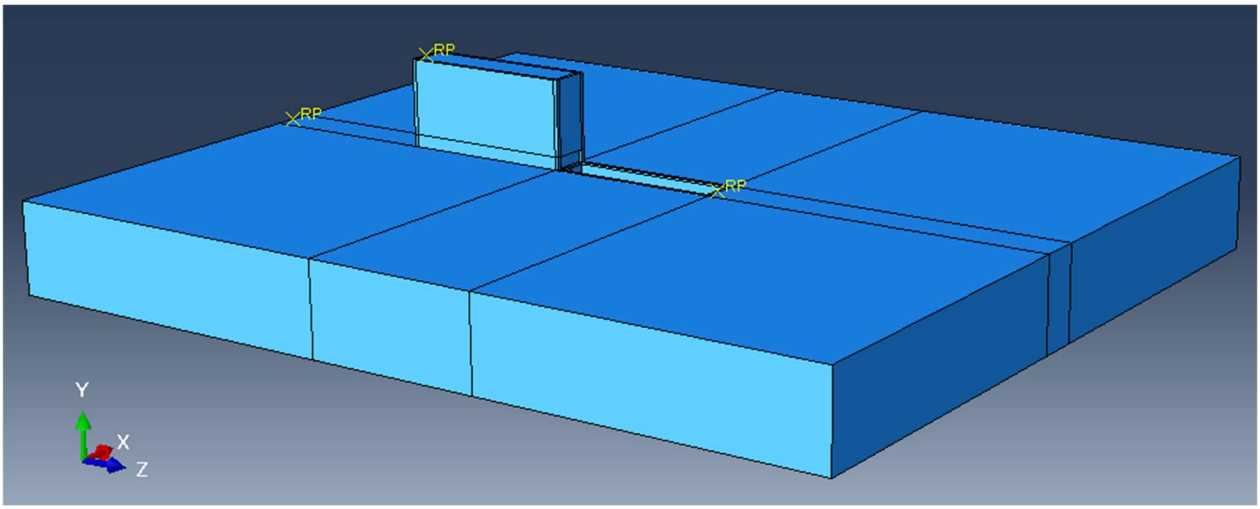

Figure 4-45 Assembled parts. Configuration corresponding to Model PS-long-1m/s at the initial time $t = 0s$ and prior to gravity loading.

4.9.3.1 The step of backfilling

In the same way as in the case of Model III describing the UCPBP process, an explicit dynamic analysis was also used in a single step time for PS-long-1m/s. In this model, the step duration was 190s as the upper rigid box underwent a displacement distance of $190m$ at a rate of $1m/s$.

All the other parameters used in this model are the same as for Model III described in section 4.8.1.

Results of the plane strain model will be presented in section 5.5 and include the distribution of the contact pressure along the transversal distance path Lt (m), as defined in Figure 4-46.

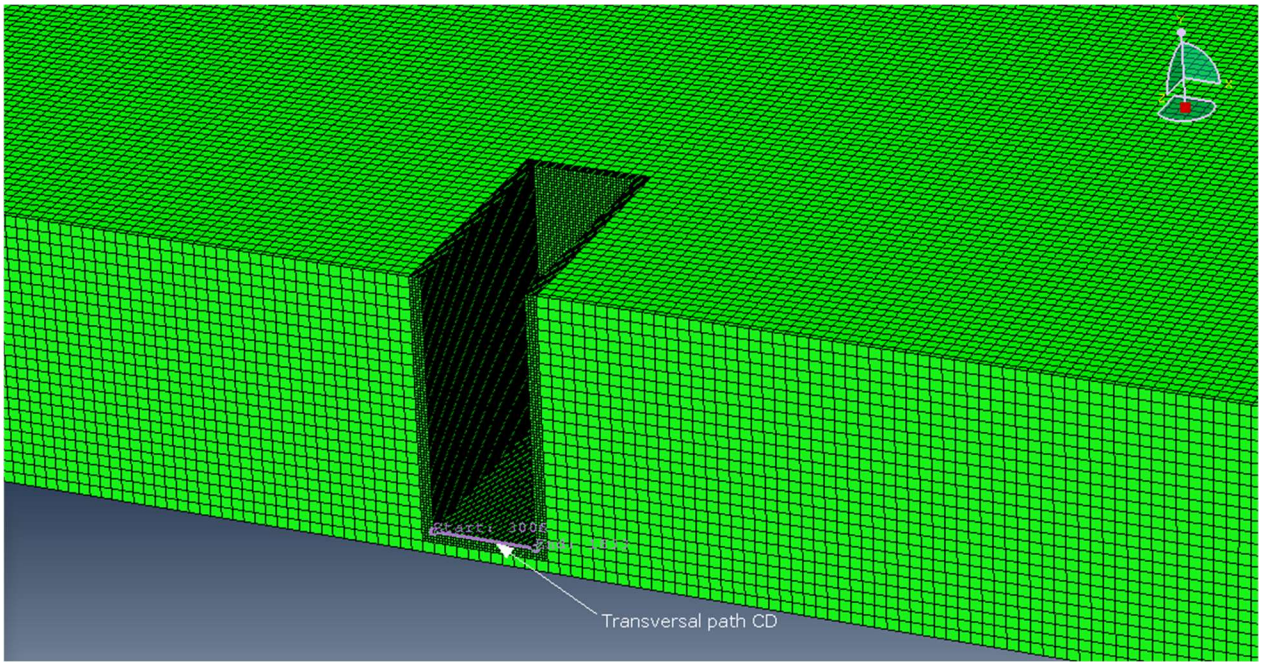

Figure 4-46 Path CD in the transversal vertical middle section corresponding to t = 0s, for all PS models.

The outputted results of all plane strain simulations are compared to the finite difference method results as presented by Li and Aubertin (2008) in section 5.5 as well.

CHAPTER 5 EFFECT OF THE BACKFILLING MODE ON BACKFILLED STOPE: A NUMERICALLY BASED ASSESSMENT

5.1 SPH versus FEM based CPRESSs curves - effect of UCPBP

Predictive results deduced from Models I, II and III outputs are shown in Figure 5-1 for the same stope dimensions of 15m x 30m x 45m. In fact, three distinct curves of contact pressures (CPRESSs) computed along the bottom of the stope are depicted in Figure 5-1. Examination of the results permits to draw the following conclusions:

i. Regarding the results obtained from the analyses of Model II (FEM-WIP), it can be shown that curve b) in Figure 5-1, i.e., the CPRESS-L_d curve along the path AB (which was previously defined in Figure 4-19) is continuous but not uniform. Examination of curve b) in Figure 5-1 shows that CPRESS is maximum in the middle-path (i.e. for $L_d = 15m$) and it strictly decreases when moving away from the middle-path to reach a minimum value of 460 kPa at both vertical boundaries i.e. for $L_d = 0m$ and $L_d = 30m$. The discrepancy is due to the arching effect conditioned by the location of the vertical boundaries and because a stress transfer between the stiff backfill material and the stiffer surrounding rock mass due to friction at the interface of the two materials induces a reduction of the pressure and the stress near the boundary walls. The latter result confirms what was also previously found by Li and Aubertin (2008).

ii. Curve c) in Figure 5-1 depicts the distribution of CPRESSs along path AB for which an initial wished-in-place configuration of structured particles was assumed. In the same manner as in above., CPRESS values at the cavity vertical boundaries $L_d = 0m$ and $L_d = 30m$ are 1125 kPa and 190 kPa respectively. It is important to recall that curve c) represents the state of CPRESSs at the end of the step time of the explicit dynamic procedure of the analysis. Here again, the rearrangement of the particles which occurs during the analysis, causes a new state of interfacial contact stresses described by:

1) A CPRESS at the beginning of the path, i.e., CPRESS ($L_d = 0m$) = 1125 kPa higher than the CPRESS at the end of the same path, i.e., CPRESS ($L_d = 30m$) = 190 kPa; and

2) In the same manner, this rearrangement of the particles causes an over-stressed contact pressure in the portion of path AB delimited by $L_d = 25.1$m and $L_d = 27.8m$, as shown in Figure 5-1. Computed values of CPRESSs corresponding to this portion are higher than the value of the overburden pressure as it appears in curves a) and c) in Figure 5-1. It is believed that such rearrangement which can cause a dense gathering of particles in this portion of the interface will increase CPRESSs in contact points belonging to this portion.

iii. In the case of curve d) of model III (SPH-UCPBP), it is believed that the direction of the backfilling process, which starts at the beginning of path AB at $L_d = 0m$ and ends at $L_d = 30m$, as shown in Figure 5-1; is responsible of causing :

1) a higher CPRESS at the start of the path and a lower one at its end i.e., CPRESS ($L_d = 0m$) = 460 kPa and CPRESS ($L_d = 30m$) = 230 kPa.

2) a slight decrease in CPRESSs when moving along the longitudinal interface path in the same direction of the backfilling process. It is important to mention that the gradient of CPRESSs is low for the quasilinear portion of the curve d) bounded between $L_d = 1m$ and $L_d = 29m$ where CPRESS ($L_d = 1m$) = 170 kPa and CPRESS ($L_d = 29m$) = 80 kPa, respectively.

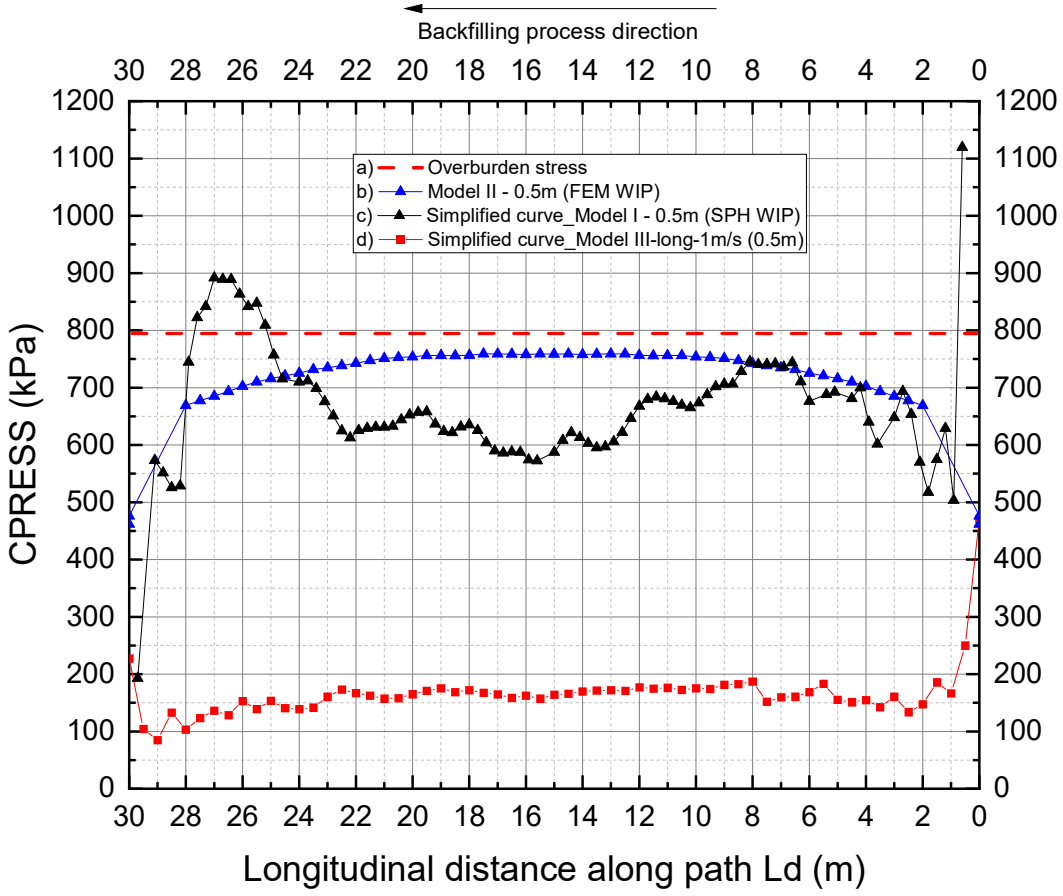

Figure 5-1 Distribution of contact pressures (CPRESS) vs longitudinal distance along the bottom interface path: a) Overburden stress, b) Model-II-0.5m-FEM, c) simplified curve Model-I-0.5m-SPH, d) simplified curve Model-III-long-1m/s-(0.5m).

5.2 Effect of initial mesh density on computed CPRESSs in an UCPBP

Figure 5-2 shows values of CPRESSs deduced from simulations that were previously described in Table 4.1. On the basis of this figure, the following conclusions have been drawn:

i) Figure 5-2 shows that curve e) is above curve f) indicating that CPRESSs deduced from an initial seed (or initial mesh density) of 0.5m are slightly higher than those deduced from an initial seed of 0.8. These two curves were obtained for a rate of backfilling of 1 m/s. It is concluded that, in general, and for a specific initial mesh density, it is expected that values

of CPRESSs increase when the seed of particles decreases (or when the initial mesh density decreases).

ii) In Figure 5-2, curve a) was determined based on an initial structured mesh of the backfill's material in which particles have a diameter of 0.25m or 25cm. Such diameter is the 50% of 0.5m and 31.25% of 0.8m particles diameter used in the case of curves e) and f) respectively. Along interfacial path, CPRESSs in the case of curve a) remain higher than those of curves e) and f), despite that the three preceding curves were deduced from simulations carried out with the same rate of backfilling of 1m/s. Although the two curves e) and f) are comparable, CPRESS of curve a) increases from 130kPa (for $L_d = 0m$) to reach 2700kPa (for $L_d = 27m$) and decreases after that to 530kPa at the end of the path i.e., $L_d = 30m$.

Here again, such aforementioned discrepancy may be explained by particles rearrangement within the excavated rock, and it is caused by the change of the granular backfill material configuration from an initial state corresponding to t = 0s to an intermediate state corresponding to a time t superior to 0s, in particular, when this time corresponds to the end of the step time (or at the end of the performed simulation). Figure 5-3 shows the initial volume V_i of backfill material particles initially located within the upper rigid box (shown in Figure 4-22) of the initial assembly configuration. In the case of Model-III-long-1m/s-(0.5m), V_i = 20m x 15m x 30m = 9000m^3 contains 72000 particles at the initial time t = 0s. Output results of this model show that 20000 particles or 27.78% (or 20000 of 72000) of the initial number of backfill material particles that were located within the upper rigid box (Figure 5-3) were left outside the stope at the end of the UCPBP, as shown in Figure 5-4. This simply means that only 52000 particles or 72.22% of the initial number of particles were used to complete the UCPBP, as presented in Table 5.1.

The initial mesh of the granular material (Figure 5-3) was constructed using a structured mesh and its elements are arranged in a dense manner at the initial time corresponding to t = 0s. During the UCPBP, these elements will flow arbitrarily and fall in the excavation after being converted to smoothed particles. In the initial structured mesh, it was assumed that the backfill had unit weight of 18.0 kN/m^3, it is the same numerical value used by Li

and Aubertin (2008). Therefore, the load applied to each particle for Model-III-long-1m/s(0.5m) will be $\left(18.0\frac{kN}{m^3} \times 20m \times 30m \times 15m\right) \div 72000\ particles = 2.25\ kN/particle$. The average unit weight of the backfilled stope will be in this case $(2.25 \times 52000\ particles) \div (45m \times 30m \times 15m) = 5.78\ kN/m^3$. Such change is due to particle rearrangement that occurs during the continuous backfilling process and is responsible of lowering CPRESSs belonging to curves e and f in Figure 5-2 for example. In the case of Model-I-0.5m-SPH, curve b exhibits significantly higher CPRESSs values than curves e and f because the WIP backfill dense configuration was initially installed within the stope which contain the same number of particles at the start and the end of the simulation process.

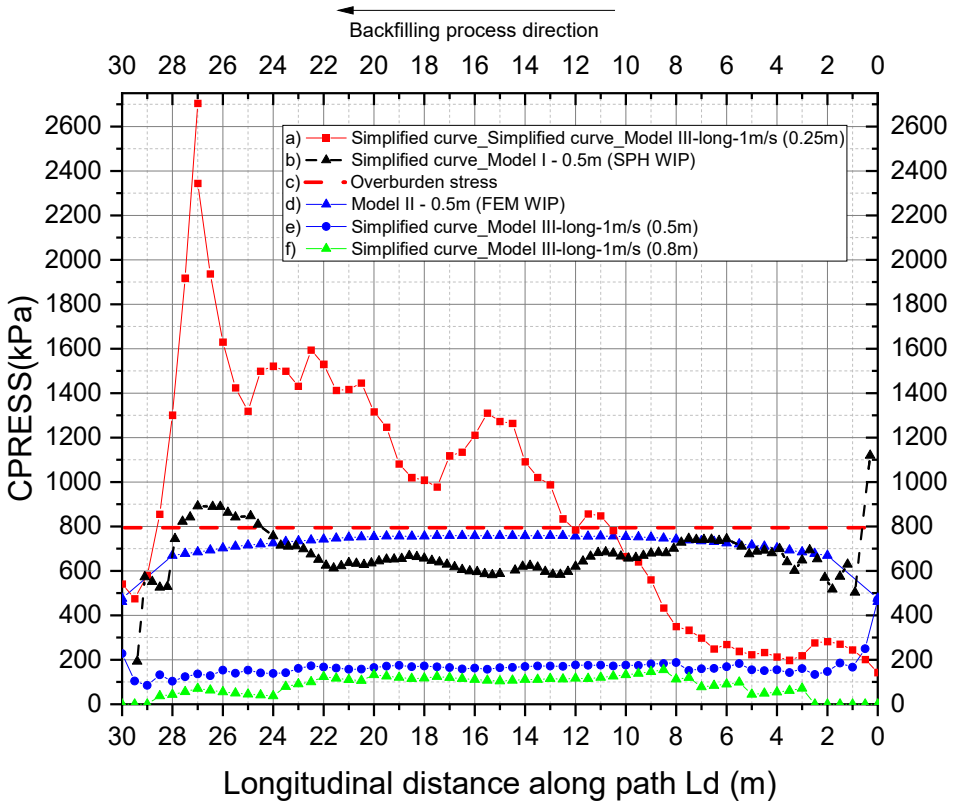

Figure 5-2 Distribution of contact pressures (CPRESS) vs longitudinal distance (L_d) along path: a) simplified curve Model-III-long-1m/s-(0.25m); b) simplified curve Model-I-0.5m-SPH; c) Overburden stress; d) Model-II-0.5m-FEM, e) simplified curve Model-III-long-1m/s-(0.5m); and f) simplified curve Model-III-long-1m/s-(0.8m).

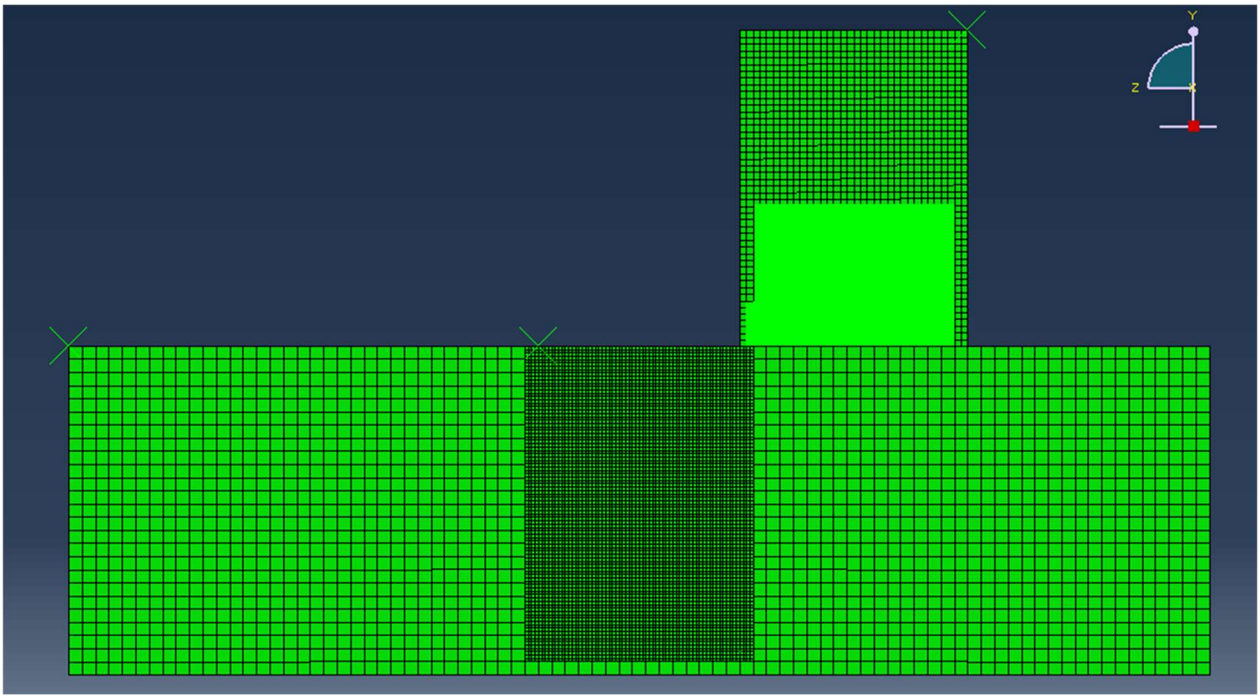

Figure 5-3 Location of the particles in the initial volume at the initial configuration corresponding to the initial time t = 0s. Case of the simulation Model-III-long-1m/s-(0.5m)

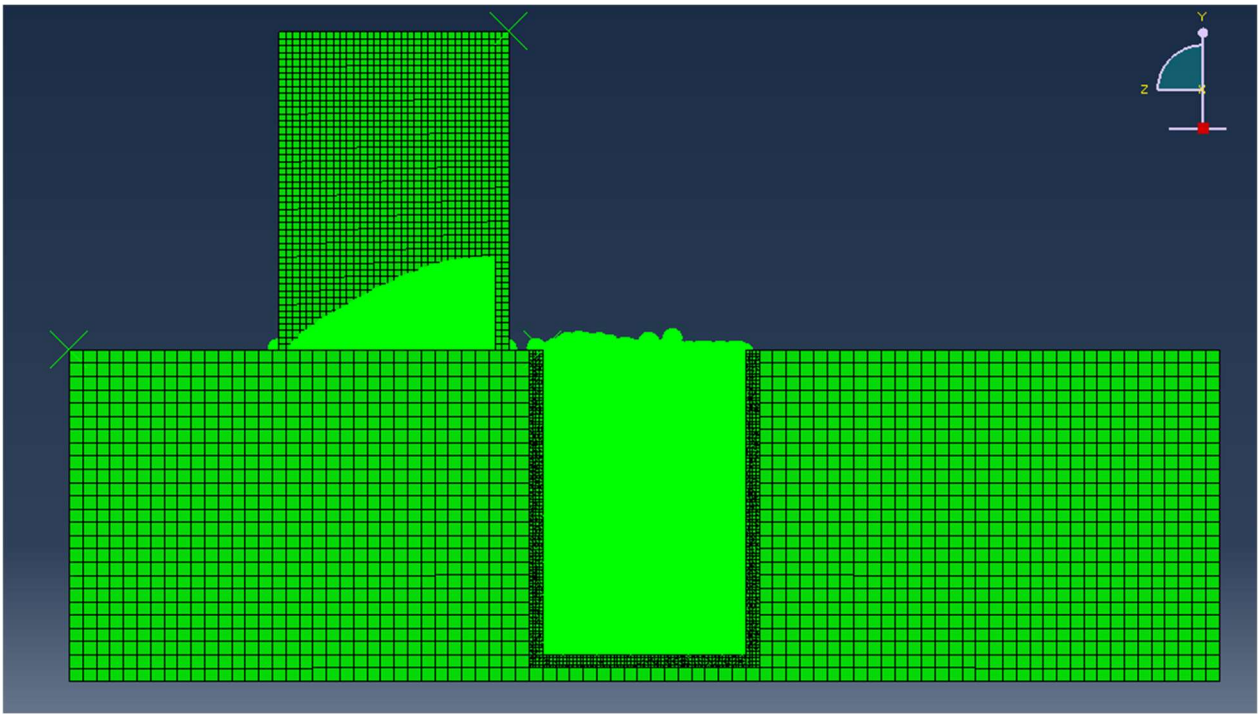

Figure 5-4 Location of the particles at the end of the simulation Model-III-long-1m/s-(0.5m)

5.2.1 Conclusions

It is concluded that an assumed wished-in-place model is unable to account for the change of the unit weight of the backfill material and therefore is unrealistic because the computed stresses and strains depend on the initial total number of particles contained in the upper box and therefore, they depend on the initial seed or the initial mesh density determined by the diameter of the spherical particles. The SPH-based dynamic process of backfilling provides more realistic computed stresses because it takes into account the rearrangement of all particles during and at the end of the simulated backfilling process. This phenomenon is confirmed in practice on the site when dealing with backfilling an arbitrary excavation with granular material. Such conclusion was always validated physically because it has been noticed that the number of particles per unit volume (NPUV) of an in-situ granular material which is initially structured is always higher than the NPUV of the same material being restructured after rearrangement of particles.

Table 5.1 Number of particles in stope at the end of the simulations for different particle densities

Particle's Mesh (seed)	0.8 m	0.5 m	0.25 m
Initial total number of particles	17100	72000	576000
Number of particles in the stope at the end of the simulation	11500	52000	433800
% of particles in the stope at the end of the simulation	67.25%	72.22%	75.31%

5.3 Effect of the speed of the backfilling process

Predicted values of contact pressures, for simulations of Models I, II and III of different backfilling processes with different backfilling velocities are presented in Figure 5-5 and Figure 5-6. These simulations represent backfilling processes along the transversal and the longitudinal directions for three different imposed velocities of $1m/s$, $0.75m/s$ and $0.5m/s$. Based on the numerical results, the following conclusions are drawn:

1. Figure 5-5 shows that contact pressure values of curve f ($0.5m/s$) are lower than values of curve d ($0.75m/s$) and e ($1m/s$) in the portion of path AB delimited by $L_d = 25m$ and $L_d = 4m$. In the same manner, values of contact pressure of curve d ($0.75m/s$) are lower than those of curve e ($1m/s$) in the portion of path AB delimited by $L_d = 20m$ and $L_d = 4m$. It is concluded that, in general, it is expected that values of CPRESSs increase when the backfilling velocity increases.
2. At the initial time of t = 0s, 72000 backfill material's particles are located within the upper rigid box at the initial assembly configuration for all simulations. Results show that only 59000 particles or 81.94% of the initial number of particles were used to complete the UCPBP for a backfilling velocity of $1m/s$; 55200 particles or 76.67% of the initial number of particles were used to complete the UCPBP for a backfilling velocity of $0.75m/s$; and 49800 particles or 69.17% of the initial number of particles were used to complete the UCPBP for a backfilling velocity of $0.5m/s$. These results are also presented in Table 5.2 and it is concluded that a high backfilling velocity leads to a larger number of particles within the excavated rock thus inducing greater values of contact pressure.

Table 5.2 Number of particles in stope at the end of the simulations (effect of backfilling velocity)

Velocity	1 m/s	0.75 m/s	0.5 m/s
Initial total number of particles	72000	72000	72000
Number of particles in the stope at the end of the simulation	59000	55200	49800
% of particles in the stope at the end of the simulation	81.94%	76.67%	69.17%

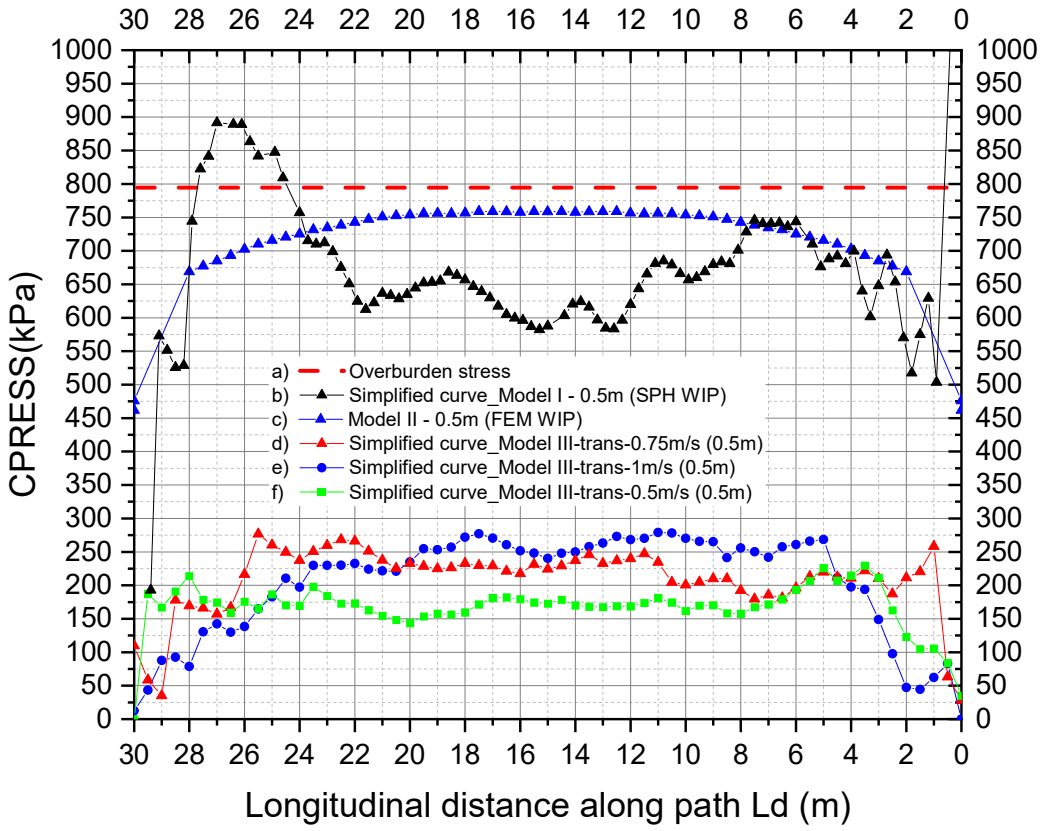

Figure 5-5 Distribution of contact pressures (CPRESS) vs longitudinal distance (L_d) along path for UCPBP along transversal direction: a) Overburden stress, b) simplified curve_Model I – 0.5m, c) Model II – 0.5m, d) simplified curve_Model III-trans-0.75m/s (0.5m) e) simplified curve_Model III-trans-1m/s (0.5m), f) simplified curve_Model III-trans-0.5m/s (0.5m).

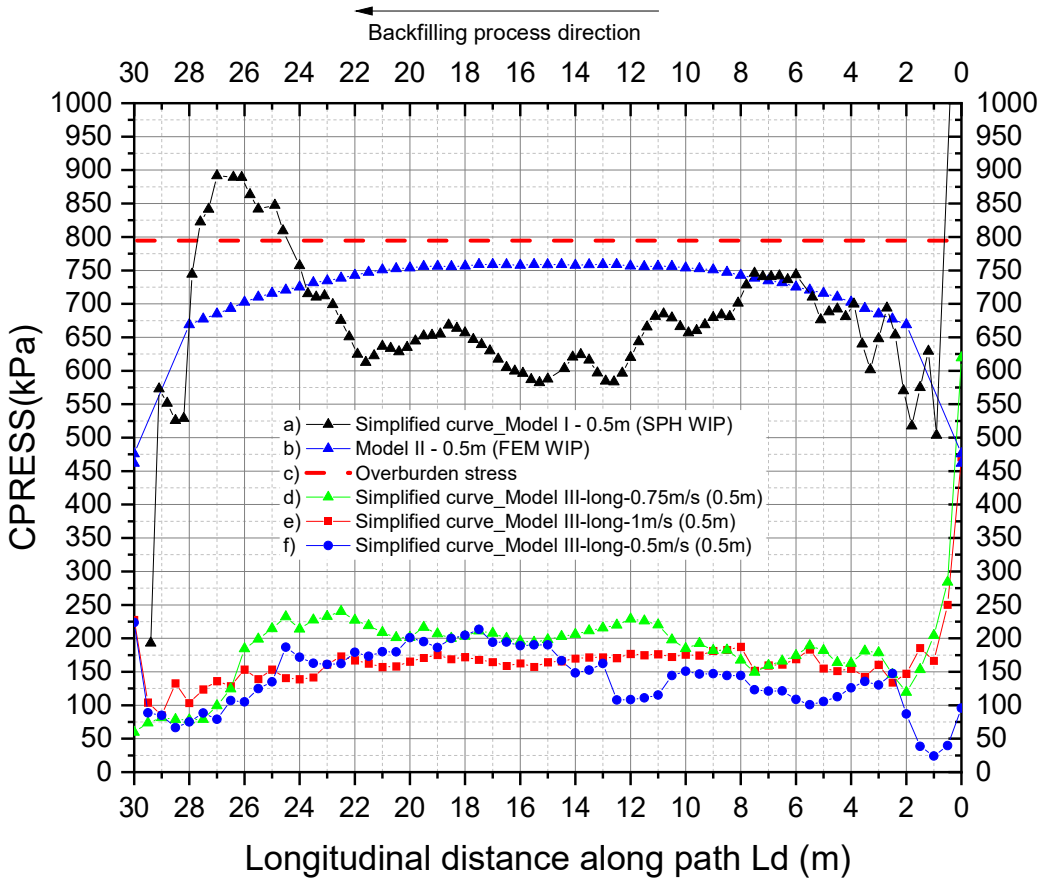

Figure 5-6 Distribution of contact pressures (CPRESS) vs longitudinal distance (L_d) along path for UCPBP along longitudinal direction: a) simplified curve_Model I – 0.5m , b) Model II – 0.5m, c) Overburden stress, d) simplified curve_Model III-long-0.75m/s (0.5m), e) simplified curve_Model III-long-1m/s (0.5m), f) simplified curve_Model III-long-0.5m/s (0.5m).

5.4 Effect of the backfilling mode

The data depicted in Figure 5-7, Figure 5-8 and Figure 5-9 refer to the results of Model III describing the backfilling process in the longitudinal and transversal direction. The following conclusions can be drawn from the curves presenting the contact pressures (CPRESS) computed along the path of the bottom of the stope:

i. Curve d and e (backfilling velocity of 1m/s in Figure 5-7) show that CPRESSs deduced from the transversal backfilling process are higher than those deduced from the longitudinal

backfilling process, in the middle section of the curves (from $L_d = 3m$ to $L_d = 26m$). The same observation is made in Figure 5-8, where curves d and e (backfilling velocity of 0.75m/s) show higher values of the CPRESSs deduced from transversal backfilling process in the middle section of the curves (from $L_d = 1m$ to $L_d = 29m$). However, in Figure 5-9 results are different because curves d and e (backfilling velocity of $0.5m/s$) show higher values of the CPRESS deduced from transversal backfilling process, but only for approximatively half of the distance along the path (from $L_d = 0.5m$ to $L_d = 14.5m$ and $L_d = 24.5m$ to $L_d = 29.5m$). It is concluded that in general for values of CPRESSs are higher for a backfilling process in the transversal direction.

ii. In Figure 5-7, Figure 5-8 and Figure 5-9, curves d and e show that, in general, at the start and at the end of the path, CPRESSs deduced from the longitudinal backfilling process are higher than values of CPRESSs deduced from the transversal backfilling process. In the case of curves d and e (backfilling velocity of 1m/s) in Figure 5-7, at the start of the path ($L_d = 0m$) values of CPRESS are equal to 460 kPa for the longitudinal backfilling process and 0 kPa for the transversal backfilling process. At the end of the path ($L_d = 30m$), values of CPRESS are equal to 230 kPa for the longitudinal backfilling process and 10 kPa for the transversal backfilling process.

iii. Examination of curve d in Figure 5-7, Figure 5-8 and Figure 5-9 (transversal backfilling process) shows that CPRESS is minimum at the start and the end of the path and tend to increase toward the middle-path. These results show a performance similar to the arching effect conditioned by the location of the vertical boundaries where a stress transfer occurs between the stiff backfill material and the stiffer surrounding rock mass due to friction at the interface of the two materials, thus causing a reduction of pressure and the stress near the boundary walls.

iv. At the initial time t = 0s, 72000 backfill material's particles are located within the upper rigid box at the initial assembly configuration for all simulations, as noted in Table 5.3. Results show that for the same velocity of backfilling process, more particles were needed to complete the transversal backfilling process than the longitudinal one. In the case of a backfilling velocity of 1m/s, 52000 particles or 72.22% of the initial number of particles

were used to complete the longitudinal backfilling process and 59000 particles or 81.94% of the initial number of particles were used for the transversal backfilling process. It is concluded from these results that, in general, a transversal backfilling process leads to a larger number of particles within the excavated rock, thus causing greater values of contact pressure.

Table 5.3 Number of particles in stope at the end of the simulations (effect of backfilling mode)

Velocity	1 m/s		0.75 m/s		0.5 m/s	
Backfilling direction	longitudinal	transversal	longitudinal	transversal	longitudinal	transversal
Initial total number of particles	72000	72000	72000	72000	72000	72000
Number of particles in the stope at the end of the simulation	52000	59000	48400	55200	43600	49800
% of particles in the stope at the end of the simulation	72.22%	81.94%	67.22%	76.67%	60.55%	69.17%

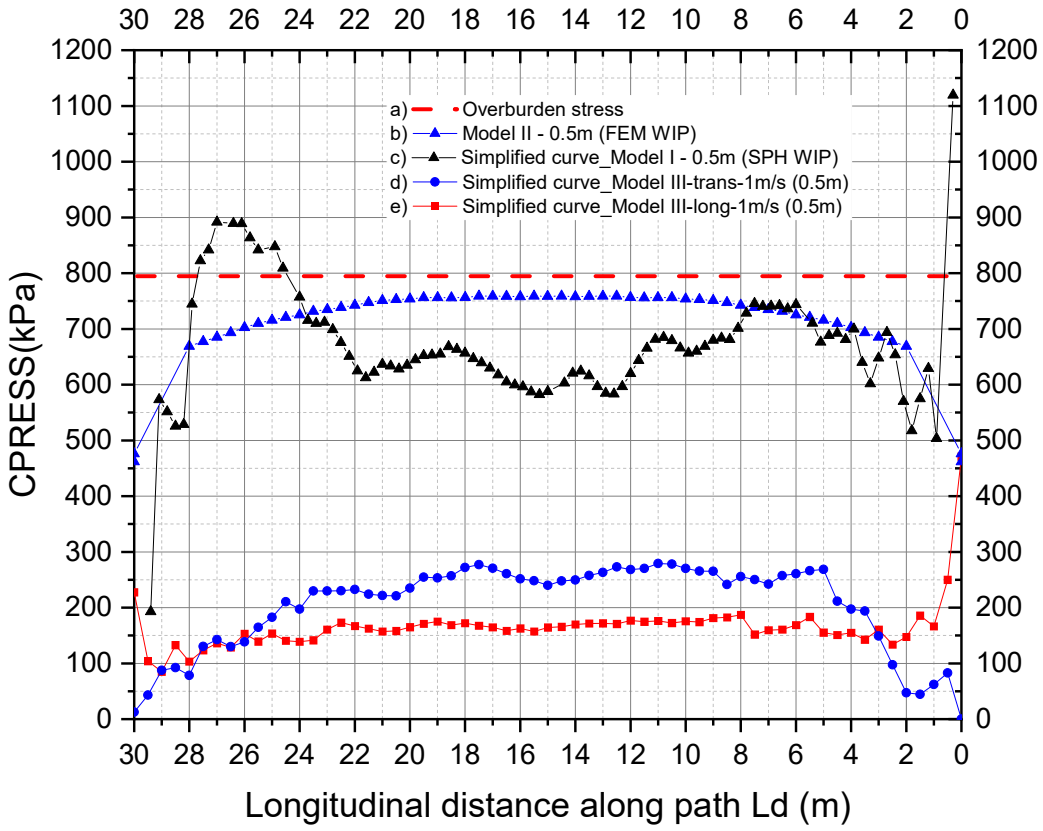

Figure 5-7 Distribution of contact pressures (CPRESSs) vs longitudinal distance (L_d) along path for UCPBP: a) Overburden stress , b) Model II – 0.5m , c) simplified curve_Model I – 0.5m, d) simplified curve_Model III-trans-1m/s (0.5m), e) simplified curve_Model III-long-1m/s (0.5m).

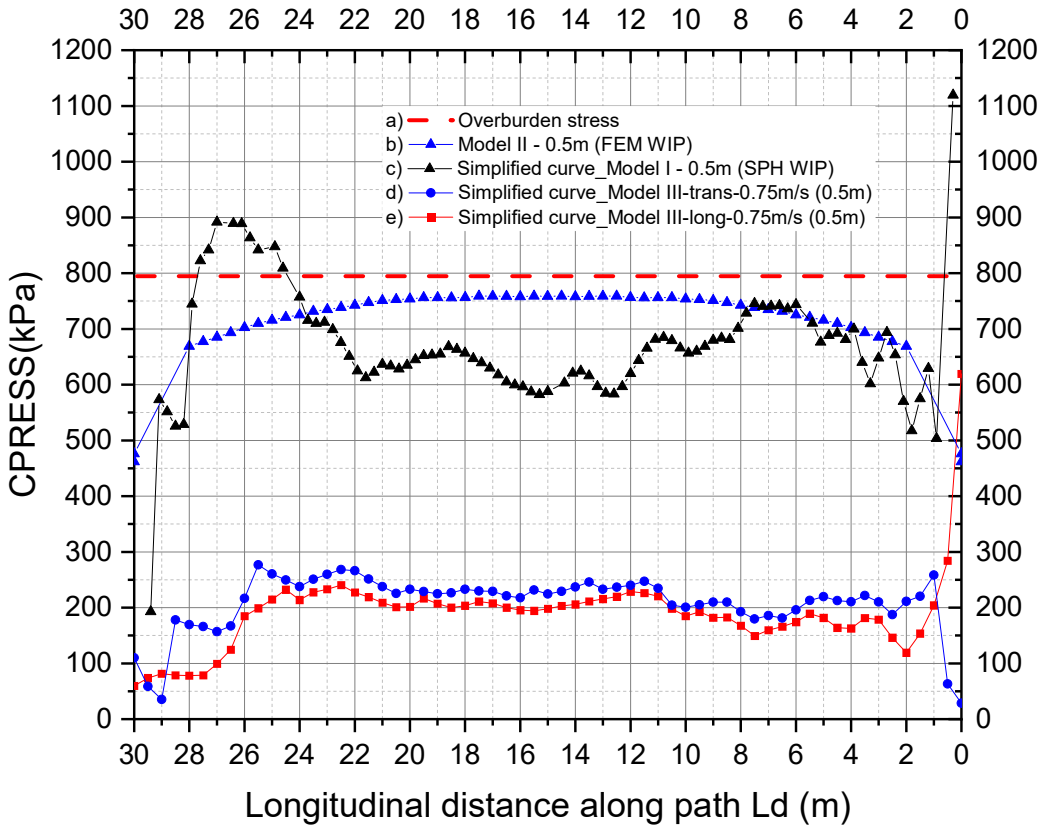

Figure 5-8 Distribution of contact pressures (CPRESS) vs longitudinal distance distance (L_d) along path for UCPBP: a) Overburden stress , b) Model II – 0.5m , c) simplified curve_Model I – 0.5m, d) simplified curve_Model III-trans-0.75m/s (0.5m), e) simplified curve_Model III-long-0.75m/s (0.5m).

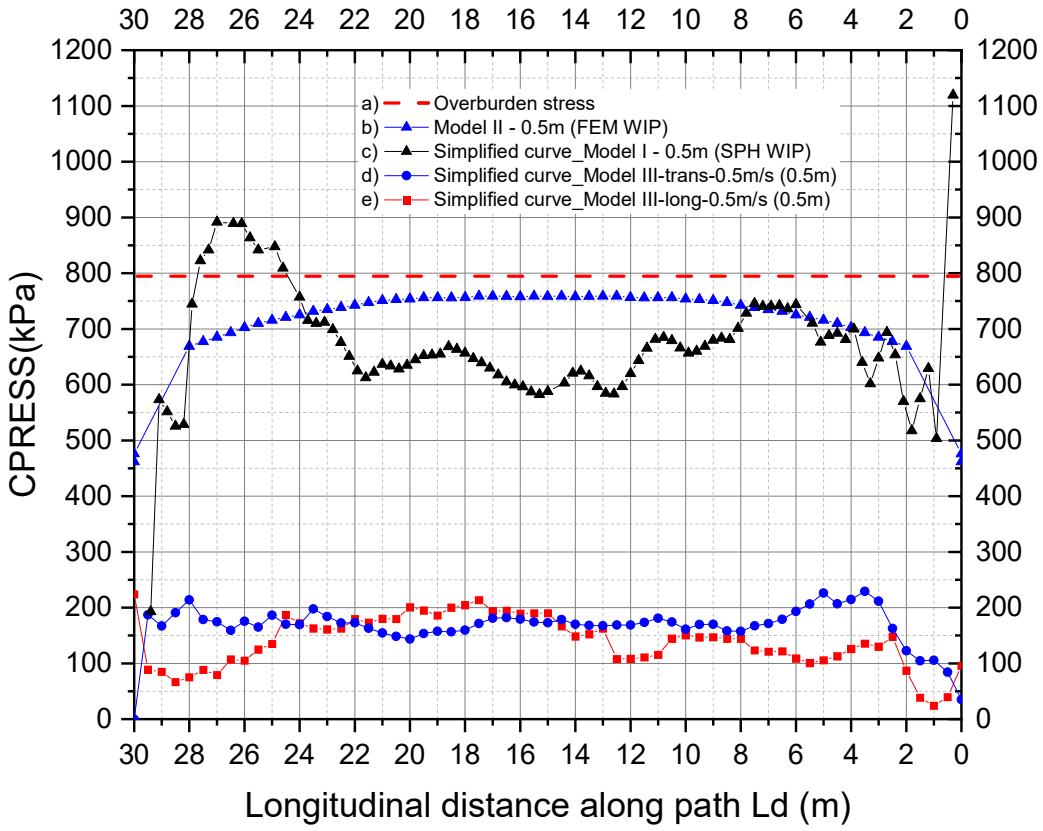

Figure 5-9 Distribution of contact pressures (CPRESS) vs longitudinal distance (L_d) along path for UCPBP: a) Overburden stress , b) Model II – 0.5m , c) simplified curve_Model I – 0.5m, d) simplified curve_Model III-trans-0.5m/s (0.5m), e) simplified curve_Model III-long-0.5m/s (0.5m).

5.5 The plane strain model results

Results of the plane strain model which are presented in Figure 5-10 show the distribution of the contact pressure along the transversal distance path L_t(m). In addition,

i. The FEM_WIP curve (curve a) shows that the CPRESS strictly increases from the vertical boundaries of the trench (two vertical planes of the cavity of the trench passing through points $L_t = 0m$ and $L_t = 18m$) to the symmetrical plane passing through $L_t = 9m$. At $L_t = 0m$ and $L_t = 18m$, CPRESS = 665.4 kPa; at the center where $L_t = 9m$, CPRESS

reaches the value of 905.3 kPa. This shows that the contact pressure does not have the same value at a given width (45m in this case), as mentioned in section 4.7.2 for Model II (FEM_WIP). Such phenomenon is due to the arching effect as described by Li and Aubertin (2008) as a stress transfer between the soft backfill material and the stiffer surrounding rock mass due to friction at the interface of the two materials which has an effect to reduce the pressure and stress near the walls. It is also observed that most values of CPRESS are above the overburden stress curve (curve b).

ii. The smooth SPH_WIP curve (curve c) is showing extreme values of contact pressure at the vertical walls of the trench. At $L_t = 0m$, CPRESS = 1357.3 kPa and for $L_t = 18m$, CPRESS = 250.2 kPa. In the middle section, values of contact pressure are lower than the value of the overburden stress of 794.6 kPa depicted in curve b.

iii. The simplified SPH-UCPBP curve (curve e) depicted in Figure 5-10 shows a non-uniform distribution of the CPRESS consistent with the results predicted by Model III. Higher values of CPRESSs are obtained at the edges of the stopes at $L_t = 0m$ and $L_t = 18m$. For $L_t = 0m$, CPRESS = 960.1 kPa; for $L_t = 1m$, CPRESS = 1062.8 kPa; and for $L_t = 18m$, CPRESS = 933 kPa. These values are higher than the value of the overburden stress of 794.6 kPa. It is also observed that curve e values are the closest to curve d showing the result of the contact pressure distribution as presented by Li and Aubertin (2008).

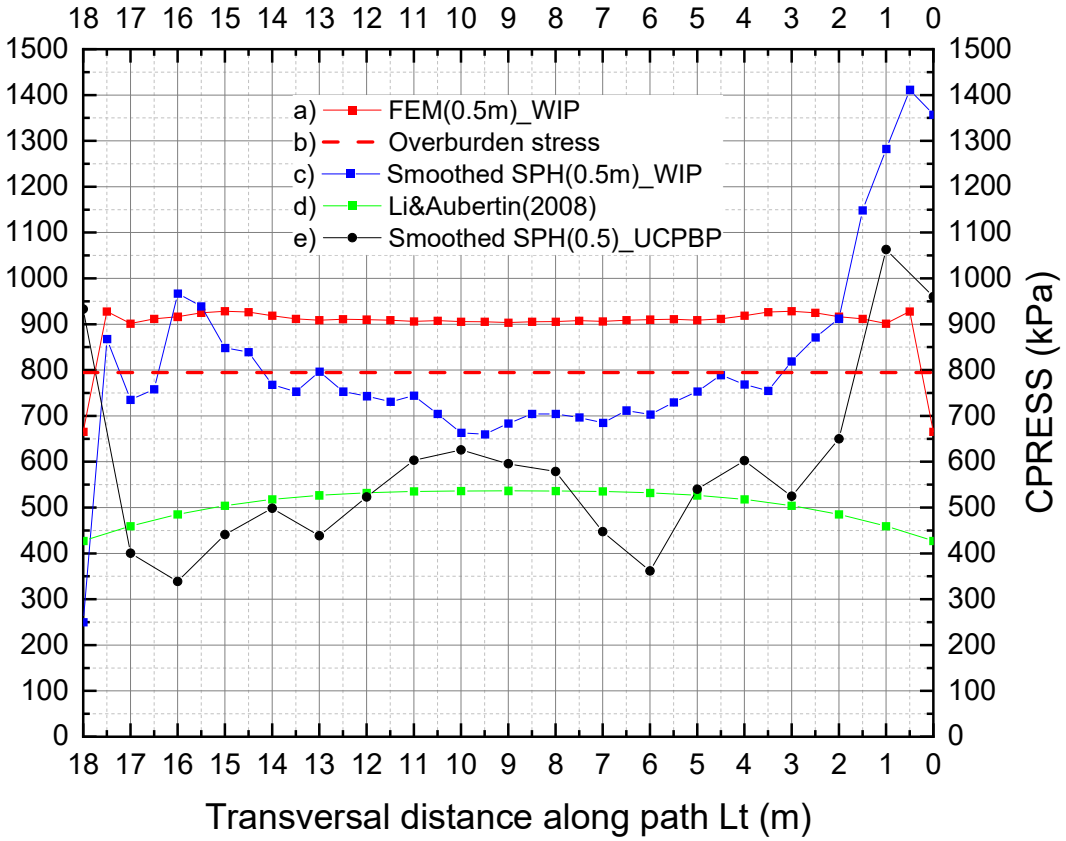

Figure 5-10 Distribution of contact pressures (CPRESS) vs transversal distance along path (L_t) for: a) FEM (seed 0.5m) _WIP, b) overburden stress, c) simplified curve SPH (seed 0.5m)_WIP, d) Results of Li and Aubertin (2008) e) simplified curve SPH (seed 0.5m) _UCPBP_1m/s longitudinal.

5.6 Discussion

The main purpose of this study was to assess the contact pressures along the rock-backfill interface in a backfilled stope. Also, by using a dynamic procedure, the author aimed to determine these contact pressure curves along these interfaces following the dynamic deposition mode of the granular material by using the smoothed particle method. Different backfilling continuous dynamic modes were analyzed, and all performed simulations leading to deduced post processing solution variables were achieved by considering different modelling conditions such as different sizes of smoothed particles and by taking into consideration the CPU runtime. Future investigators may

conduct more advanced simulations by considering different modelling conditions and by using more advanced sophisticated hardware. More efficient and powerful computers are necessary to obtain more precise curves of contact pressures distribution along the rock-backfill interface. This can be achieved by simulating the backfilling process with a smaller size particle of the backfill. The smallest particle's size that has been used in this study was equivalent to $25\ cm$; more precise solution-variables may be obtained by reducing this size to $2.5\ cm$ and this will require a highest computer runtime. Please recall that the initial ($t = 0s$) configuration of the backfill's particles is constituted of uniform spherical smoothed particles having the same diameter. When the dynamic backfilling process starts ($t > 0s$) a new distribution process of the particles will take place and the configuration of the particles will evolve with time until reaching the quasi-static state at the end of the simulation time. This time corresponds to a kinetic energy of the whole system equivalent to zero, this particular time also corresponds to the state in which the backfill will be at rest. It was concluded that the dynamic procedures used to simulate the deposition mode during and after the backfilling process will give a better understanding of the contact pressure stresses at the rock-backfill interfaces.

The present study was limited to a dry granular material modelled using the SPH method built-in Abaqus/explicit commercial software. Future investigators may assess numerically the dynamic backfilling process by using the three types of fill materials discussed in section 2.1 (i.e., rock fill, paste fill and hydraulic fill).

The simulation of the paste fill and hydraulic fill during a dynamic backfilling process is a very difficult task when using an explicit dynamic procedure based an explicit operator. The main difficulty is caused by the variation of the boundary conditions with time of each smoothed particle.

Future investigators may choose to simulate the backfilling state at rest by using consolidation procedure based on a general static procedure. In this case, Abaqus/Standard finite element models may be used to achieve this test, and the kinetic energy of the system should remain null. In this standard finite element method, the alteration of the initial mesh discretizing the backfill will never be altered. This means no separation of the elements is allowed during the simulation. Consequently, the contact pressures (also other solution variables) will never reflect the dynamic

process of a real backfilling event because the backfill material is assumed to be in place at the start till the end of the standard finite element simulation.

Also, it is suggested to study the continuous dynamic backfilling process by using the smoothed particle hydrodynamic method in the case of inclined stopes. The results found by Aubertin et al. (2003), and for which the backfill was modelled in place and in contact with the stope may be compared to the expected results deduced from the SPH model simulation. The SPH results may be used for checking and verifying if arching effect may occur as mentioned by Aubertin et al. (2003). The comparison of results will offer a better understanding of the interaction between the backfill and its enclosing walls.

CHAPTER 6 CONCLUSION AND RECOMMANDATIONS

6.1 Conclusion

Smoothed particle hydrodynamics (SPH) method has been used to study backfilling processes of a backfilled rock stope. Three models were developed using Abaqus 2020 software in order to model a wished-in-place SPH backfilling process, a wished-in-place finite element model using the standard finite element method (FEM), and finally an SPH uniform, continuous and progressive backfilling process (UCPBP). Based on the results deduced from the simulations, the following conclusions have been drawn:

i. Contact pressure (CPRESS) for the FEM-WIP model (Model II) is continuous but not uniform and is maximum in the middle-path and strictly decreases when moving away from the middle-path to reach minimum values at both vertical boundaries. This variation is due to the arching effect and the stress transfer between the stiff backfill material and the stiffer surrounding rock mass due to friction at the interface. A similar result was also previously found by Li and Aubertin (2008).

ii. Contact pressure (CPRESS) for the SPH-WIP model (Model I) shows a new state of interfacial contact stresses and a dense gathering of particles that can occur due to a rearrangement of the particles.

iii. In the case of Model III representing the uniform, continuous and progressive backfilling process (UCPBP):

1) In general, and for a specific initial mesh density, it is expected that values of CPRESSs increase when the seed of particles decreases (or when the initial mesh density decreases).

2) In general, it is expected that values of CPRESSs increase when the backfilling velocities increase.

3) In general, values of CPRESSs are higher for a backfilling process in the transversal direction compared to those of the longitudinal direction.

4) For the backfilling process in the transversal direction, the arching effect is observed and is conditioned by the location of the vertical boundaries where a stress transfer between the

stiff backfills material and the stiffer surrounding rock mass due to friction at the interface of the two materials reduces the pressure and the stress near the boundary walls.

iii.4) An assumed wished-in-place model is unable to account for the change of the unit weight of the backfill material and therefore is unrealistic. The SPH-based dynamic process of backfilling provides more realistic stresses because it takes into consideration particle rearrangement, which is a well-known phenomenon when it comes to backfilling an arbitrary excavation with granular material.

6.2 Recommendations

In this study, the author assessed the application of the smoothed particle hydrodynamic method in the case of a continuous backfilling dynamic process of backfilled stope. It is important to extend the present results to more developed models and this can be done by achieving many suggested future studies.

1. It is important to investigate the case of a backfill material composed of particles having different shapes (sphere, ellipsoid, …) and different sizes.
2. It is also recommended to conduct a full program of simulations (SPH models, explicit finite element models, implicit finite element models, coupled eulerian-lagrangian methods,…) to cover the three general known types of fill which are rock fill, paste fill and hydraulic fill. These analyses may use general static or explicit dynamic or implicit dynamic procedures. The quasi-static procedure may be used in conjunction with a consolidation step in the case of the paste fill and this in order to determine effective stresses (including effective contact pressures) and/or water pressure. The case of an unsaturated medium may be also modelled to determine pore water pressures and effective stresses in both regions i.e., saturated medium and unsaturated medium. Details of these explanation may be found in section 5.6 of the present document.
3. It is important to conduct a future program of appropriate simulations to assess the contact pressures and deformations of an SPH model having inclined stopes. The expected solution variables should be compared to those deduced from standard finite element models or finite difference models or even explicit finite element models. Comparison of results of

contact pressure curves will allow the determination of the inner distribution of principal stresses in order to check the arching effect within the backfilling medium.

4. It is recommended to validate the numerical results with measured fields results. This task will contribute to validate the interpretation of the dynamic mode of backfilling process.

REFERENCES

An, Y., Wu, Q., Shi, C., & Liu, Q. (2016). Three-dimensional smoothed-particle hydrodynamics simulation of deformation characteristics in slope failure. *Geotechnique, 66*(8), 670-680. https://doi.org/10.1680/jgeot.15.P.222

Aubertin, M., Li, L., Arnoldi, S., Belem, T., Bussière, B., Benzaazoua, M., & Simon, R. (2003). Interaction between backfill and rock mass in narrow stopes. *Soil and rock America, 1*(2), 1157-1164.

Balmforth, N. J., & Kerswell, R. R. (2005). Granular collapse in two dimensions. *Journal of Fluid Mechanics, 538*, 399-428. https://doi.org/10.1017/S0022112005005537

Belem, T., & Benzaazoua, M. (2008, 2008/04/01). Design and Application of Underground Mine Paste Backfill Technology. *Geotechnical and Geological Engineering, 26*(2), 147-174. https://doi.org/10.1007/s10706-007-9154-3

Benz, W. (1988). Applications of smooth particle hydrodynamics (SPH) to astrophysical problems. Comput. Phys. Commun. (Netherlands), Netherlands.

Benzaazoua, M., Bussiere, B., Demers, I., Aubertin, M., Fried, E., & Blier, A. (2008). Integrated mine tailings management by combining environmental desulphurization and cemented paste backfill: Application to mine Doyon, Quebec, Canada. *Minerals Engineering, 21*(4), 330-340. https://doi.org/10.1016/j.mineng.2007.11.012

Bowles, J. E. (1996). *Foundation analysis and design* (5th ed. ed.). McGraw-Hill.

Brinkgreve, R., Broere, W., & Waterman, D. (2006). PLAXIS 2D—Version 8 Tutorial Manual. *Plaxisbv: Delft, The Netherlands*.

Bui, H. H., Fukagawa, R., Sako, K., & Ohno, S. (2008). Lagrangian meshfree particles method (SPH) for large deformation and failure flows of geomaterial using elastic-plastic soil constitutive model. *International Journal for Numerical and Analytical Methods in Geomechanics, 32*(12), 1537-1570. https://doi.org/10.1002/nag.688

Chen, W.-F., & Han, D.-J. (2007). *Plasticity for structural engineers*. J. Ross Publishing.

Chen, W., & Qiu, T. (2012, 2012/04/01). Numerical Simulations for Large Deformation of Granular Materials Using Smoothed Particle Hydrodynamics Method. *International Journal of Geomechanics, 12*(2), 127-135. https://doi.org/10.1061/(ASCE)GM.1943-5622.0000149

Dassault Systèmes Simulia Corp. (2020). *Abaqus Theory Manual, Version 6.20, Providence, RI, USA.*

Drescher, A. (1991). *Analytical methods in bin-load analysis*. Elsevier, Amsterdam.

Drucker, D. C., & Prager, W. (1952). Soil mechanics and plastic analysis or limit design. *Quarterly of Applied Mathematics, 10*(2), 157-165.

Emad, M. Z., Mitri, H., & Kelly, C. (2015). State-of-the-art review of backfill practices for sublevel stoping system. *International Journal of Mining, Reclamation and Environment, 29*(6), 544-556.

Fahey, M., Helinski, M., & Fourie, A. (2009). Some aspects of the mechanics of arching in backfilled stopes. *Canadian Geotechnical Journal, 46*(11), 1322-1336. https://doi.org/10.1139/T09-063

Fávero Neto, A. H., & Borja, R. I. (2018, 2018/10/01). Continuum hydrodynamics of dry granular flows employing multiplicative elastoplasticity. *Acta Geotechnica, 13*(5), 1027-1040. https://doi.org/10.1007/s11440-018-0700-3

Gingold, R. A., & Monaghan, J. J. (1977). Smoothed particle hydrodynamics: theory and application to non-spherical stars. *Monthly Notices of the Royal Astronomical Society, 181*(2), 375-389.

Girolami, L., Hergault, V., Vinay, G., & Wachs, A. (2012, 2012/05/01). A three-dimensional discrete-grain model for the simulation of dam-break rectangular collapses: comparison between numerical results and experiments. *Granular Matter, 14*(3), 381-392. https://doi.org/10.1007/s10035-012-0342-3

Hallquist, J. O. (2007). LS-DYNA keyword user's manual. *Livermore Software Technology Corporation, 970*.

He, X., Liang, D., Wu, W., Cai, G., Zhao, C., & Wang, S. (2018, 2018/08/10). Study of the interaction between dry granular flows and rigid barriers with an SPH model. *International Journal for Numerical and Analytical Methods in Geomechanics, 42*(11), 1217-1234. https://doi.org/https://doi.org/10.1002/nag.2782

Helwany, S. (2007). *Applied soil mechanics with ABAQUS applications*. John Wiley & Sons.

Huang, Y., Dai, Z., & Zhang, W. (2014). *Geo-disaster Modeling and Analysis: An SPH-based Approach*. Springer-Verlag Berlin Heidelberg. https://doi.org/10.1007/978-3-662-44211-1

Itasca. (2002). FLAC2D - Fast Lagrangian Analysis of Continua, User's Guide, Version 4.00. *ITASCA, Minnesota, USA*.

Itasca. (2013). FLAC3D - Fast lagrangian analysis of continua in 3 dimensions. *Itasca Consulting Group Inc., Minneapolis, MN*.

Itasca, F. Fast Lagrangian analysis of continua. *Itasca Consulting Group Inc., Minneapolis, Minn*.

Itoh, K., & Toyosawa, Y. (2009). Field test of slope failure during slope cutting work. *JSCE Journals, 65*(1), 254-265.

Jahanbakhshzadeh, A., Aubertin, M., & Li, L. (2017, 2017/06/01). A New Analytical Solution for the Stress State in Inclined Backfilled Mine Stopes. *Geotechnical and Geological Engineering, 35*(3), 1151-1167. https://doi.org/10.1007/s10706-017-0171-6

Jahanbakhshzadeh, A., Aubertin, M., & Li, L. (2018). Three-dimensional stress state in inclined backfilled stopes obtained from numerical simulations and new closed-form solution. *Canadian Geotechnical Journal, 55*(6), 810-828. https://doi.org/10.1139/cgj-2016-0385

Janssen, H. (1895). Versuche uber Getreidedruck in Silozellen. *Z. Ver. Dtsch. Ing., 39*(35), 1045-1049.

Kermani, E., & Qiu, T. (2018). Simulation of quasi-static and dynamic collapses of rectangular granular columns using smoothed particle hydrodynamics method. *International Journal of Geomechanics, 18*(9). https://doi.org/10.1061/(asce)gm.1943-5622.0001256

Kitano, T., Fujita, S., Ogura, H., & Suganuma, A. (2016). Analyses of the Failure of an Embankment Slope and Its Influence on the Pipeline Installed in that Embankment Slope. Pipelines 2016: Out of Sight, Out of Mind, Not Out of Risk - Proceedings of the Pipelines 2016 Conference, Kansas City, MO, United states.

Lajeunesse, E., Monnier, J. B., & Homsy, G. M. (2005, 2005/10/01). Granular slumping on a horizontal surface. *Physics of Fluids, 17*(10), 103302. https://doi.org/10.1063/1.2087687

Li, L., & Aubertin, M. (2008). An improved analytical solution to estimate the stress state in subvertical backfilled stopes. *Canadian Geotechnical Journal, 45*(10), 1487-1496. https://doi.org/10.1139/t08-060

Li, L., & Aubertin, M. (2009a, 02/). Influence of Water Pressure on the Stress State in Stopes with Cohesionless Backfill. *Geotechnical and Geological Engineering, 27*(1), 1-11. https://doi.org/10.1007/s10706-008-9207-2 (Geotech. Geolog. Eng. (Netherlands))

Li, L., & Aubertin, M. (2009b). Numerical investigation of the stress state in inclined backfilled stopes. *International Journal of Geomechanics, 9*(2), 52-62. https://doi.org/10.1061/(ASCE)1532-3641(2009)9:2(52)

Li, L., Aubertin, M., Simon, R., Bussière, B., & Belem, T. (2003). Modeling arching effects in narrow backfilled stopes with FLAC. *FLAC and Numerical Modeling in Geomechanics*, 211-219.

Liu, M.-B., & Liu, G.-R. (2016). *Particle methods for multi-scale and multi-physics* (Vol. 400). World Scientific.

Lube, G., Huppert, H. E., Sparks, R. S. J., & Freundt, A. (2005, 10/04/). Collapses of two-dimensional granular columns. *Physical Review E, 72*(4), 041301. https://doi.org/10.1103/PhysRevE.72.041301

Lube, G., Huppert, H. E., Sparks, R. S. J., & Hallworth, M. A. (2004). Axisymmetric collapses of granular columns. *Journal of Fluid Mechanics, 508*, 175-199. https://doi.org/10.1017/S0022112004009036

Lucy, L. B. (1977). A numerical approach to the testing of the fission hypothesis [close binary star formation]. *Astronomical Journal, 82*(12), 1013-1024. https://doi.org/10.1086/112164

Marston, A. (1930). The Theory of External Loads on Closed Conduits in the Light of the Latest Experiments. *Iowa Engineering Experimental Station, Bulletin 9*, 36.

Meriaux, C. (2006). Two dimensional fall of granular columns controlled by slow horizontal withdrawal of a retaining wall. *Physics of Fluids, 18*(9). https://doi.org/10.1063/1.2335477

Monaghan, J. J., & Lattanzio, J. C. (1985). A refined particle method for astrophysical problems. *Astronomy and Astrophysics, 149*(1), 135-143.

Monaghan, J. J., & Lattanzio, J. C. (1991). A simulation of the collapse and fragmentation of cooling molecular clouds. *Astrophysical Journal, 375*(1), 177-189. https://doi.org/10.1086/170179

Monaghan, J. J., & Lattanzio, J. C. (1992). Numerical modelling of star formation in giant molecular clouds. *Australian Journal of Physics, 45*(4), 559-559.

Moriguchi, S., Borja, R. I., Yashima, A., & Sawada, K. (2009, 2009/03/01). Estimating the impact force generated by granular flow on a rigid obstruction. *Acta Geotechnica, 4*(1), 57-71. https://doi.org/10.1007/s11440-009-0084-5

Nonoyama, H., Sawada, K., Moriguchi, S., Yashima, A., & Itoh, K. (2012). A 2D SPH simulation for real-scale slope excavation experiment. *Journal of JGS, 7*(4), 543-555.

Owen, P. J., Cleary, P. W., & Mériaux, C. (2009, 2009/03/20). Quasi-static fall of planar granular columns: comparison of 2D and 3D discrete element modelling with laboratory experiments. *Geomechanics and Geoengineering, 4*(1), 55-77. https://doi.org/10.1080/17486020902767388

Potvin, Y., Thomas, E., & Fourie, A. (2005). Handbook on mine fill. In *Not available* (pp. 179). Australian Centre for Geomechanics.

RocScience. (2002). *Phase2: 2D finite element program for calculating stresses and estimating support around underground excavations*. Toronto, Canada.

Yao, Y., Cui, Z., & Wu, R. (2012). Development and challenges on mining backfill technology. *Journal of Materials Science Research, 1*(4), 73.

Zhan, L., Peng, C., Zhang, B., & Wu, W. (2019). Three-dimensional modeling of granular flow impact on rigid and deformable structures. *Computers and Geotechnics, 112*, 257-271. https://doi.org/10.1016/j.compgeo.2019.03.019

Zhang, X., Ding, Y., Sheng, D., Sloan, S. W., & Huang, W. (2016, 2016/05/07). Quasi-static collapse of two-dimensional granular columns: insight from continuum modelling. *Granular Matter, 18*(3), 41. https://doi.org/10.1007/s10035-016-0643-z

Zhang, X., Krabbenhoft, K., & Sheng, D. (2014, 2014/08/01). Particle finite element analysis of the granular column collapse problem. *Granular Matter, 16*(4), 609-619. https://doi.org/10.1007/s10035-014-0505-5

Zhou, S., & Li, L. (2022). Numerical Investigation on the Impact of Tailings Slurry on Catch Dams Built at the Downstream of a Breached Tailings Pond. *Processes, 10*(5), 898.